

ACCUMULATED PHOTON ECHOES AS A PROBE
OF DEPHASING DYNAMICS IN $\text{Nd}^{3+}:\text{CaF}_2$,
 CaF_2YF_3 , AND GLASSES

By

KEITH WAYNE VER STEEG


Bachelor of Science
Iowa State University
Ames, Iowa
1986

Master of Science
Oklahoma State University
Stillwater, Oklahoma
1990

Submitted to the Faculty of the
Graduate College of the
Oklahoma State University
in partial fulfillment of
the requirements for
the Degree of
DOCTOR OF PHILOSOPHY
July, 1994

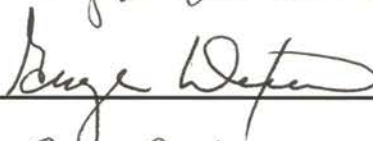
ACCUMULATED PHOTON ECHOES AS A PROBE
OF DEPHASING DYNAMICS IN Nd³⁺ :CaF₂,
CaF₂YF₃, AND GLASSES

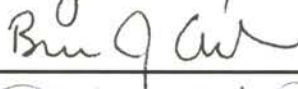
Thesis Approved:

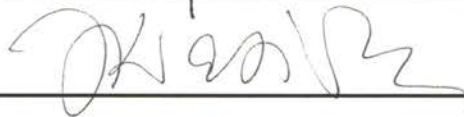


Thesis Adviser











Dean of the Graduate College

ACKNOWLEDGMENTS

I would like to express my appreciation to all of the people who helped me with my research at Oklahoma State University. Special thanks go to my thesis advisor, Dr. Richard C. Powell, for allowing me to work in his laboratory, letting me pursue the study of accumulated photon echoes, and for giving his advice and guidance. I would also like to thank Tasoltan Basiev, Alexander Karasik, and Vladimir Fedorov of the General Physics Institute in Moscow, Russia for supplying the mixed and pure calcium fluoride crystals used in this study, and for helping to make APE measurements on these samples. I would like to express special appreciation to Professor Karasik who was a continuous source of encouragement and help in understanding the physics of this study. I would also like to thank Dr. Roger Reeves and the members of my committee, Dr. Bruce Ackerson, Dr. George Dixon, Dr. Jerzy Krasinski, and Dr. Larry Scott

I would like to thank my parents, Ken and Delores Ver Steeg, for their love, support, and belief in my abilities. My special thanks also to my lovely wife Lori, for her love, help, and support throughout this work.

I would also like to thank my Lord and Savior Jesus Christ for sustaining me physically, mentally, and spiritually during these past years of my graduate education.

Financial support for my graduate study was supplied in part by a fellowship from the OSU Department of Physics and Astronomy. The APE research was funded by the National Science Foundation under grant number DMR-9103648.

TABLE OF CONTENTS

Chapter	Page
I. INTRODUCTION	1
II. EXPERIMENT PROCEDURES AND EQUIPMENT	3
Samples studied	7
III. APE SIGNAL CHARACTERISTICS	8
The two-pulse echo	10
The three-pulse stimulated echo	11
The accumulated 3 pulse stimulated echo	14
APE technical considerations	15
Spectral Diffusion	15
Pulse Jitter	17
Bottleneck Lifetime	18
FID Effects	18
Phase Jitter at the Detector	19
Overlapping Stark Levels	20
IV. RADIATIONLESS RELAXATION AND DEPHASING PROPERTIES	21
Electron-phonon interaction	21
Single phonon absorption and emission	21
Raman Processes	22
Results for glasses	25
Results for disordered crystal	37
Results for ordered crystal	47
V. CONCLUSION	55
Summary of Results	55
Suggestions for Future Work	57
BIBLIOGRAPHY	59
APPENDIX	62

Chapter	Page
. APPENDIX A - THE TUNED PREAMPLIFIER	63
. APPENDIX B - APE SIGNAL THEORY	66
The excitation matrix	66
The relaxation matrix	72
Calculation of the Bloch vector following a 2-pulse sequence.	74
Calculation of the APE signal	76
. APPENDIX C - APE DATA TABLES	81

LIST OF TABLES

Table	Page
I. $^4I_{9/2} \rightarrow ^4G_{5/2}, ^2G_{7/2}$ Absorption spectrum gaussian deconvolution for Nd^{3+} doped glasses	82
II. Temperature dependence of T_2 as measured by APE in Nd^{3+} :ED2 silicate glass at 593.1 nm, $\Delta\lambda = 1.5\text{nm}$	83
III. Wavelength dependence of T_2 as measured by APE in Nd^{3+} :ED2 silicate glass at 9.5K	84
IV. Temperature dependence of T_2 as measured by APE in Nd^{3+} :ED2 lithium germanate glass at 594.0 nm, $\Delta\lambda = 1.5\text{nm}$	85
V. Wavelength dependence of T_2 as measured by APE in Nd^{3+} :lithium germanate glass at 9.5K	86
VI. Temperature dependence of T_2 as measured by APE in Nd^{3+} : phosphate glass (UP-77) at 589.9 nm, $\Delta\lambda = 1.5\text{nm}$	87
VII. Wavelength dependence of T_2 as measured by APE in Nd^{3+} : phosphate glass (UP-77) at 9.5K	88
VIII. Temperature dependence of T_2 as measured by APE in Nd^{3+} : CaF_2YF_3 at 579.0 nm, $\Delta\lambda = 1.5\text{nm}$	89
IX. Temperature dependence of T_2 as measured by APE in Nd^{3+} : CaF_2YF_3 at 580.2 nm, $\Delta\lambda = 1.5\text{nm}$	90
X. Temperature dependence of T_2 as measured by APE in Nd^{3+} : CaF_2YF_3 at 579.04 nm, $\Delta\lambda = 0.1\text{nm}$	91
XI. Temperature dependence of T_2 as measured by APE in Nd^{3+} : CaF_2YF_3 at 580.04 nm, $\Delta\lambda = 0.1\text{nm}$	92
XII. Wavelength dependence of T_2 as measured by APE in Nd^{3+} : CaF_2YF_3 at 9.5K	93
XIII. Temperature dependence of T_2 as measured by APE in 0.3% Nd^{3+} : CaF_2 at 579.09 nm, $\Delta\lambda = 0.1\text{nm}$	94

Table		Page
XIV.	Temperature dependence of T_2 as measured by APE in 0.3% Nd ³⁺ : CaF ₂ at 579.45 nm, $\Delta\lambda = 0.1\text{nm}$	95
XV.	FFT frequency component distribution from APE signals of M and N centers in Nd ³⁺ :CaF ₂ at 9K, $\Delta\lambda = 0.1\text{nm}$	96

LIST OF FIGURES

Figure	Page
1. Basic schematic of a pump/probe experiment	4
2. Example of the $1/f$ and white noise power spectrum typical to an APE experiment.	4
3. Schematic of the APE experiment setup	6
4. Schematic of the pulse sequence needed to generate a 2-pulse photon echo (a), and a 3 pulse stimulated photon echo (b). The axes and arrows are explained in the text.	12
5. Energy levels of Nd^{3+} and an equivalent 3-level model. k_{ij} denotes the relaxation rate between states i and j	16
6. Temperature dependence of the dephasing rate in $\text{Nd}^{3+}:\text{ED2}$ silicate glass at $\lambda = 593.1$ nm. Insert shows the position of the excitation wavelength relative to the absorption spectrum. . . .	26
7. Absorption spectrum (left axis) of ED2 silicate glass: $\text{Nd}_2\text{O}_3(2.0\text{wt.}\%)$ at 9K and approximate Stark energy level locations. Open circles and squares denote the total de- phasing rates (right axis).	28
8. Temperature dependence of the dephasing rate in $\text{Nd}^{3+}:$ lithium germanate glass at $\lambda = 594.0$ nm. Insert shows the position of the excitation wavelength relative to the absorption spectrum.	30
9. APE signal functions in three glasses at 30K: (a) ED2 silicate, $\lambda = 593.1\text{nm}$, (b) lithium germanate, $\lambda = 594.0\text{nm}$ (c) lithium phosphate, $\lambda = 589.9\text{nm}$	31
10. Absorption spectrum (left axis) of lithium germanate glass: $\text{Nd}_2\text{O}_3(2.0\text{wt.}\%)$ at 9K and approximate Stark energy level locations. Open circles and squares denote the total de- phasing rates (right axis).	32

Figure	Page
11. Temperature dependence of the dephasing rate in Nd^{3+} : lithium phosphate glass at $\lambda = 589.9$ nm. Insert shows the position of the excitation wavelength relative to the absorption spectrum.	33
12. Absorption spectrum (left axis) of UP77 phosphate glass: Nd_2O_3 (0.5wt.%) at 9K and approximate Stark energy level locations. Open circles and squares denote the total dephasing rates (right axis).	35
13. Dependence of dephasing rate on excitation energy at 9.5K in Nd^{3+} doped glasses. (a) ED2 silicate, (b) lithium germanate, (c) lithium phosphate.	36
14. Absorption spectrum of $\text{CaF}_2\text{-YF}_3(12\text{wt.}\%) - \text{NdF}_3(0.1\text{wt.}\%)$ disordered crystal at 9K (left axis) and total dephasing rate (right axis).	39
15. Accumulated photon echo signals in $\text{CaF}_2 - \text{YF}_3(12\text{wt.}\%):\text{NdF}_3(4\text{wt.}\%)$ for (a) 579.0 nm, $T=9\text{K}$; (b) 576.7 nm, $T=9\text{K}$; (c) 579.0 nm, $T=65\text{K}$	40
16. Raman spectra of 2wt.% $\text{NdF}_3:\text{CaF}_2\text{-YF}_3$ at 300K.	41
17. Absorption spectrum (left axis) and energy dependence of the dephasing rate (right axis) in 4wt% $\text{NdF}_3:\text{CaF}_2 - \text{YF}_3$ at 9K. . . .	43
18. Temperature dependence of the total dephasing rates of the I center (579.0 nm) in $\text{CaF}_2 - \text{YF}_3(12\text{wt.}\%):\text{NdF}_3(4\text{wt.}\%)$. The circles represent the echo decay components.	44
19. Absorption spectra of $\text{CaF}_2 - \text{YF}_3(12\text{wt.}\%):\text{NdF}_3(4\text{wt.}\%)$ at 9K (solid line) and 77K (dashed line).	46
20. Absorption spectrum of 0.3wt.% $\text{Nd}_2\text{O}_3:\text{CaF}_2$ at 9K. M and N label two different crystal field sites.	48
21. (a) APE signal of 0.3% $\text{Nd}^{3+}:\text{CaF}_2$ at 9K, $\lambda_{exc} = 579.36$ nm. (b) Fourier transform of the APE signal. Principle peaks are labeled by frequency.	50
22. Fourier analysis of 23 APE signals in 0.3% $\text{Nd}^{3+}:\text{CaF}_2$ at 9K measured at wavelengths corresponding to both M and N centers. Each "bin" of the histogram represents an interval of 2 GHz.	51

Figure	Page
23. Temperature dependence of the dephasing rate for 0.3% Nd ³⁺ : CaF ₂ N center (left) and M center (right). The fit is to a direct, single phonon absorption process.	54
24. Frequency response of the tuned preamplifier	64
25. Tuned preamplifier schematic	65
26. Pump-probe timing diagram for APE signal generation.	66
27. Coordinate representation of the Bloch vector (R') precessing about the pseudofield vector (Ω').	68

CHAPTER I

INTRODUCTION

The manufacture of solid state lasers has relied heavily upon rare earth doped crystalline and glass materials. Neodymium has proven to be the dopant ion most widely used in medium to high powered laser systems, in part because it has broad absorption bands which enable efficient flash lamp pumping. The technical success of Nd^{3+} doped laser materials generated an interest among scientists to understand the physical mechanisms by which excited state Nd^{3+} relax non-radiatively to the metastable ${}^4F_{3/2}$ level, from which lasing occurred. In order to explain radiationless relaxation between J manifolds separated by large energy gaps, theories were developed that relied on the emission of multiple high energy phonons[1] in crystals[2] and glasses.[3] The crucial factor affecting the rate of relaxation was determined to be the energy gap to the next lower level with the relation between the relaxation rate W and the energy gap ΔE going as:

$$W \propto \exp(-\alpha\Delta E). \quad (1)$$

where α parameterizes the coupling between the dopant ion and the host lattice.

The multiphonon theory does not apply to relaxation across energy gaps less than about 1000 cm^{-1} , therefore it was not useful for predicting radiationless relaxation rates within a J manifold where the Stark energy levels are separated by tens or hundreds of wavenumbers, and relaxation times are on the order of 10^{-12} seconds. One such manifold of interest in Nd^{3+} is that of the ${}^4G_{5/2}, {}^2G_{7/2}$ state, consisting of seven Kramer's degenerate Stark levels. Optical linewidth measurement of these non fluorescing Stark levels using fluorescence line narrowing (FLN) or optical holeburning (HB) techniques were difficult to perform, requiring non resonant methods.

This thesis describes an experiment in which a method of time domain laser spectroscopy has been used to measure optical dephasing times within inhomogeneously broadened Stark levels of the ${}^4G_{5/2}, {}^2G_{7/2}$ manifold of Nd^{3+} . These measurements were made in glasses, disordered crystals, and pure crystals in order to gain information regarding the relaxation times and dynamics as the host changes from a disordered to an ordered system. The method of spectroscopy used is called accumulated photon echo (APE), and it allows one to directly measure linewidths of non fluorescing transitions.

Throughout this thesis, references given are by no means exhaustive but representative of the topic at hand and will point the reader to more detailed material. The data tables are collected in Appendix C in order to avoid unnecessary breaks in the text. Chapter 2 describes the experimental setup and samples used in this study. Chapter 3 explains what the APE is, and how it is generated. The theoretical details of APE signal derivation are presented separately in Appendix B. Chapter 4 gives a brief overview of the various models used to interpret optical dephasing, and presents and explains the experimental results. Lastly, Chapter 5 summarizes the results and suggests topics for future study.

CHAPTER II

EXPERIMENT PROCEDURES AND EQUIPMENT

The geometry of the experimental setup is that of a basic pump/probe design (Fig. 1) in which a quasi-CW pulsed (82 MHz) laser beam is split into two parts by a 10% beamsplitter. The weaker (probe) beam passes through a mechanical delay line before it is combined with the pump beam within the sample to be studied. The APE signal, manifested as a change in the transmitted probe beam intensity as a function of pump/probe delay (t_{12}), is detected by a PIN silicon photodiode. As discussed in more detail in the next chapter and in Appendix B, the APE signal (probe intensity versus delay) yields the dephasing time (T_2) according to $I_{pr}(t_{12}) \propto e^{-2t_{12}/T_2}$.

As in any laser spectroscopy experiment, background noise is always a problem that must be dealt with. In the APE experiment, the signal contrast ratio ($\text{pump}_{\text{on}} - \text{pump}_{\text{off}} / \text{pump}_{\text{on}} \approx 10^{-5} - 10^{-8}$) which means that the detected signal is easily swamped by laser, detector, and amplifier noise. These three noise sources contribute to what is called "1/f noise". Figure 2 shows a graph of the 1/f and white noise power as a function of frequency. From this figure, it can be seen that to reduce the effects of noise, it is necessary to move the detection frequency from DC out to 3-4 MHz, where the 1/f noise is much lower. This frequency shift can be achieved by a technique called heterodyning, in which the pump beam is modulated at frequency f_o and combined with the unmodulated probe beam within the sample. The APE signal will thus be modulated at f_o , and can be detected by a properly triggered phase sensitive amplifier.

In this experiment, an acousto-optic modulator (AOM) modulated the pump beam. A digital pulse generator connected to the AOM driver allowed us to set the

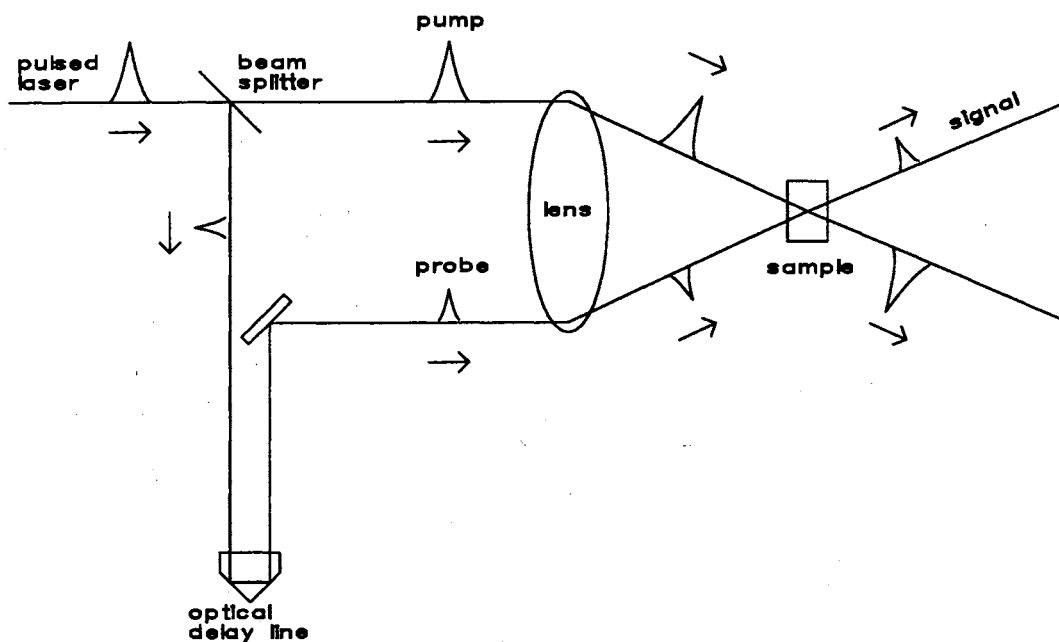


Figure 1. Basic schematic of a pump/probe experiment

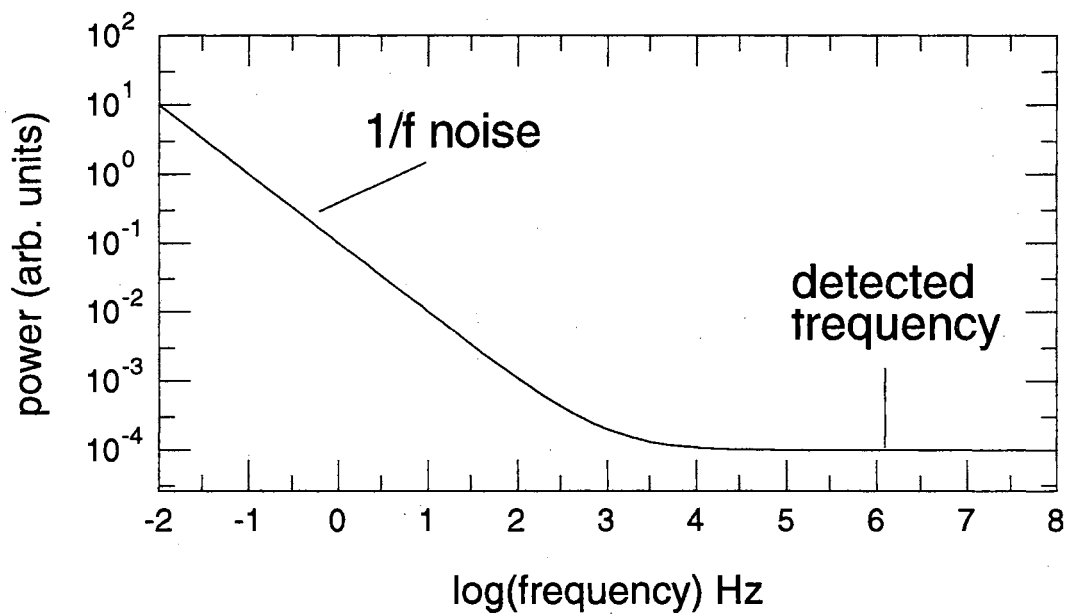


Figure 2. Example of the $1/f$ and white noise power spectrum typical to an APE experiment.

chopping frequency to approximately 4 MHz, and a high speed lock-in amplifier (EG&G 5202) was used to detect the output of the photodiode. A narrowband preamplifier connected directly to the photodiode housing increased the APE signal by 20db before it was fed into the lock-in amplifier. Without this tuned amplifier, described in Appendix A, no signal could be detected by the lock-in.

Further noise reductions dealt with the light scattered from the interference grating formed by parallel polarized pump and probe beams near zero delay. The interference grating is very sensitive to mechanical vibrations caused by the cryogenic refrigerator. A way to eliminate the interference grating is to orthogonally polarize the pump and probe beams, which was accomplished in this experiment with polarization rotators and Glan-Thompson polarizers (Fig. 3).

Finally, movement of the delay line and stepping of the boxcar was synchronized by a microcomputer (WYSE '286) running a GPIB control program called Labtech Notebook. The lock-in amplifier output was acquired by the signal processor three seconds after the delay line was translated. This delay allowed the APE frequency grating to recover from the erasure caused by the delay line movement, and insured that there was no signal distortion due to the one second time constant of the lock-in amplifier.

All of the experiments were carried out at low temperature. The samples were mounted on a copper cold finger bolted to the second stage of a CTI Cryogenics closed-cycle refrigerator. A Ge diode mounted at the bottom of the second stage together with a manganin wire heater and a Lakeshore temperature controller provided temperature control from 8.8K to 100K, ± 0.5 K. Although the temperature sensor was mounted at the bottom of the second stage cold finger rather than next to the sample, the difference in temperature between these two points was less than 0.2 K throughout the temperature range used in these measurements.

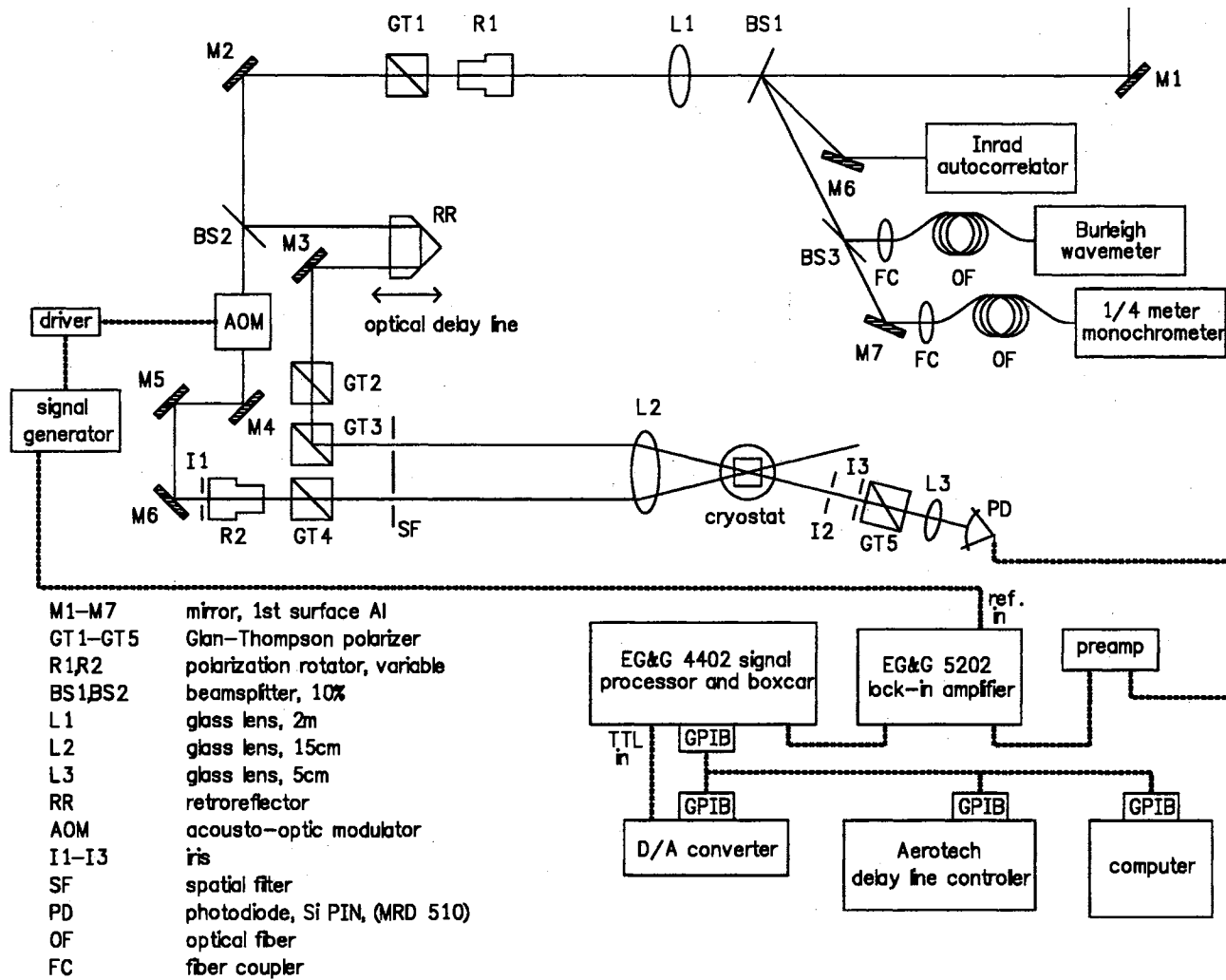


Figure 3. Schematic of the APE experiment

Samples studied

lithium silicate glass

$\text{SiO}_2(60\text{mol}\%)\text{Li}_2\text{O}(27.5\text{mol}\%)\text{CaO}(10\text{mol}\%)\text{Al}_2\text{O}_3(2.5\text{mol}\%)$

$\text{Nd}_2\text{O}_3(2.0\text{wt}\%)$

LLNL-1005, ED2

0.498cm x 0.871cm x 0.168cm thick

lithium germanate glass

$\text{Li}_2\text{Ge}_7\text{O}_{15}$

$\text{Nd}_2\text{O}_3(2.0\text{mol}\%)$

LLNL

0.7cm x 1.15cm x 0.8cm thick

calcium yttrium fluoride

$\text{CaF}_2\text{-YF}_3(12\text{wt}\%)$

$\text{NdF}_3(4\text{wt}\%)$

GPI

0.6cm x 0.4cm x 0.095cm thick

lithium phosphate glass

$\text{Nd}_2\text{O}_3(0.5\text{wt}\%)$

LLNL-6942, UP-77

0.516cm x 1.38cm x 0.084cm thick

calcium fluoride

CaF_2

$\text{NdF}_3(0.3\text{wt}\%)$

GPI 12-22-65(?)

0.75cm x 1.1cm x 0.3cm thick

All the samples were cut and polished to at least $1\mu\text{m}$.

GPI = General Physics Institute, Moscow, Russia

LLNL = Lawrence Livermore National Laboratory, Livermore, CA, USA

CHAPTER III

APE SIGNAL CHARACTERISTICS

This chapter will serve to explain both quantitatively and figuratively how the accumulated photon echo (APE) is generated, how it can be used to measure T_2 in materials doped with optically active impurities, and what problems arise when attempting to use this method in an actual experiment.

One goal of high resolution optical spectroscopy is to uncover information about the homogeneous linewidth (Γ_h) of a particular transition for an impurity embedded in a host material. Typically the host material has some degree of internal disorder that causes the transition of interest to become inhomogeneously broadened, and to thus render direct measurement of Γ_h impossible by conventional optical spectroscopy. The invention of the laser has paved the way for the development of techniques to measure transition linewidths hidden by inhomogeneously broadened spectra. To this end, three experimental methods have become important. The first two, optical holeburning and fluorescence line narrowing (FLN), serve to measure Γ_h in the frequency domain by selective excitation of a single homogeneous packet of absorbing impurity centers.

The formalism used to describe the interaction of an ensemble of two-level systems with a coherent excitation field relies on solving the Liouville equation for the density matrix ρ

$$i\hbar\dot{\rho} = [H, \rho]. \quad (2)$$

H is the total Hamiltonian given by

$$H = H_0 + H_I + H_R \quad (3)$$

where

- H_0 = energy of an isolated two-level system (TLS)
- H_I = $-\vec{\mu} \odot \vec{E}$, which is the interaction energy between the transition dipole moment $\vec{\mu}$ and the applied field \vec{E}
- H_R = energy of interaction with all processes that return the ensemble to thermal equilibrium.

Feynman-Vernon-Hellwarth vector diagrams[4] (FVD) are used to simplify Eqn. 2 and to represent graphically the dynamics of the TLS. Within this representation, ρ is described by the Bloch vector \mathbf{R} which rotates in a three-dimensional space defined by three mutually orthogonal axes $\hat{1}, \hat{2}, \hat{3}$ where

$$\mathbf{R} = u\hat{1} + v\hat{2} + w\hat{3}. \quad (4)$$

The projection of \mathbf{R} onto the three axes is given by

$$\begin{aligned} u &= \rho_{12} + \rho_{21} \\ v &= i(\rho_{21} - \rho_{12}) \\ w &= \rho_{22} - \rho_{11} \end{aligned} \quad (5)$$

The population difference between the excited state (ρ_{22}) and ground state (ρ_{11}) is given by the last of Eqns. 5, in which w is called the inversion parameter. Thus, the $\hat{3}$ axis represents the degree of system inversion. If \mathbf{R} points in the $+\hat{3}$ direction, the entire population is inverted, and if \mathbf{R} points in the $-\hat{3}$ direction the ensemble is in the ground state. The first two of Eqns. 5 represent the coherence parameters u and v . Therefore the relative phase of \mathbf{R} is given by its projection onto the $\hat{1}, \hat{2}$ plane. In converting to the $\hat{1}, \hat{2}, \hat{3}$ representation, a second vector is defined that corresponds to the excitation field

$$\beta = \text{Re}\chi^*(t)\hat{1} + \text{Im}\chi^*(t)\hat{2} + \omega_o\hat{3} \quad (6)$$

where χ is the Rabi frequency

$$\chi = \frac{\mu \odot \mathbf{E}}{\hbar} \quad (7)$$

and $\omega_o = (E_b - E_a)/\hbar$ is the resonance frequency of a two level system with ground state and excited state energies E_a and E_b , respectively and the excitation field is given by \mathbf{E} . Figure 25 in Appendix B illustrates this coordinate system, the only difference in this figure is that β is replaced by a modified pseudofield vector $\mathbf{\Omega}$, as explained in the appendix.

In the $\hat{1}, \hat{2}, \hat{3}$ representation Eqn. 2 is transformed to the equation of motion for a vector \mathbf{R} that is precessing about β according to

$$\frac{d\mathbf{R}}{dt} = \beta \otimes \mathbf{R}. \quad (8)$$

The solution to Eqn. 2 (and Eqn. 8) for a two-pulse sequence is given in Appendix B. Mention of the FVD formalism is made here to provide a conceptual framework for the discussion of photon echoes which follows.

The two-pulse echo

The third method, the photon echo, obtains information regarding Γ_h in the time domain by measuring the time it takes for an ensemble of optically excited impurities to loose phase coherence. This dephasing time, T_2 , is related to Γ_h by

$$T_2 = \frac{1}{\pi\Gamma_h}. \quad (9)$$

The photon echo is the optical analog of the nuclear spin echo, which was discovered in 1950[5] in the field of nuclear magnetic resonance spectroscopy. Shortly after the invention of the ruby laser in 1960, scientists observed the two pulse photon echo (2PE) in ruby.[7] Referring to Fig. 4(a), the generation of a two-pulse echo begins at time $t = 0$, when a coherent light pulse of duration τ and intensity

$$\int_0^\tau \frac{\mu \odot \mathbf{E}}{\hbar} dt = \frac{\pi}{2} \quad (10)$$

induces an ensemble of impurity ions to oscillate in phase. This is represented graphically in Fig. 4(a), panel 1 by an inhomogeneous distribution of Bloch vectors, \mathbf{R} , rotating by 90° from the $-\hat{3}$ direction to the $\hat{1}, \hat{2}$ plane. Due to local inhomogenities in their environment, the oscillating dipoles drift out of phase with

respect to each other with a characteristic time given by $1/\Gamma_{inh}$, where Γ_{inh} represents the width of the inhomogeneous distribution function. This drift out of phase, and subsequent decrease of macroscopic polarization is termed free induction decay (FID), and is represented in Fig. 4(a), panel 2 by the precession of the individual Bloch vectors in the $\hat{1}, \hat{2}$ plane. After a time $t = t_{12}$, a second coherent pulse of area π reverses the phase drift so that the direction of the dipoles' phase drift reverses itself. At time $t = 2t_{12}$, the dipoles are exactly rephased and a coherent optical "echo" signal is emitted which can be measured with a suitable light detector.

During the time $2t_{12}$, processes that cause irreversible dephasing (i.e., incoherent interactions such as phonon scattering, radiative or nonradiative population relaxation, spin exchange) effectively remove dipoles from the rephasing event, thus the rephased signal amplitude will decrease as time t_{12} increases. The characteristic time for the echo signal decrease is called the total dephasing time, T_2 , and is given by

$$\frac{1}{T_2} = \frac{1}{2T_1} + \frac{1}{T_2^*} \quad (11)$$

where T_1 is the population relaxation time and T_2^* is the pure dephasing time. The pure dephasing time can further be separated into a component corresponding to processes that affect the ensemble of dipoles homogeneously (T_2') and those which affect the ensemble inhomogeneously (T_2^{inh})

$$\frac{1}{T_2^*} = \frac{1}{T_2'} + \frac{1}{T_2^{inh}} \quad (12)$$

The three-pulse stimulated echo

This having been said concerning the 2PE, we next mention a similar coherent transient, the 3 pulse stimulated photon echo (3PSE). The generating pulse sequence is similar to that for the 2PE; and is shown figuratively in part (b) of Fig. 4. At time $t = 0$ a coherent $\pi/2$ light pulse resonantly excites an ensemble of ions, creating a state that is a superposition of the ground and excited states (R rotates 90° to the $\hat{1}, \hat{2}$ plane in Fig. 4 (b) panel 1). The ensemble of oscillators

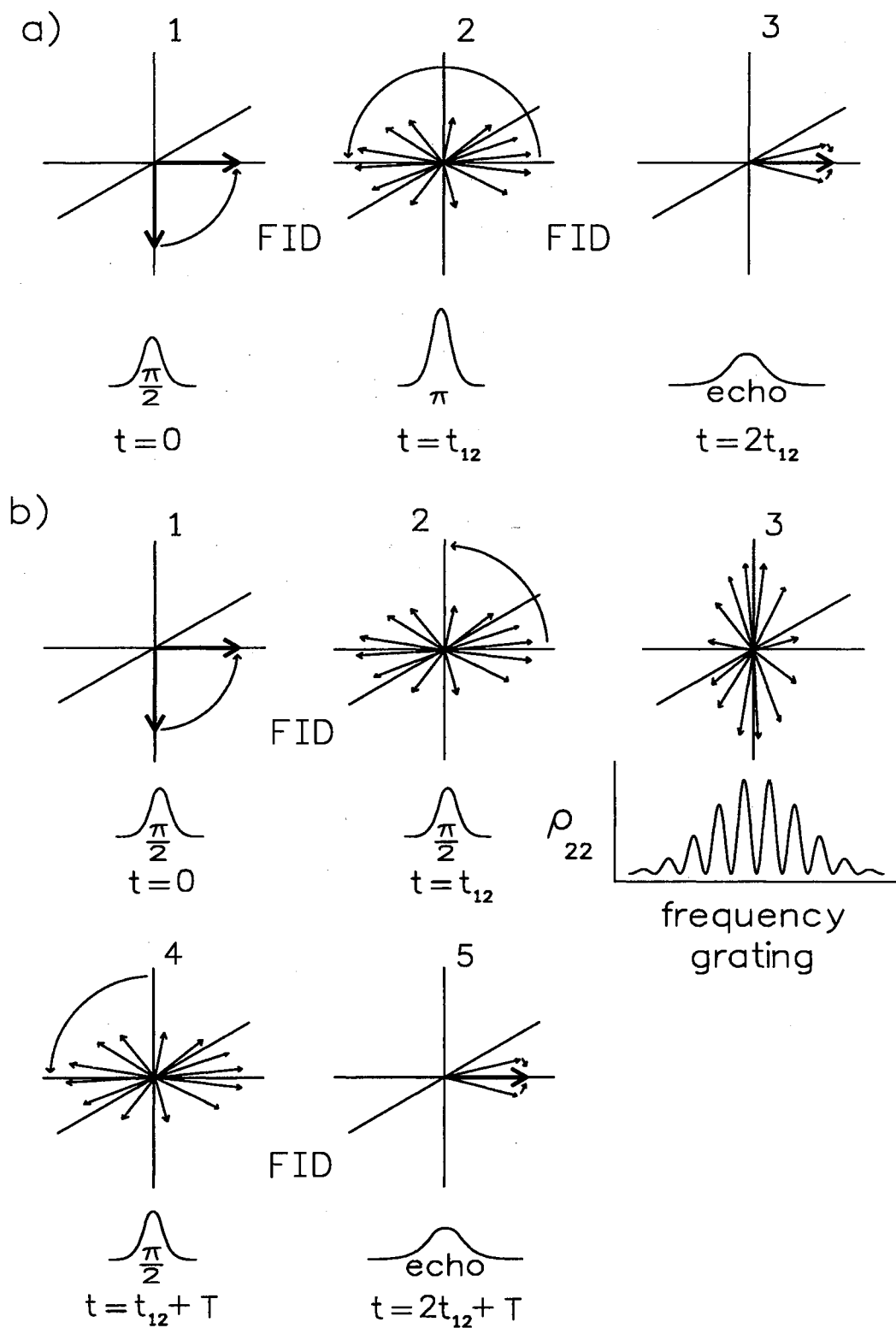


Figure 4. Schematic of the pulse sequence needed to generate a 2-pulse photon echo (a), and a 3 pulse stimulated photon echo (b). The axes and arrows are explained in the text.

drift out of phase with respect to each other due to free induction decay, and incoherent interactions remove some dipoles from being able to be rephased. This is represented by the precession of the individual Bloch vectors within the $\hat{1}, \hat{2}$ plane shown in the second panel of Fig. 4 (b). After a time $t = t_{12}$ a second resonant $\pi/2$ pulse is applied, converting the coherent superposition state to a population in the excited and ground state (the precessed Bloch vectors rotate into the $\hat{1}, \hat{3}$ plane, Fig. 4 (b) panel 3. This can be understood by considering the following: if the transition was not inhomogeneously broadened (all the dipoles oscillate at the same frequency) then after the second $\pi/2$ pulse the entire distribution would be in either the ground or excited state, depending on the duration of time t_{12} and the rate at which the ensemble was being driven between the two states, termed the Rabi frequency, χ , where

$$\chi = \frac{\mu E_0}{\hbar}. \quad (13)$$

In the real world, however, $\Gamma_{inh} \neq 0$ so some dipoles will be “frozen” in the ground state, and others in the excited state, depending on how far from the center of the inhomogeneous distribution the dipole oscillates (called the detuning frequency, Δ). In Appendix B of this thesis, an expression for the population distribution is derived (Eqn.85) after a two-pulse excitation sequence. This expression shows that the excited state frequency distribution of dipoles is proportional to $\cos(\Delta t_{12})$ (and the ground state $1 - \cos(\Delta t_{12})$). This population frequency grating will persist until the population relaxes or spectral diffusion (to be mentioned later) erases it.

At time $t = t_{12} + T$, where $T \leq T_1$, a third $\pi/2$ pulse converts the population distribution back to a coherent superposition state (Fig. 4 (b) panel 4). The individual dipoles retain their phase memory enabling them to drift back into phase, just as in the 2PE case. At time $t = 2t_{12} + T$, the dipoles have rephased and a coherent light signal is emitted which can be detected (Fig. 4 (b) panel 5).

Mention is made of using π and $\pi/2$ pulses to generate the 2PE and the 3PSE. This typically requires pulsed lasers that are capable of producing 10^6 - 10^{12} watts peak power, depending on the oscillator strength of the electronic transition under study. As the width of the excitation pulses decrease (thus enabling

measurement of faster processes), the power required to achieve a π or $\pi/2$ pulse rises quadratically. In practice, it is possible to generate a 2PE or 3PSE with lower intensity pulses, although the PE signal amplitude decreases sharply. This is because whereas a π pulse inverts the entire dipole population, a pulse of only a few milliradians would invert some, but not all of the dipoles.

It is possible to estimate the pulse area (θ) in the glasses used in this study, given that the cross section σ for the ${}^4I_{9/2} \rightarrow {}^4G_{5/2}$ transition in Nd^{3+} : glass is $\sim 10^{-20} - 10^{-21} \text{ cm}^2$. Using this, the transition dipole moment can be estimated from

$$|\mu|^2 = \frac{3n\varepsilon_0 c \hbar \sigma}{2\pi^2} \frac{1}{\nu g(\Delta\nu)} \quad (14)$$

where

- n = index of refraction (~ 1.5)
- ε_0 = permittivity of free space
- c = speed of light
- \hbar = Planck's constant / 2π
- ν = line center frequency ($\sim 5 \times 10^{14} \text{ Hz}$)
- $g(\Delta\nu)$ = normalized lineshape function at
line center ($\sim 2 \times 10^{-13}$) sec.

The transition dipole moment is found to be $\mu \sim 10^{-33} \text{ C}\cdot\text{m}$. Assuming a gaussian excitation pulse envelope, 20 mW average beam power, a pulse repetition rate of 82 MHz, and a beam waist at the focus of $100\mu\text{m}$, the pulse area is calculated to be $\theta \sim 0.02 \text{ mrad}$. This is much less than $\pi/2$ radians, and we expect only a small fraction of the dipole ensemble to be inverted by this excitation field.

The accumulated 3 pulse stimulated echo

It would be advantageous to be able to generate photon echoes by using low peak power lasers, since this would simplify the experimental setup and reduce laser damage to both the samples under study as well as to the optics used in the experiment. As it turns out, this is indeed possible if there exists a third level in the atomic system that can act as a bottleneck in the relaxation path of

excited ions returning to the ground state (see Figure 5). The technique that takes advantage of this bottleneck in the pump cycle is called the accumulated 3 pulse stimulated photon echo (APE). The method of APE uses coherent light pulses of area $\ll \pi$, and compensates for low peak power by relying on a metastable state in the pump cycle that has a population relaxation time $(T_1) \gg T_2$. Therefore, instead of relying on a single two pulse sequence to write a frequency grating, as in a 3PSE, the APE relies on millions of $\theta \ll \pi$ pulse pairs to accumulate over time a ground state population versus frequency grating. Because of the need to use millions of pulse pairs to build up a grating, laser systems used in APE experiments are usually mode-locked lasers having a pulse repetition rate on the order of 100's of MHz. The laser system used in this experiment had a repetition rate of 82 MHz.

After the grating is accumulated, the first (pump) pulse of the two pulse sequence causes some dipoles to return to their coherent superposition state, rephase, and emit a signal after a time t_{12} . This coherent signal is emitted simultaneously with the arrival of the second (probe) pulse. The interference between the probe pulse and the coherent emission results in a slight increase in transmission of the probe pulse, which can be detected with a photomultiplier or photodiode connected to a phase sensitive amplifier. By monitoring the transmitted probe amplitude as a function of the interval between the two excitation pulses (t_{12}), the total dephasing time can be found from Eqn. 117 in Appendix B

$$S(t_{12}) \propto \exp(-2t_{12}/T_2). \quad (15)$$

In this thesis, the (increased) transmitted probe beam amplitude as a function of t_{12} is referred to as the APE signal.

APE technical considerations

Spectral Diffusion

In this section, some of the problems associated with using the APE technique to measure T_2 will be discussed. The first consideration to note is that any dynamic

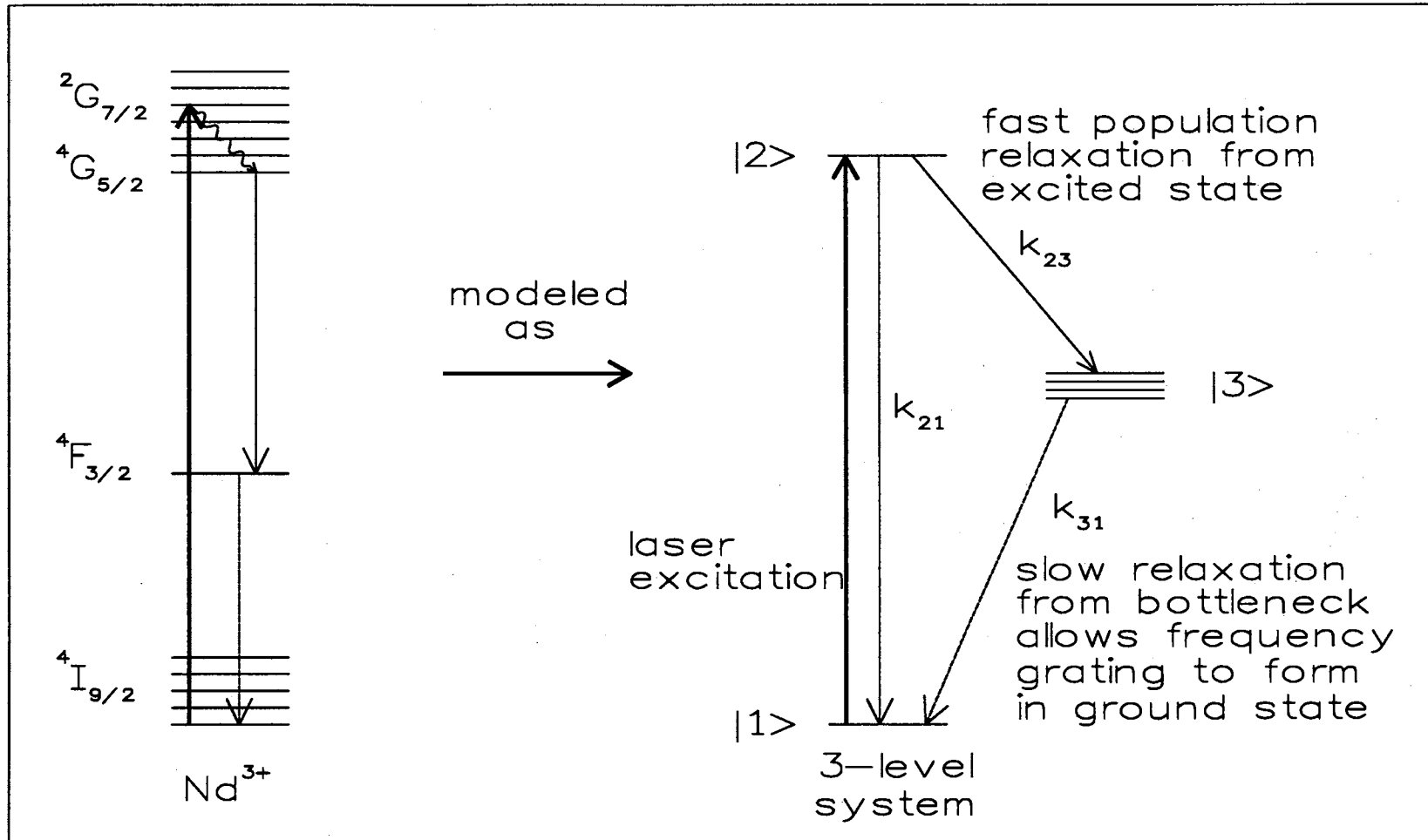


Figure 5. Energy levels of Nd^{3+} and an equivalent 3-level model. k_{ij} denotes the relaxation rate between states i and j .

affecting the ground state frequency grating will also affect the shape of the APE signal, and thus the measured value of T_2 . Spectral diffusion, or energy transfer, is one such dynamic. From Eqn. 85 it can be seen that as t_{12} increases, the grating spacing decreases causing excited state dopant ions to be more prone to transferring their excitation energy to ions not in the excited state. Dopant ions distributed in the peaks of the grating may transfer their excitation to impurities with excitation frequencies located in the grating trough, thus partially erasing the grating. When spectral diffusion is present, the APE signal will anomalously decrease as t_{12} increases, resulting in a nonexponential function.

One check for spectral diffusion is to compare the APE signal from a low impurity doped sample with that from a high doped sample. All things being equal, if the shape of the APE signal remains unchanged for different dopant concentrations, then it is unlikely that spectral diffusion is occurring. We could perform this check on the disordered and pure crystal samples used in this study, but not on the glass samples, since other concentrations were not available.

Pulse Jitter

One systemic variable effecting the frequency grating is excitation pulse jitter. Referring again to the frequency grating function (Eqn. 85) it is apparent that if the phase difference between the pump and probe pulses (ϕ_{12}) changes randomly for each pulse pair, then

$$\langle \cos(\Delta t_{12} - \alpha_{12} + \phi_{12}) \rangle_{Ave} = 0 \quad (16)$$

and a stable grating will not be formed. (In Eqn. 25, Δ = detuning parameter, $\alpha_{12} = (\mathbf{k}_1 - \mathbf{k}_2) \cdot \mathbf{r}$ where \mathbf{k}_1 and \mathbf{k}_2 are the wavevectors of the pump and probe beams.) In fact, any phase jitter at all between the two excitation pulses will only serve to decrease the grating contrast, and reduce the APE amplitude. The experimental setup used in this experiment (see Chapter 1) reduces this problem by splitting the output of the dye laser so that at each value of t_{12} set by the optical delay line, $\phi_{12} = 0$. The only way that random phase fluctuations could play a

role is if the acousto-optic modulator introduces a phase shift in the pump beam. This is unlikely since the undiffracted pump beam was used in the experiment as opposed to using a higher order diffracted beam.

Bottleneck Lifetime

It is worth noting from the above discussion that the duration of the bottleneck state plays a crucial role in determining the APE signal amplitude. In Appendix B, an analytical expression is derived for the APE signal, and mention is made of the “enhancement factor”, γ , which parameterizes the degree to which the frequency grating is enhanced due to the accumulation effect as opposed to that of a single pulse pair. In the limit of $k_{21}, k_{31} \ll k_{23}$ and $T_1 > T$, γ can be written as[6]

$$\gamma = \frac{\exp(-k_{31}T)}{2[1 - \exp(-k_{31}T)]}. \quad (17)$$

Using Eqn. 26 it is possible to approximate the degree to which the accumulated frequency grating enhances the APE signal. For example, an 82 MHz pulse train and a bottleneck lifetime of $1\mu s$ gives an enhancement factor of about 40. Due to the low value of γ as the bottleneck lifetime drops much below $1\mu s$, materials that have sub-microsecond bottleneck lifetimes are generally poor candidates for use with the APE technique.

FID Effects

Several texts discuss free induction decay[8][9][10] and the reader is referred to these for a more detailed discussion of this coherent transient effect. The polarization density of an ensemble of optically active impurities after excitation by a single coherent pulse is given by

$$P(t) = Nex_o Re[\{u_o + iv_o\} \exp(i\omega_o t)] e^{-t/T_2} e^{-t/\Gamma_{inh}} \quad (18)$$

where N is the number density of impurities, ex_o is the transition dipole moment, and ω_o is the center frequency of the inhomogeneous distribution. u_o and v_o are

the initial ($t=0$) values of the coherence parameters u and v defined in Eqns. 5. The important thing to note about $P(t)$ is that it decays at a rate of $1/\Gamma_{inh}$ (since $1/T_2 < 1/\Gamma_{inh}$ typically). If $t_{12} \leq 1/\Gamma_{inh}$, then the probe pulse will interact with the FID polarization induced by the pump pulse. This complicates the analytical APE signal derivation considerably, since extra terms are added which increases the probe beam transmission at small values of t_{12} , therefore the APE signal will no longer be a simple exponential. However, the FID/probe beam interaction has been investigated through numerical simulations.[11][12] Results show that for systems in which the homogeneous linewidth is a fraction of the inhomogeneous width ($T_2' \gg T_2^{inh}$) the FID contribution may be significant if $t_{12} \leq 2T_2^{inh}$. In systems with strong inhomogeneous broadening with $T_2^{inh} \ll \tau_p$, simulations show no appreciable FID contribution. Furthermore, theory shows[11] that choosing an excitation pulsewidth $\tau_p \leq T_2/2$ would enable the measurement of T_2 even if there was a small FID effect. Therefore, FID contributions to the APE signal in the glasses and disordered crystal should not be a problem, however the effect may be noticeable in the crystal.

Phase Jitter at the Detector

As mentioned earlier, the detected APE signal is caused by the interference between a probe pulse and an echo stimulated from the ground state frequency grating by the preceding pump pulse. If the laser phase is unstable over time, the probe beam phase will change relative to the phase of the echo signal, resulting in unwanted amplitude fluctuations at the detector.

While the experiment can be designed to cancel out phase jitter that would affect the frequency grating accumulation, eliminating APE signal amplitude fluctuations at the detector is not as simple. Careful alignment of the laser system is crucial to minimize phase instabilities. Even then, temperature fluctuations in the lab, air currents, building vibrations, and sloppy optical mounts on the laser system all contribute to laser instabilities - hence phase jitter and noise in the APE signal.

Overlapping Stark Levels

This effect is most pronounced in the Nd^{3+} doped systems that are investigated in this thesis. As shown in Figure 5, the ${}^4I_{9/2}$ ground state has 5 Stark levels and the excited ${}^4G_{5/2}, {}^2G_{7/2}$ states has a total of 7 levels. In the glass environment, large inhomogeneous broadening combined with a laser bandwidth of 45 cm^{-1} make it impossible to excite just one Stark component of the multiplet. Usually two or more levels are excited which leads to multiexponential APE signals. Every effort was made to excite the lowest Stark component, however some Stark overlap is still present even at very long wavelengths where the absorption (and APE signal amplitude) is small. The only other alternative is to deconvolute individual decay components from the APE signal, which was also done in this study.

Although the disordered crystals did not exhibit the same degree of inhomogeneous broadening as the glasses, there was still appreciable overlap between Stark components belonging to two different crystal field environments, which will be discussed later. The pure crystal had the least inhomogeneous broadening, but there was still Stark level overlap manifested by a quantum beat phenomena in the APE signal, which will also be discussed later.

CHAPTER IV

RADIATIONLESS RELAXATION AND DEPHASING PROPERTIES Electron-phonon interaction

Single phonon absorption and emission

The phonon absorption and emission rate per unit volume are given by[13]

$$W_{ABS} = \frac{\omega_r^3}{2\pi M v^5 \hbar} \left| \langle \psi_f^{el} | V_1 | \psi_i^{el} \rangle \right|^2 n_r \quad (19)$$

$$W_{EMS} = \frac{\omega_r^3}{2\pi M v^5 \hbar} \left| \langle \psi_f^{el} | V_1 | \psi_i^{el} \rangle \right|^2 (n_r + 1) \quad (20)$$

where

$$\begin{aligned} \omega_r &= \text{frequency of phonon state } r \\ M &= \text{mass of the crystal} \\ v &= \text{average velocity of sound} \\ \langle \psi_f^{el} | V_1 | \psi_i^{el} \rangle &= \text{interaction matrix element} \\ V_1 &= \text{crystal field coupling operator} \\ n_r &= \text{phonon occupation number for the} \\ &\quad r^{\text{th}} \text{ phonon state} \\ &= \frac{1}{\exp(\hbar\omega_r/kT) - 1} \end{aligned} \quad (21)$$

If the total dephasing time depends mainly on phonon absorption in the ground or excited state, then one would expect the dephasing rate to go like

$$\frac{1}{\pi T_2}(T) \propto \frac{1}{\exp(\hbar\omega_r/kT) - 1} \quad (22)$$

and if phonon emission is the main process:

$$\frac{1}{\pi T_2}(T) \propto \frac{\exp(\hbar\omega_r/kT)}{\exp(\hbar\omega_r/kT) - 1} \quad (23)$$

In both cases of single phonon absorption and emission, it can be seen from Eqns. 19 and 20 that the single phonon rates go like ω^3 . If it is possible to measure the dephasing time as a function of frequency of available phonons at constant temperature, then a plot of the total dephasing rate versus phonon frequency should go as

$$\frac{1}{\pi T_2}(\omega_r) \propto \omega_r^3 \quad (24)$$

The derivation of Eqns. 19 and 20 (and Eqn. 28 in the next section), assumes that the phonon distribution can be described by a Debye density of states and (perhaps implicitly) that the host lattice possesses long range translational symmetry. While these assumptions may be valid for crystals, they are inappropriate for glasses and disordered systems. Indeed, the concept of “phonon” in a disordered material is ambiguous and it may be more appropriate to speak of localized vibrational modes instead. Corrections to the use of a Debye density of states will be discussed later in this chapter.

Raman Processes

The density of occupied phonon states is given by the product of the phonon density of states $\rho(\omega)$ and the phonon occupation number $n(\omega)$ given in Eqn. 21:

$$n(\omega_r)\rho(\omega_r) \propto \frac{\omega_r^2}{\exp(\hbar\omega_r/kT) - 1} \quad (25)$$

In the event that an energy gap is bridged by a single phonon transition of energy $\hbar\omega_r$ such that

$$\hbar\omega_r \ll kT \quad (26)$$

Eqn. 25 shows that there are fewer phonons available at ω_r compared to those available at energies closer to kT . In situations such as this, Raman processes may occur in which a phonon of frequency ω_a is absorbed and another of frequency ω_e emitted such that

$$\omega_a - \omega_e = \omega_r. \quad (27)$$

The transition probability of such a process is given by[13]

$$W_{raman} = A \left(\frac{T}{T_D} \right)^7 \int_0^{\frac{T_D}{T}} \frac{x^6 e^x}{(e^x - 1)^2} dx \quad (28)$$

where

$$\begin{aligned} T_D &= \text{Debye temperature} = \frac{\hbar\omega_D}{k} \\ \omega_D &= \text{Debye cutoff frequency} \\ A &= \frac{36}{\rho^2 v^{10} 8\pi^3} \left| \langle \psi_f^{el} | V_2 | \psi_i^{el} \rangle + \sum_l \left[\frac{\langle \psi_f^{el} | V_1 | \psi_i^{el} \rangle \langle \psi_i^{el} | V_1 | \psi_i^{el} \rangle}{E_i^{el} - E_l^{el}} \right] \right|^2 \\ \rho &= \text{density of the material} \\ v &= \text{velocity of sound in the material} \\ V_1 &= \text{first order crystal field coupling operator} \\ V_2 &= \text{second order crystal field coupling operator} \end{aligned} \quad (29)$$

Since the Raman process involves two phonons, it is second order in the interaction Hamiltonian matrix elements, and so is less probable than a single phonon process that is first order. Of course, if Eqn. 26 holds then a Raman process could occur.

In the limit $T \gg T_D$, the integral in Eqn. 28 becomes a constant, and the Raman pure dephasing rate goes as

$$W_{raman} \propto T^7. \quad (30)$$

In the high temperature limit, $T \geq 0.5T_D$, the rate goes as

$$W_{raman} \propto T^2. \quad (31)$$

In the glasses studied in this experiment, and indeed most glasses[14], the dephasing rate has a quadratic temperature dependence down to 9K. This result is contrary to the conditions on Eqn. 31. One would expect a quadratic temperature dependence at temperatures above ~ 100 K, since the Debye temperature for inorganic glasses is about 10^2 K (for vitreous silica, $T_D = 495$ K[15]).

The low temperature quadratic temperature dependence of optical linewidths in glasses has been explained in several ways. At very low temperature ($T < 4$ K),

the temperature dependent part of the linewidth was successfully modeled as arising from interactions between the impurity centers and an ensemble of two-level systems (TLS)[16][17]. Assumptions necessary for the TLS model are generally not valid at temperatures in the range 10-100K, however. Another proposed theory makes use of localized vibrational modes.[18]

Since there is no reason to assume that in glasses the physical mechanism of Raman scattering of phonons is invalid, other efforts to explain low temperature T^2 dependence have postulated that the Raman scattering mechanism is correct. Instead, changes have been made to assumptions regarding the density of states and the Debye temperature. One premise in the standard Debye model is that the phonon density of states function is determined by a host with translational symmetry. Glasses, on the other hand, lack such symmetry but do possess a dilational symmetry arising from the rings formed by covalent bonds between network former and modifier atoms. Whereas phonons arise from quantized vibrations for a system with translational symmetry, a type of pseudo particle called “fractons” describe quantized vibrations of a system with dilational symmetry. Noting that glasses do not necessarily possess the translational symmetry required for normal mode analysis used in the Debye model, a theory based on Raman scattering of fractons was developed[19] and successfully applied to explain the T^2 linewidth dependence in FLN experiments on Eu^{3+} : glasses.[20][21]

Another premise central to the standard Debye model regards the Debye temperature (T_D) used in Eqn. 28 to calculate W_{Raman} . As noted earlier, the standard Debye temperature is too large to allow a scattering rate with a quadratic temperature dependence down to ~ 10 K. Drawing on experimental evidence for the existence of a low energy maximum (called the Boson peak) at frequency Δ_p in the phonon density of states, Huber[22][23] reevaluated the Raman contribution to the linewidth. In the low frequency (“acoustic”) regime $\rho(\omega)$ increases as ω^2 up to a maximum frequency of Δ_p . At frequencies above Δ_p , $\rho(\omega)$ is associated with variations in optic-like modes of the glass. By dividing the phonon spectrum into these two regions and applying a short wavelength approximation to the “optical”

region ($\hbar\omega_r > \Delta_p$) in which the electron-lattice Hamiltonian varies as

$$H_{el} \propto \frac{1}{\sqrt{\omega}} \quad (32)$$

instead of the long-wavelength approximation

$$H_{el} \propto \sqrt{\omega} \quad (33)$$

used in deriving Eqn. 28, it can be shown that the Raman pure scattering rate varies as T^2 for $T \geq 0.4\Delta_p/k$. Measurements made on ED2 silicate glass[24] found the Boson peak to be $\Delta_p = 90\text{cm}^{-1} \pm 20\%$, showing that T^2 dependence due to Raman scattering may persist down to 50K in this host. At lower temperatures the temperature dependence gradually becomes cubic. Only at temperatures $T \ll \Delta_p/k$ does the temperature dependence go as T^7 .

Both the fracton model and the effective T_D model correctly predict low temperature quadratic temperature dependence of the homogeneous linewidth. While the fracton model is satisfying in that it treats the difference in symmetry between glasses and crystals at a fundamental level, it is esoteric, having as its underpinning mathematical constructs called fractals. The effective T_D model ignores microscopic differences in symmetry between crystals and glasses, reasoning instead that the electron-phonon coupling Hamiltonian should be treated differently for low frequency modes as opposed to high frequency modes.

Results for glasses

Figure 6 show the temperature dependence of the dephasing rate ($1/\pi T_2$) for the lowest Stark energy level of the ${}^4I_{9/2} \rightarrow {}^4G_{5/2}, {}^2G_{7/2}$ transition of Nd^{3+} in ED2 silicate glass. In this figure, a low temperature intercept of 15.2 GHz has been subtracted from the data, which are shown in Table II in Appendix C. The solid line in Fig. 6 is the function $Y = 2.6 \times 10^{-3}T^{2.4 \pm 0.2}$ which is close to the $T^{2.2}$ dependence found previously in measurements made in $\text{Nd}^{3+}:\text{ED2}$. [25]

APE measurements in ED2 made by reference [25] exhibited single exponential APE signals up to approximately 586.5 nm. Measurements at shorter

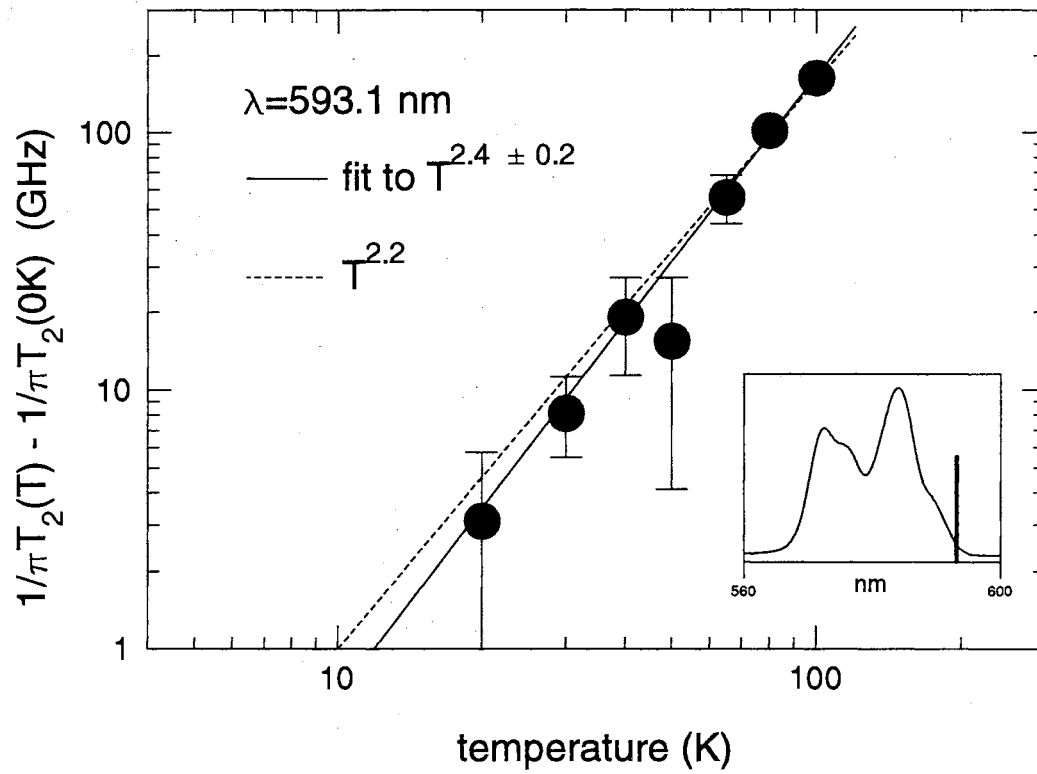


Figure 6. Temperature dependence of the dephasing rate in $\text{Nd}^{3+}:\text{ED2}$ silicate glass at $\lambda = 593.1$ nm. Insert shows the position of the excitation wavelength relative to the absorption spectrum.

wavelengths were characterized by nonexponential decays. In this experiment, all the APE signals in ED2 were nonexponential, and could be fit to a sum of two single exponential functions, as shown in Fig. 9(a). This is most likely due to the increased bandwidth of our laser compared to that used by reference [25]. Although no bandwidth information is explicitly given in [25], the pulsewidth is given as 5 ps. Our pulsewidth was about 0.5 ps, with a spectral FWHM of 1.5 nm (45cm^{-1}). This would imply that the laser used by [25] had a spectral width of $\sim 0.15\text{nm}$ which would considerably increase site selectivity and reduce excitation of multiple Stark energy levels. This would be manifested by single exponential APE signals down to wavelengths where the Stark components are closer together, and some overlap is unavoidable.

In this experiment, we excited at 593.1nm and found that the long component of the APE signal stayed more or less constant up to about $T=65\text{K}$, then it increased abruptly as shown in Table II. This is caused by a thermally activated single phonon process in the ground state. Although no data are available regarding the ground state Stark splitting in ED2 silicate glass, fluorescence line narrowing (FLN) experiments on LGS-28 silicate glass [26] suggest a ground state splitting of $\sim 25\text{cm}^{-1} - 87\text{cm}^{-1}$. Our laser bandwidth of 45cm^{-1} would overlap the 1st Stark level, which would become significantly populated at 65K. The constant ($\sim 25\text{ps}$) component of the APE signal corresponds to nonradiative population relaxation from higher lying excited state Stark level. Figure 7 shows the approximate locations of several Stark levels within the ${}^4G_{5/2}, {}^2G_{7/2}$ multiplet, found by numerically deconvoluting the low temperature absorption spectrum in ED2. The positions and widths of the gaussian functions are listed in Table I in Appendix C. Based on Fig. 7, it can be seen that excitation at 593.1nm would in all likelihood excite the three lowest Stark energy levels.

Reference [25] found the low temperature ($T=1.6\text{K}$) intercept to be 2.9 GHz ($T_2 = 110\text{ps}$), which remained constant up to 5K. This intercept was attributed to relaxation of the population in the lowest Stark level of the ${}^4G_{5/2}, {}^2G_{7/2}$ multiplet to other lower-lying electronic states of the Nd^{3+} ion. In our experiment, we found

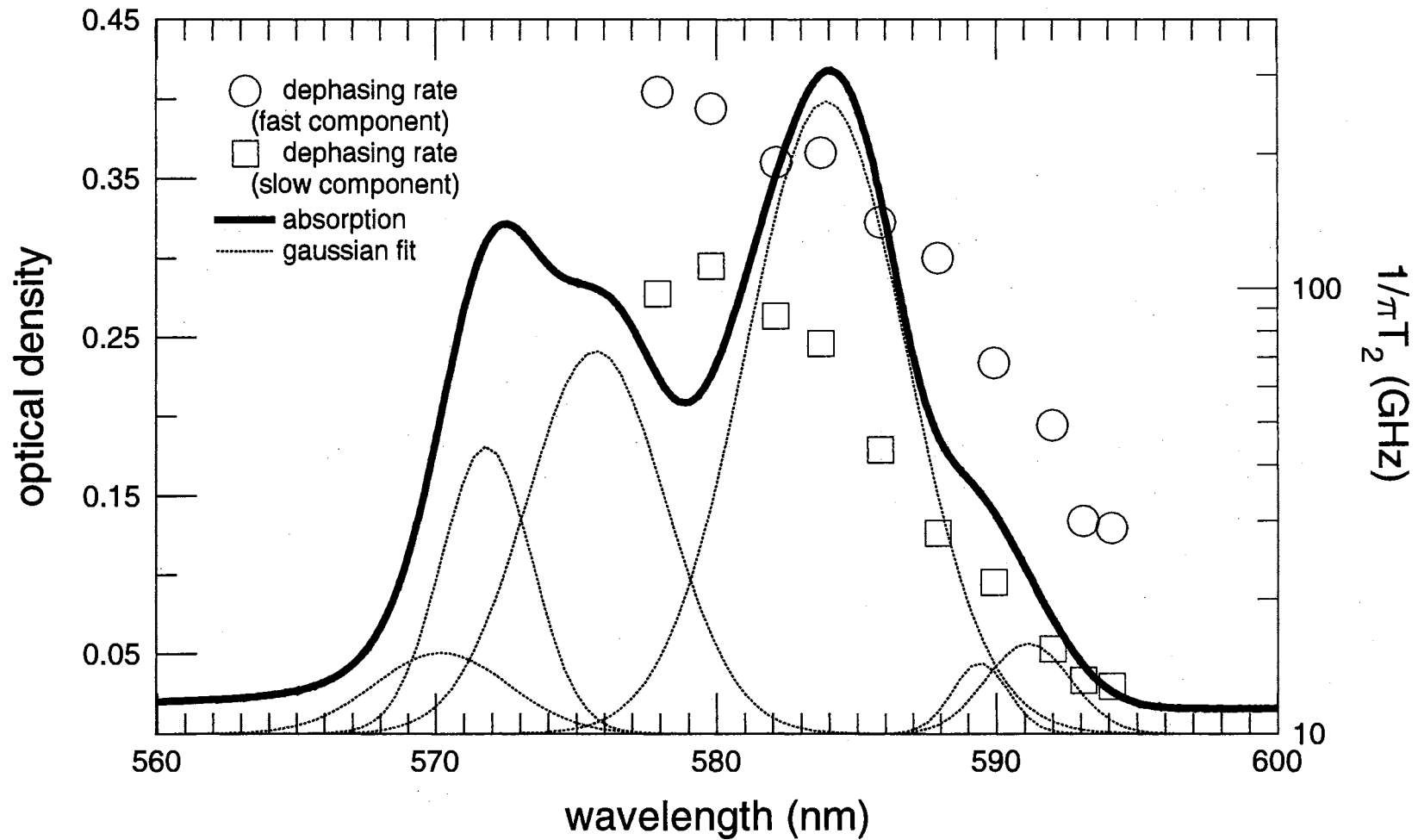


Figure 7. Absorption spectrum (left axis) of ED2 silicate glass: Nd_2O_3 (2.0 wt.%) at 9K and approximate Stark level locations. Open circles and squares denote the total dephasing rates (right axis).

$1/\pi T_2$ (T=0K) to be 15.2 GHz and 6.4 GHz, which is similar to that measured by reference [27], who used a broadband laser similar to the one used in our study.

This information indicates the following. Our laser excitation excited the lowest three excited state Stark energy levels in the ED2 sample. The relaxation from the lowest component, which would have been manifested as a long tail on the APE signal, was masked by the much faster relaxation from the second and third Stark components. The two principle population relaxation times of $T_1 = 5.3\text{ps}$ and $T_1 = 12.5\text{ps}$ found from

$$T_2 = 2T_1 \quad (34)$$

correspond to relaxation across energy gaps of approximately 40cm^{-1} and 200cm^{-1} .

Temperature dependence measurements were made of $1/\pi T_2$ across the inhomogeneously broadened ${}^4I_{9/2} \rightarrow {}^4G_{5/2}, {}^2G_{7/2}$ absorption profile. Although the signal to noise ratio improved at wavelengths shorter than 593.1nm, results were uninterpretable due to a large degree of scatter in the data caused by the laser bandwidth overlapping multiple Stark levels.

The $1/\pi T_2$ temperature dependence in the germanate glass is shown in Table IV and Fig. 8 where a low temperature intercept of 11 GHz has been subtracted. The measurements were made at 594.0nm, at the long wavelength edge of the absorption spectrum, as shown in the inset of Fig. 8. Unlike the silicate glass, the APE signal decay could be described by a single exponential function at all temperatures, as shown in Fig. 9 (b). This is likely due to the fact that, relatively speaking, we probed further out in the wings of the absorption than we did in the silicate, and therefore minimized contribution from overlapping Stark levels. The temperature dependence of $1/\pi T_2$ can be fit to a $T^{2.25 \pm 0.10}$ function, which is consistent with the $T^{1.7} - T^{2.3}$ dependence characteristics of rare-earth doped glasses.[14]

Figure 11 and Table VI illustrate the temperature dependence of the dephasing rate in the UP77 lithium phosphate glass sample at 589.9 nm. The dephasing

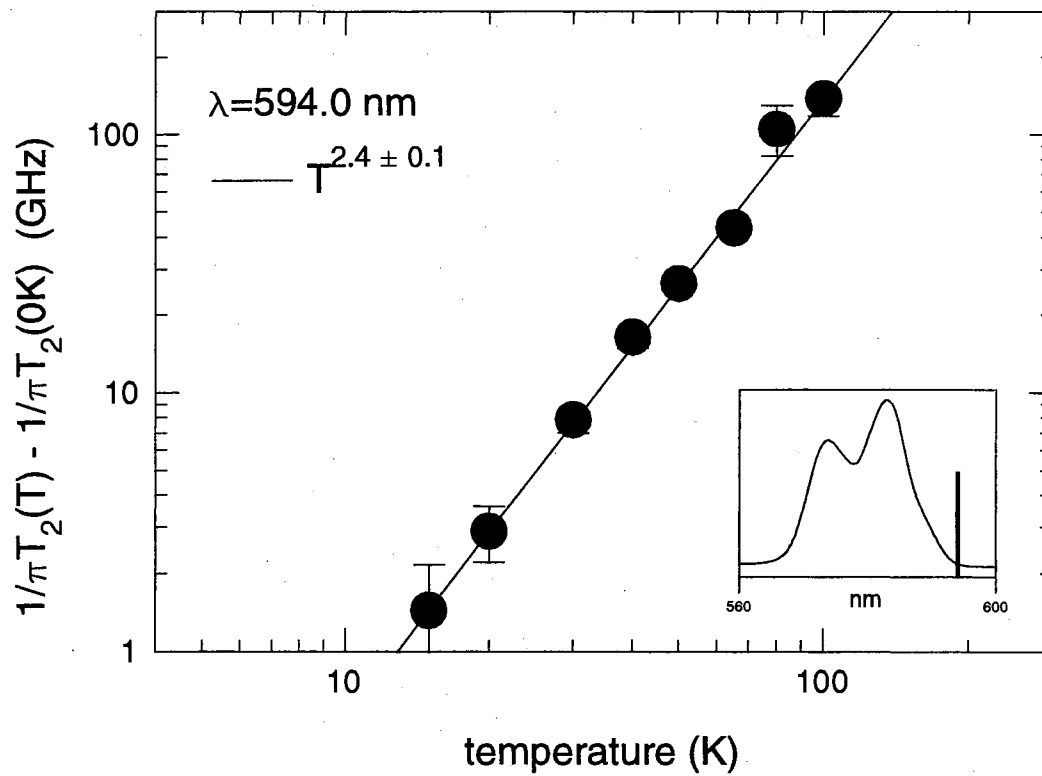


Figure 8. Temperature dependence of the dephasing rate in Nd^{3+} : lithium germanate glass at $\lambda = 594.0$ nm. Insert shows the position of the excitation wavelength relative to the absorption spectrum.

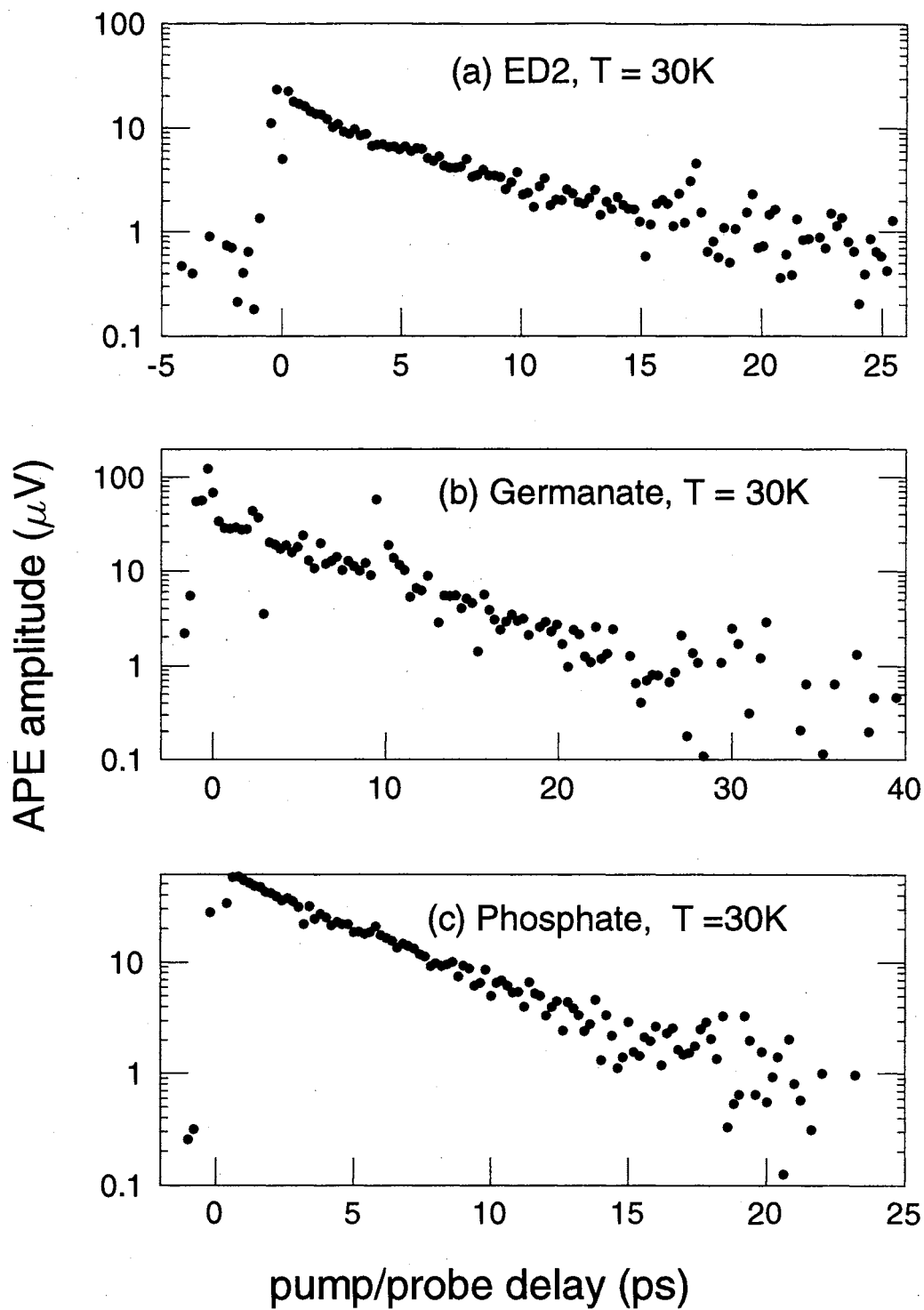


Figure 9. APE signal functions in three glasses at 30K: (a) ED2 silicate, $\lambda = 593.1\text{nm}$, (b) lithium germanate, $\lambda = 594.0\text{nm}$ (c) lithium phosphate, $\lambda = 589.9\text{nm}$.

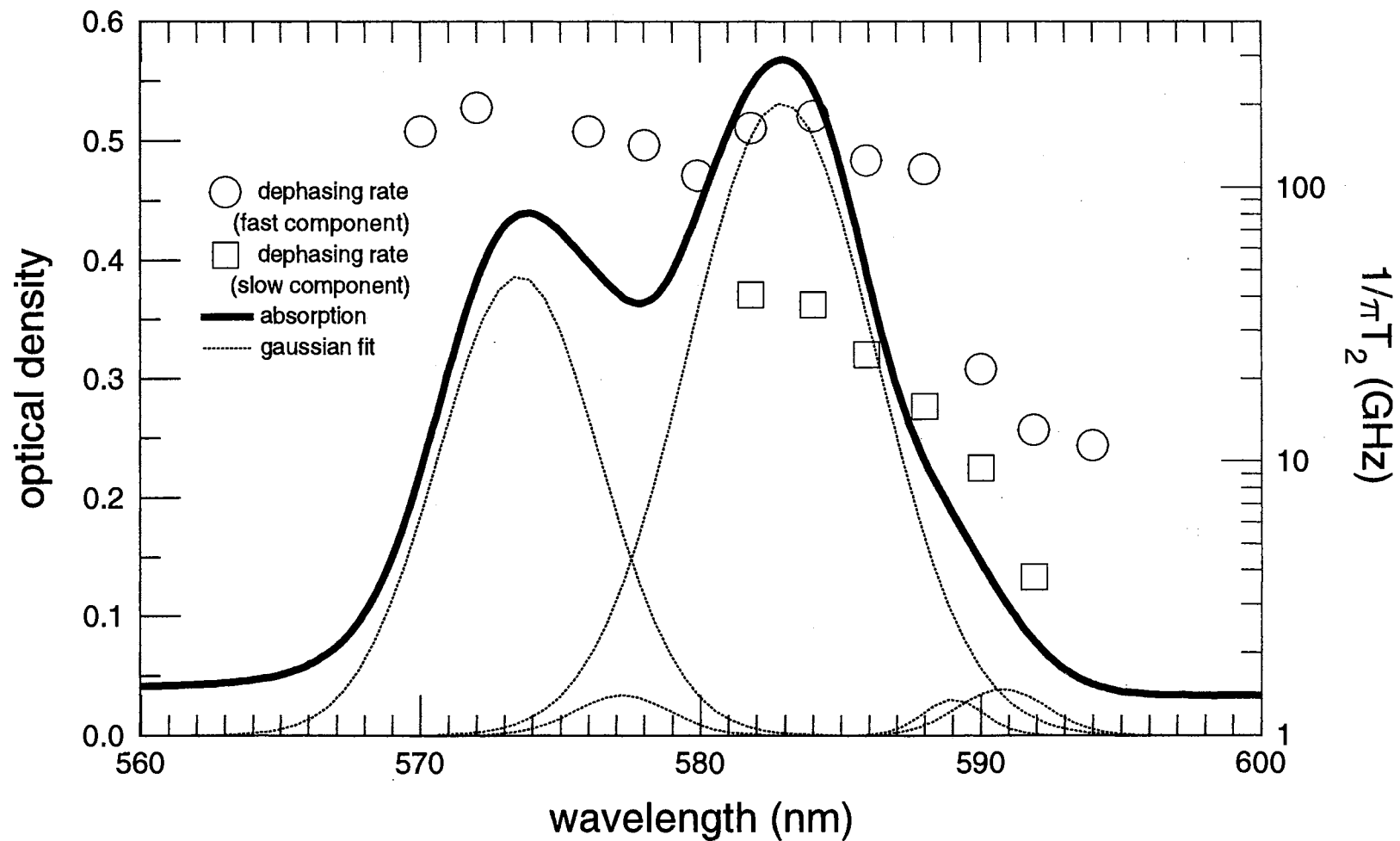


Figure 10. Absorption spectrum (left axis) of lithium germanate glass: Nd_2O_3 (2.0 wt.%) at 9K and approximate Stark level locations. Open circles and squares denote the total dephasing rates (right axis).

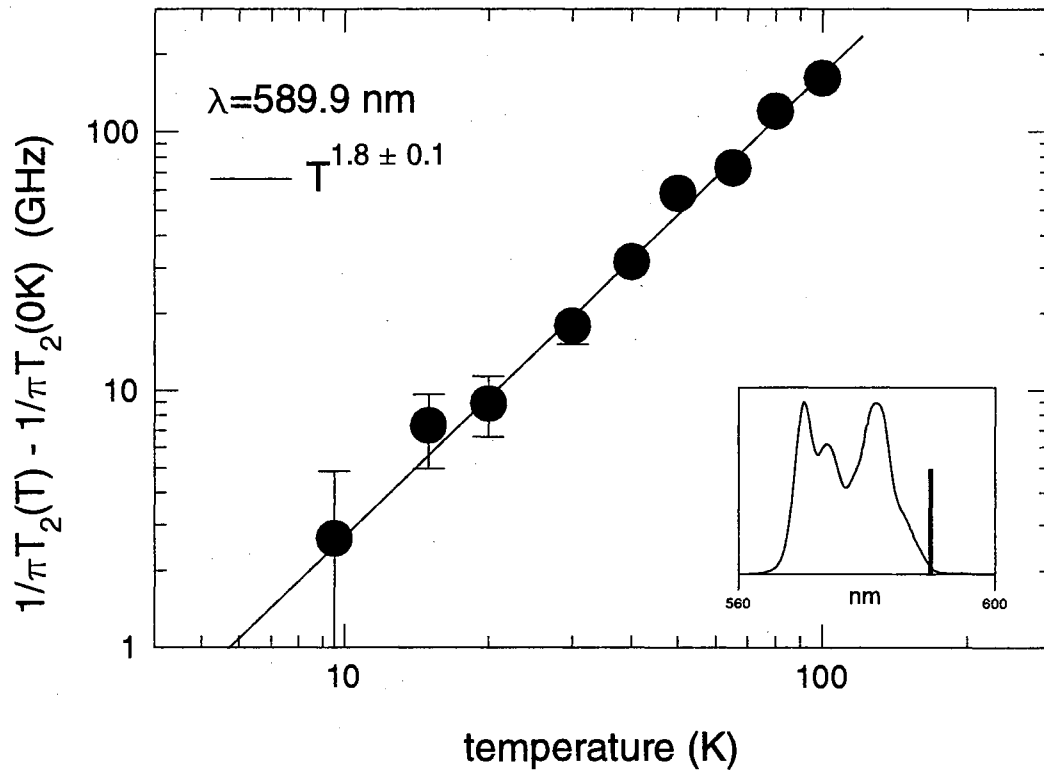


Figure 11. Temperature dependence of the dephasing rate in Nd^{3+} : lithium phosphate glass at $\lambda = 589.9 \text{ nm}$. Insert shows the position of the excitation wavelength relative to the absorption spectrum.

rate of the lowest excited state Stark level could be modeled by a $T^{1.8\pm 0.1}$ temperature dependence with a low temperature intercept of 19 GHz. As with the lithium germanate sample, the phosphate glass host produced APE signals that could be described by a single exponential function between 10K and 100K, as shown in Fig. 9(c). A previous study of the luminescence decay kinetics of Nd^{3+} :lithium phosphate glass concluded that only a very small variation in optical transition probabilities exists for different optical centers in this host material. [26] This helps explain the narrower features of the UP77 absorption spectrum shown in Fig. 12 It may also suggest a reason for the single exponential APE signals at long wavelengths, since a smaller inhomogeneous linewidth would serve to reduce Stark overlap.

The dependence of $1/\pi T_2$ on the excitation energy in ED2 is shown in Figs. 7, 13 (a), and in Table III. The relation is approximately linear in energy. Also shown in Figs. 13 (b) and (c) are the dephasing rates of the germanate and phosphate glasses. These show a ω^3 dependence up to a value of about 180 GHz, which is the resolution cutoff due to the laser pulsewidth. The data suggest a single phonon emission mechanism (Eqn. 20) for low temperature relaxation in the phosphate and germanate glasses. Single phonon absorption can be disregarded, since the ratio of single phonon emission to single phonon absorption processes is given by Eqns. 19, 20, and 21 as

$$\frac{W_{ems}}{W_{abs}} = \exp(\Delta E/kT). \quad (35)$$

At a temperature of 9.5K, single phonon absorption processes can be neglected in the energy range of $\sim 30 - 300 \text{ cm}^{-1}$, which is the range in which the dephasing rate is a monotonically increasing function of energy, as shown in Fig. 13.

The linear energy dependence of the dephasing rate in the silicate glass is more difficult to explain. FLN studies of Eu^{3+} : lithium silicate glass show the low temperature linewidth increasing linearly with excitation energy across the inhomogeneously broadened ${}^7F_0 \rightarrow {}^5D_0$ transition. [20][21] This variation of low temperature linewidth is explained as being a measure of the density of differing crystal field sites across the inhomogeneously broadened transition. Since the

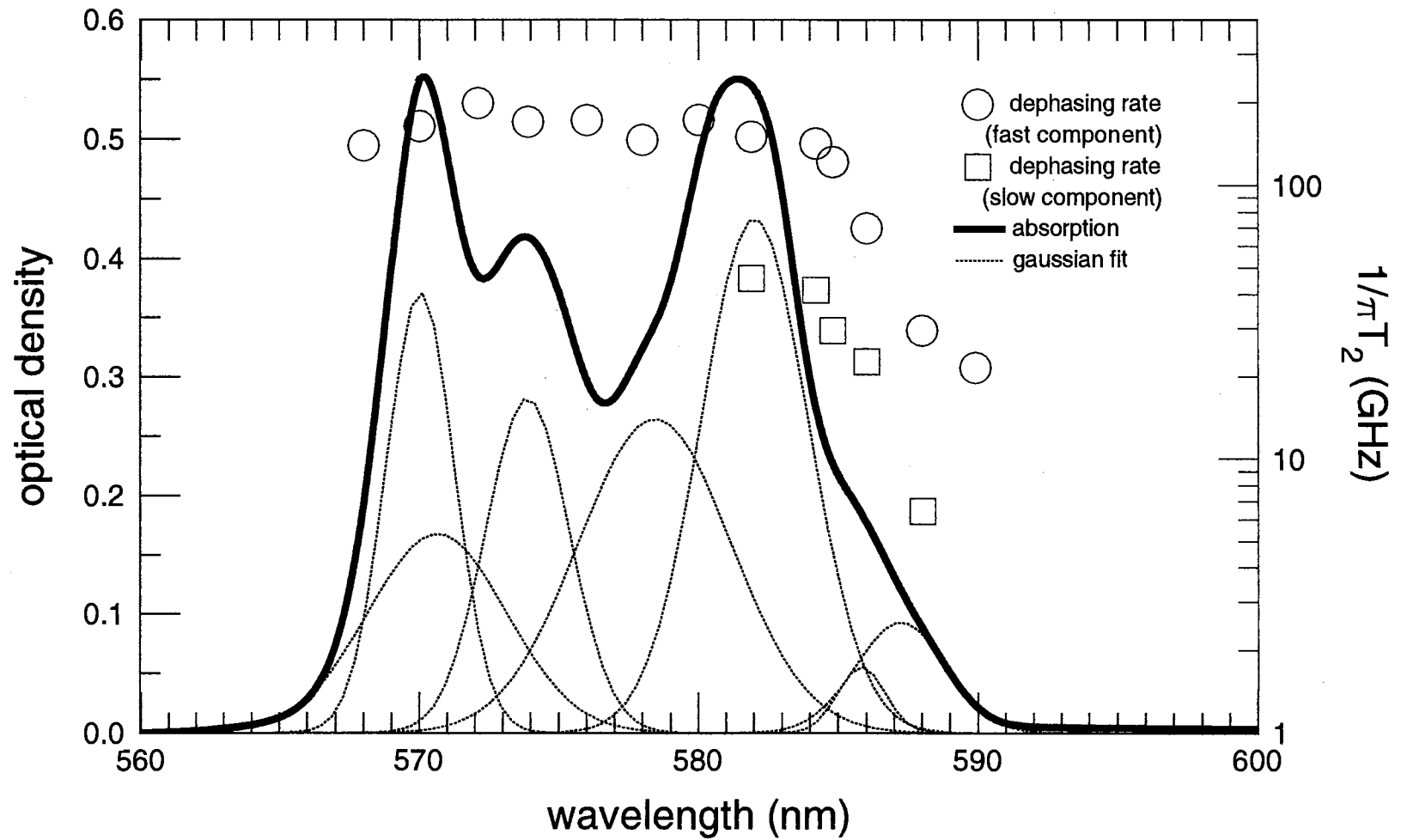


Figure 12. Absorption spectrum (left axis) of UP77 phosphate glass: Nd_2O_3 (0.5 wt.%) at 9K and approximate Stark level locations. Open circles and squares denote the total dephasing rates (right axis).

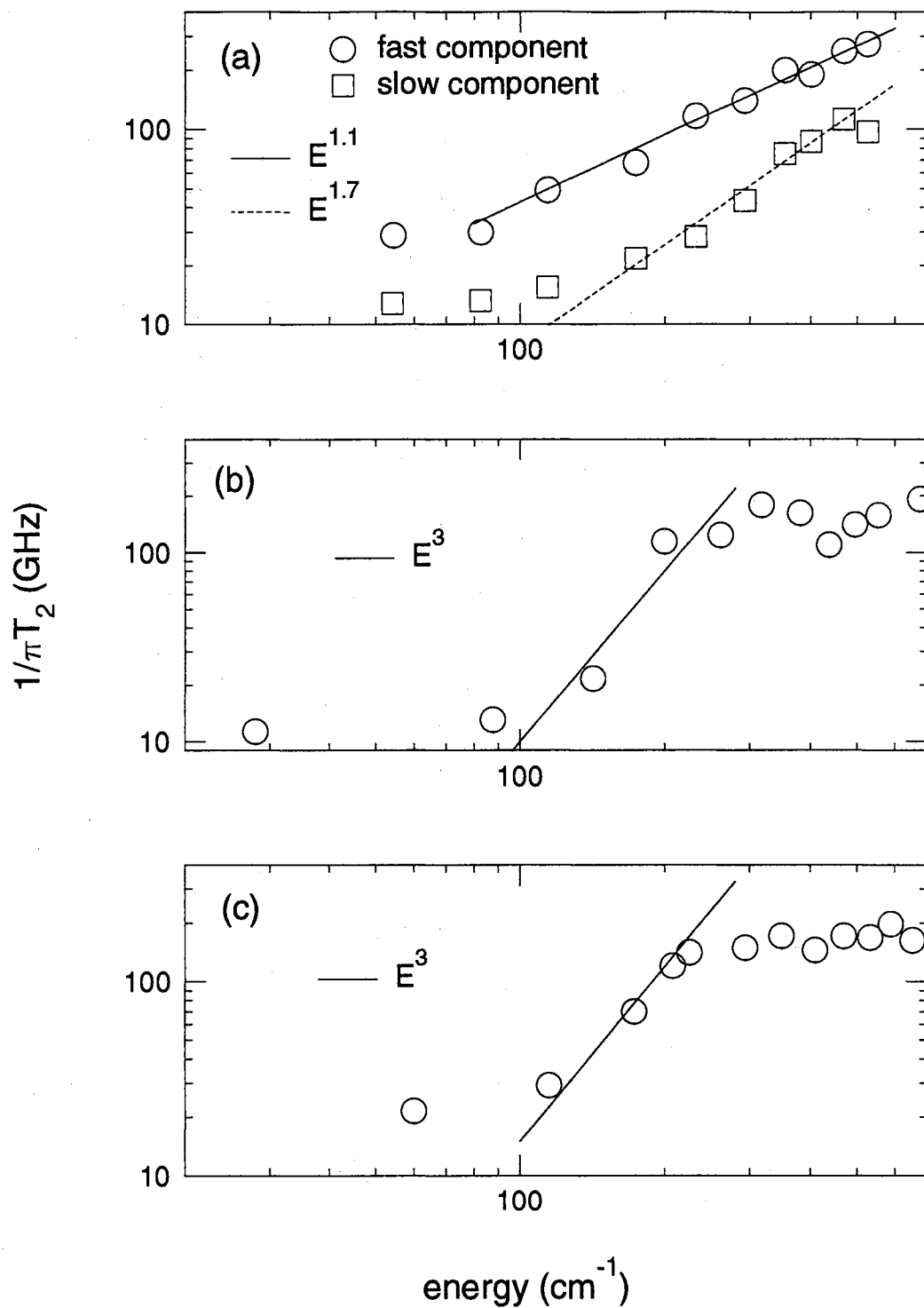


Figure 13. Dependence of dephasing rate on excitation energy at 9.5K in Nd^{3+} doped glasses. (a) ED2 silicate, (b) lithium germanate, (c) lithium phosphate.

transition studied was a singlet transition, single phonon emission could be disregarded. Reference [25] notes the increase of $1/\pi T_2$ with excitation energy in Nd^{3+} : ED2 glass between 580 and 595 nm, and attributes it to population relaxation from higher lying Stark levels to lower ones. From graphs in reference [25], $1/\pi T_2 \propto E^2 - E^4$.

Earlier in this chapter, it was noted that the exponential APE signals in the phosphate and germanate glasses compared to the nonexponential signals in the silicate glass could be an indication of increased inhomogeneous broadening of the silicate host compared to that of the phosphate and germanate glasses. If this is true, it may be possible to explain the linear frequency dependence of the dephasing rate in ED2 in terms of competition between two physical mechanisms. The dephasing rate increases almost linearly across a single Stark level in silicates due to changes in local crystal field strength. We also know that it can increase cubically due to single phonon emission to lower Stark levels. If Nd^{3+} is in a host (such as ED2) which causes greater inhomogeneous broadening, then the linear effect may dominate. The smaller inhomogeneous linewidth of the phosphate may allow the cubic effect to be dominant. Further testing of this hypothesis is needed in Nd^{3+} : glasses with varying inhomogeneous linewidths.

Results for disordered crystal

Whereas glasses have a continuous set of optical centers that correspond to a smooth change of ligand field parameters from site to site, our disordered crystals have two discrete groups of optical centers, denoted as I and II. These correspond to Nd^{3+} ions located in different low-symmetry crystal field environments, in which the II center possesses symmetry lower than that of the I center.[28] For each of these two groups of centers, variation of crystalline field leads to large inhomogeneous line broadening.

Figure 14 shows the absorption spectrum of Nd^{3+} ions in the 4% NdF_3 :yttrium fluorite crystal at $T=9.5\text{K}$. This spectrum corresponds to the ${}^4\text{I}_{9/2} \rightarrow {}^4\text{G}_{5/2}, {}^2\text{G}_{7/2}$ transition for the two optical quasicenters. The inhomogeneously broadened 580

and 579 nm lines correspond to transitions between the lowest Stark levels of the ${}^4I_{9/2}$ and ${}^4G_{5/2}, {}^2G_{7/2}$ multiplets for the II and I quascenters respectively. The 576.4 nm line corresponds to a transition to the second Stark level of ${}^4G_{5/2}$ state for the I center[28]. The splitting between the first and second Stark level of the ${}^4I_{9/2}$ ground state is 83 cm^{-1} (I center) and 208 cm^{-1} (II center). Low temperature fluorescent lifetimes for the ${}^4F_{3/2}$ metastable state are equal to 630 and 400 μs for the I and II centers, respectively.

Figure 15(a) shows an APE decay curve at $T=9\text{K}$ for excitation of the I center ($\lambda_p = 578.7\text{nm}$). Nearly all of the echo decay curves at each λ_p and T consisted of more than one exponential component. The nonexponential nature of APE decays was also noted in the previous section on glasses, and $\text{Nd}^{3+}:\text{YAG}$ crystals.[29]

The dependence of the dephasing rate $1/(\pi T_2)$ on excitation wavelength (λ_p) is shown in Fig. 14. In the temperature range of 9-50K, nearly all the echo decay curves could accurately be described by a sum of two exponentials. Thus we show two values of the dephasing rate for each λ_p which correspond to the two decay times. The open circles correspond to broadband excitation ($\Delta\lambda_p = 1.5 \text{ nm}$), and the filled circles to narrowband excitation ($\Delta\lambda_p = 0.3 \text{ nm}$). In both cases the pump beam power was about 20 mW. At $T=9\text{K}$ the minimum value of $1/\pi T_2$ for the ${}^4I_{9/2} \rightarrow {}^4G_{5/2}, {}^2G_{7/2}$ transition of Nd^{3+} is 10-20 times less for this crystal than for the Nd^{3+} doped glasses of the previous section in which T_2 was limited by the population relaxation time T_1 . This difference of T_2 could be attributed to a smaller maximal energy of optical phonons for these crystals and, consequently, to a lower probability of nonradiative relaxation from ${}^4G_{5/2}$ to lower states. Raman spectra of $\text{CaF}_2\text{-YF}_3$ shows a density of phonon states that has broad overlapping bands stretching from 0 to 600 cm^{-1} as shown in Fig. 16.

The maximum optical phonon energy of silicate, germanate, and phosphate glasses is over 1000 cm^{-1} , which is nearly twice that of the mixed crystal.[3]

The excitation of the second Stark component of the ${}^4G_{5/2}, {}^2G_{7/2}$ state for the I center ($\lambda = 576.7\text{nm}$) leads to more than a 10 fold increase of phase relaxation rate. This increased rate is most likely associated with a single phonon transition

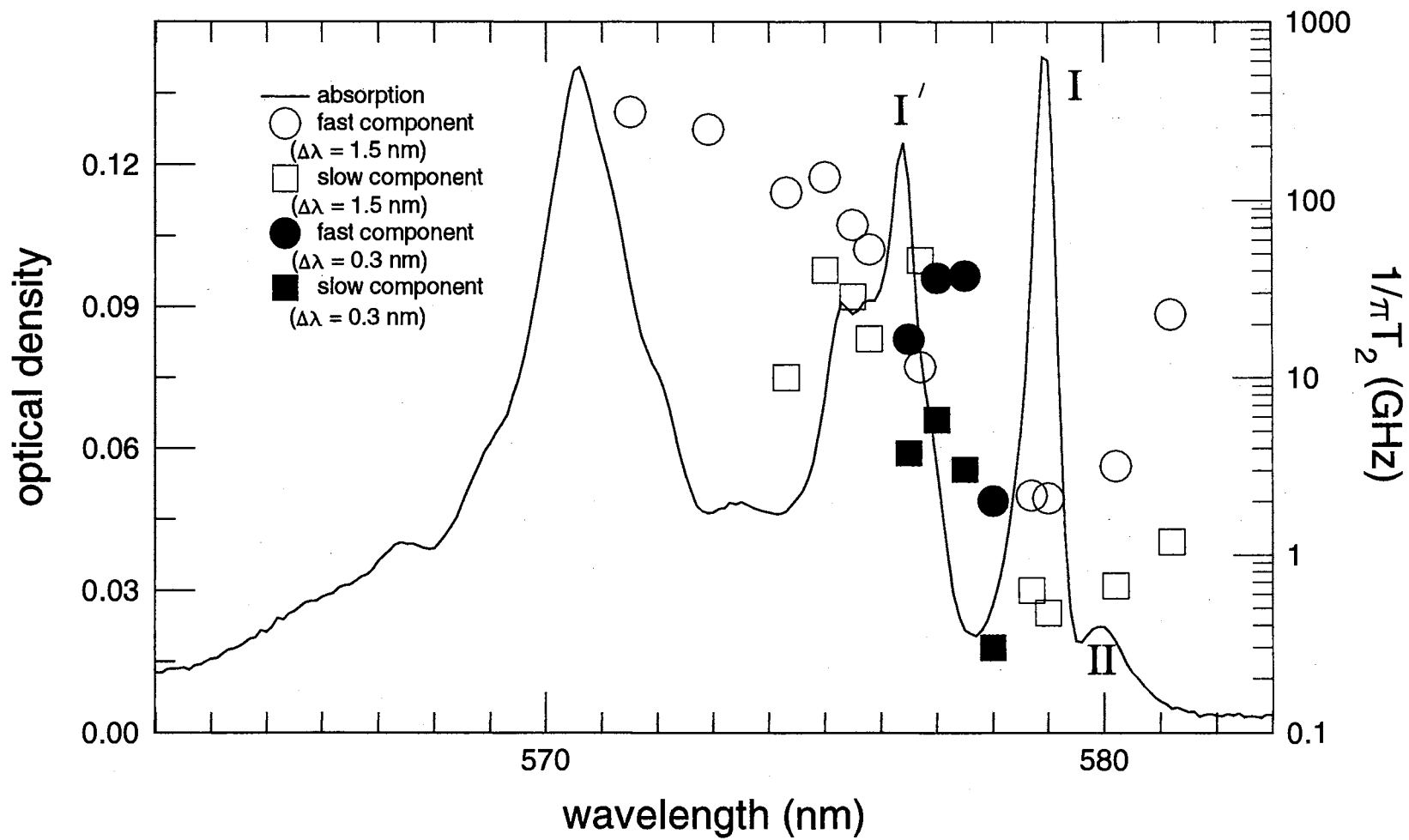


Figure 14. Absorption spectrum of $\text{CaF}_2\text{-YF}_3(12\text{wt.}\%) - \text{NdF}_3(0.1\text{wt.}\%)$ disordered crystal at 9K (left axis) and total dephasing rate (right axis).

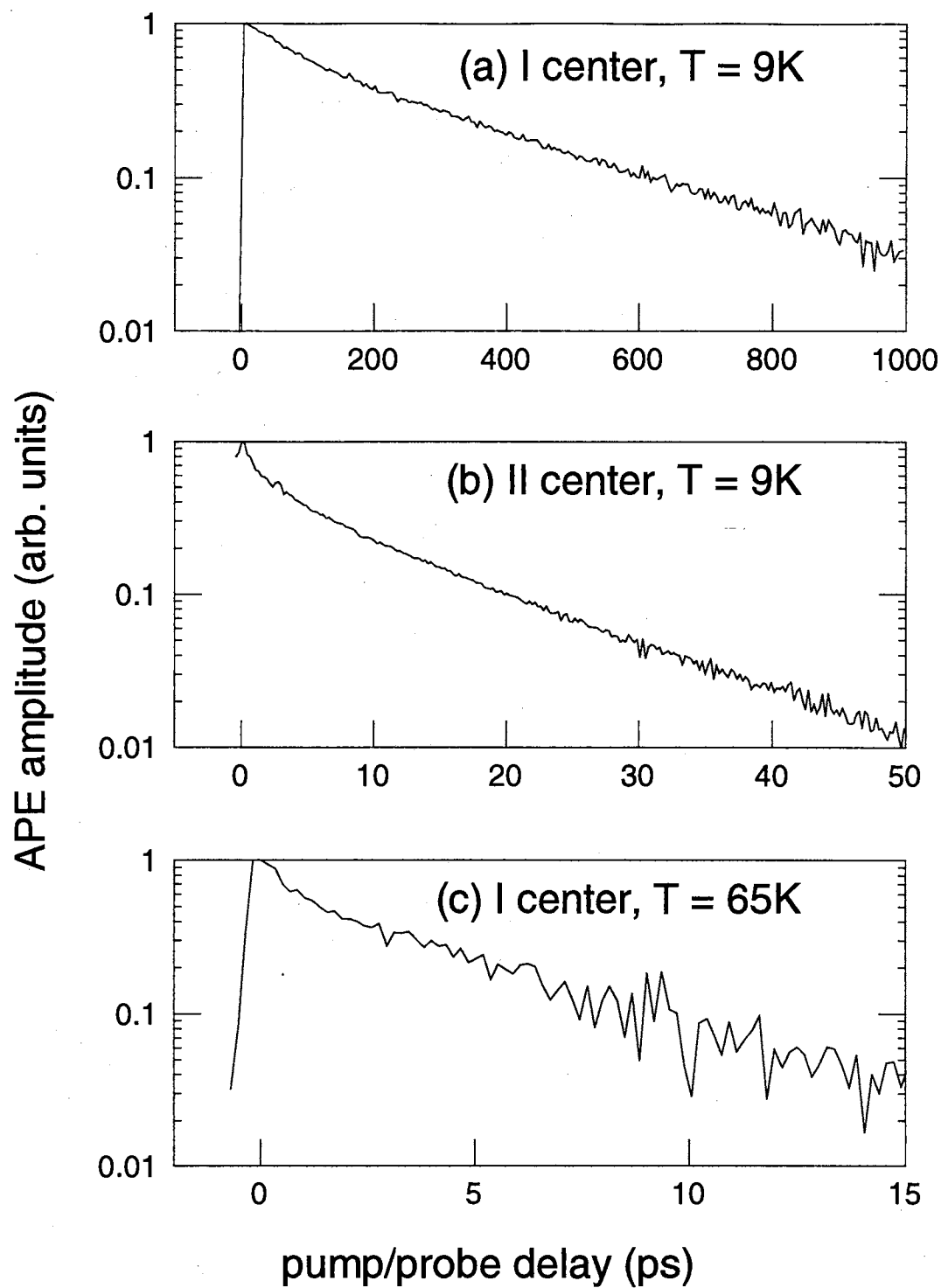


Figure 15. Accumulated photon echo signals in $\text{CaF}_2 - \text{YF}_3(12\text{wt.}\%):\text{NdF}_3(4\text{wt.}\%)$ for (a) 579.0 nm, $T=9\text{K}$; (b) 576.7 nm, $T=9\text{K}$; (c) 579.0 nm, $T=65\text{K}$.

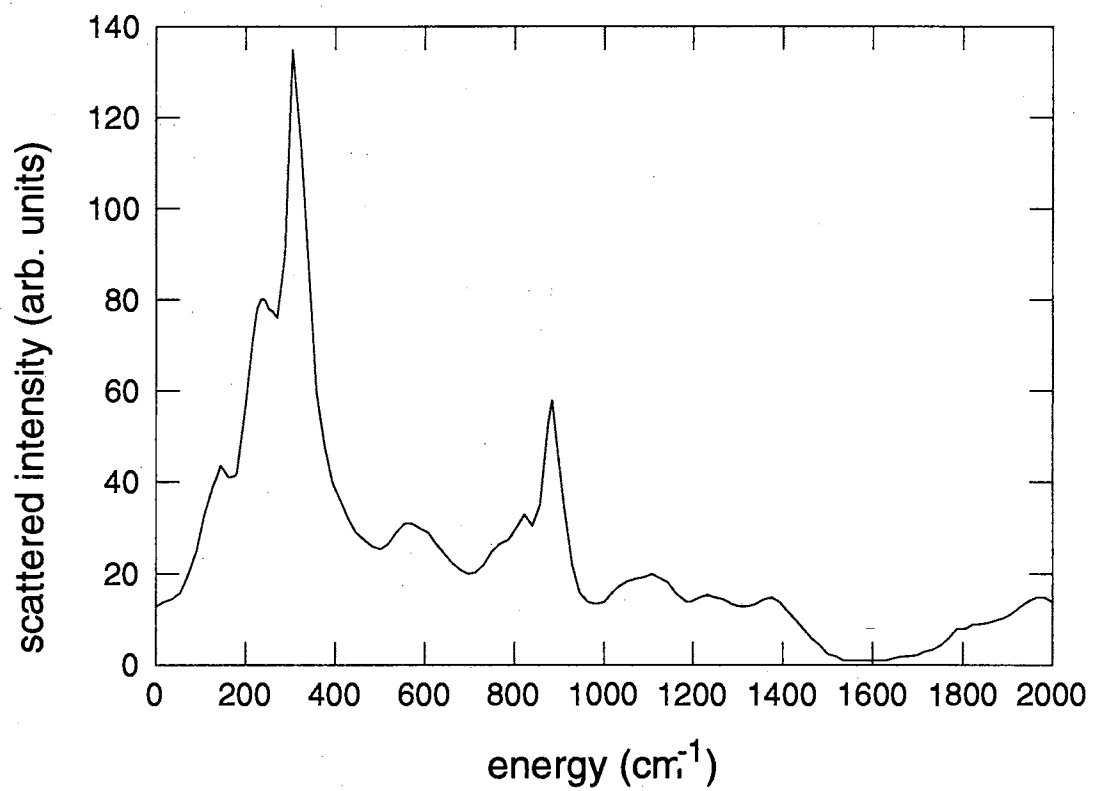


Figure 16. Raman spectra of 2wt.% NdF₃:CaF₂-YF₃ at 300K.

from this Stark level to the lowest one of the ${}^4G_{5/2}$ state, which corresponds to a phonon energy of $\sim 70 \text{ cm}^{-1}$.

Further increase of excitation photon energy to $\lambda_p = 571.5 \text{ nm}$ leads to a practically monotonic increase of Γ_h , which is similar to that reported for the glasses in the previous section and is limited by the time resolution of our method ($\sim 0.8 \text{ ps}$). This very fast relaxation can be explained by a spontaneous single phonon transition from high lying Stark levels within the ${}^4G_{5/2}, {}^2G_{7/2}$ manifold. In this case the increasing energy gap between the lowest Stark level and the higher levels being excited, incorporates phonons of higher frequencies (ω_{ph}) into the relaxation process. As shown in Fig. 17 this gives rise to a relaxation rate $1/T_2 \sim \omega_{ph}^3$.

Due to the large energy gap between the two lowest Stark levels of ${}^4I_{9/2}$ ($\Delta E \geq 83 \text{ cm}^{-1}$) and ${}^4G_{5/2}$ ($\Delta E \geq 69 \text{ cm}^{-1}$) phase relaxation processes at $T = 9 \text{ K}$ due to phonon absorption cannot account for the change in Γ_h .

We measured the temperature dependence of Γ_h from 9K to 100K while exciting the lowest Stark level of ${}^4G_{5/2}, {}^2G_{7/2}$ for both the I ($\lambda = 579\text{nm}$) and II ($\lambda = 580.5\text{nm}$) centers. As shown in Figs. 15(a) and 15(c) there is an abrupt decrease of T_2 for the I center as the temperature was increased from 9 to 65K.

The measured APE decay time for the first and second exponents of the decay curve did not change significantly as we increased the temperature from 9 to 15 K. This allowed us to analyze the Γ_h temperature dependence as $\Gamma_h(T) - \Gamma_h(T = 9K)$ (Figure 18). At temperatures above 50 K, the biexponential decay curves degenerate into a single exponential and can be attributed to the homogenization of the 579 nm absorption line. The results for the I center are presented in Fig. 18.

The solid curve on Fig. 18 corresponds to a fit of the experimental data to a relaxation process by direct single phonon absorption; $\Gamma_h \sim 167/(e^{\Delta E/kT} - 1)$. Here $\Delta E = 75\text{cm}^{-1}$ is a fixed parameter corresponding to an average of the splitting between the lowest Stark levels in the ground ${}^4I_{9/2}$ ($\Delta E = 83\text{cm}^{-1}$) and ${}^4G_{5/2}, {}^2G_{7/2}$ ($\Delta E = 69\text{cm}^{-1}$) excited states. Uncertainty in the value of ΔE due

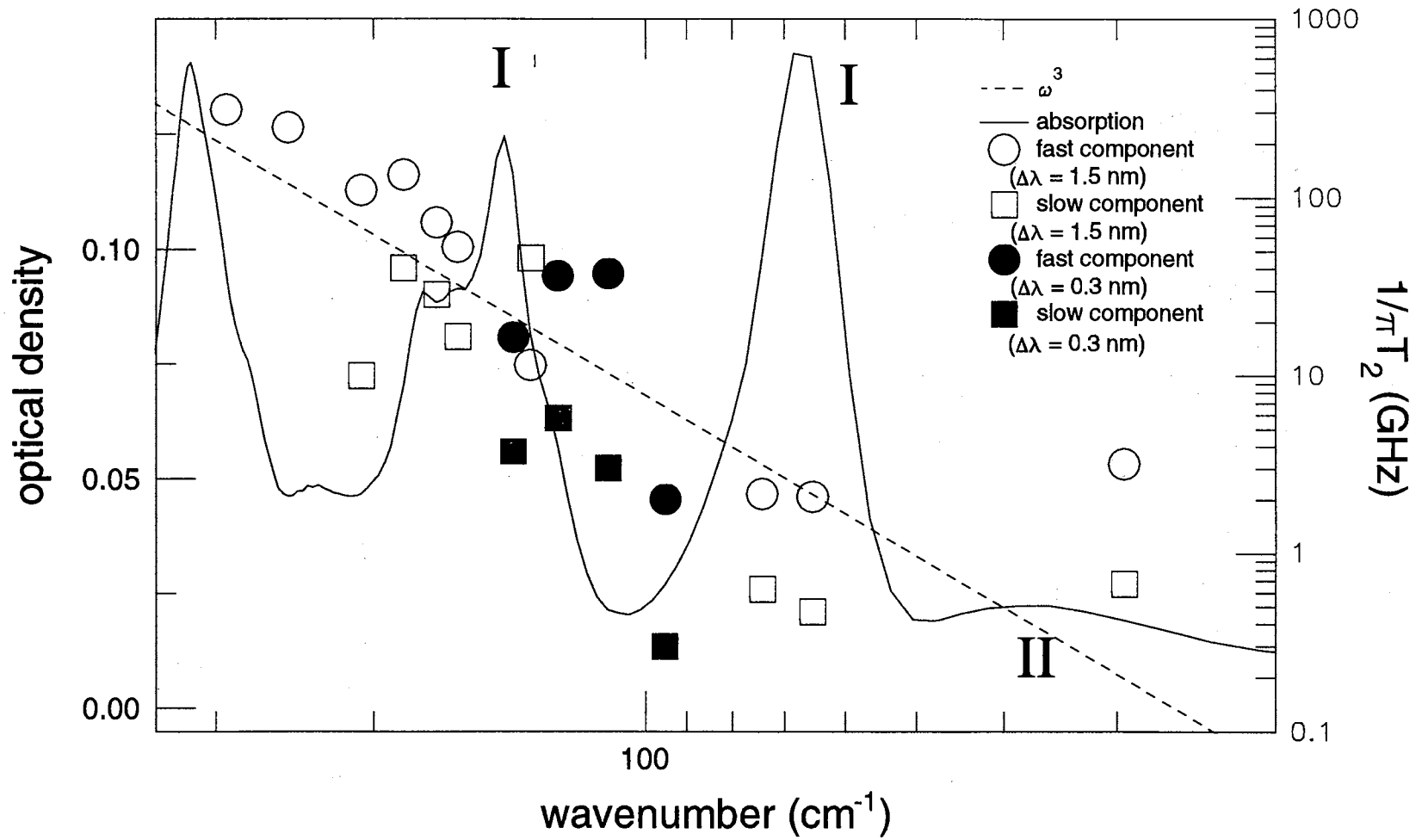


Figure 17. Absorption spectrum (left axis) and energy dependence of the dephasing rate (right axis) in 4wt.% NdF₃ : CaF₂ - YF₃ at 9K.

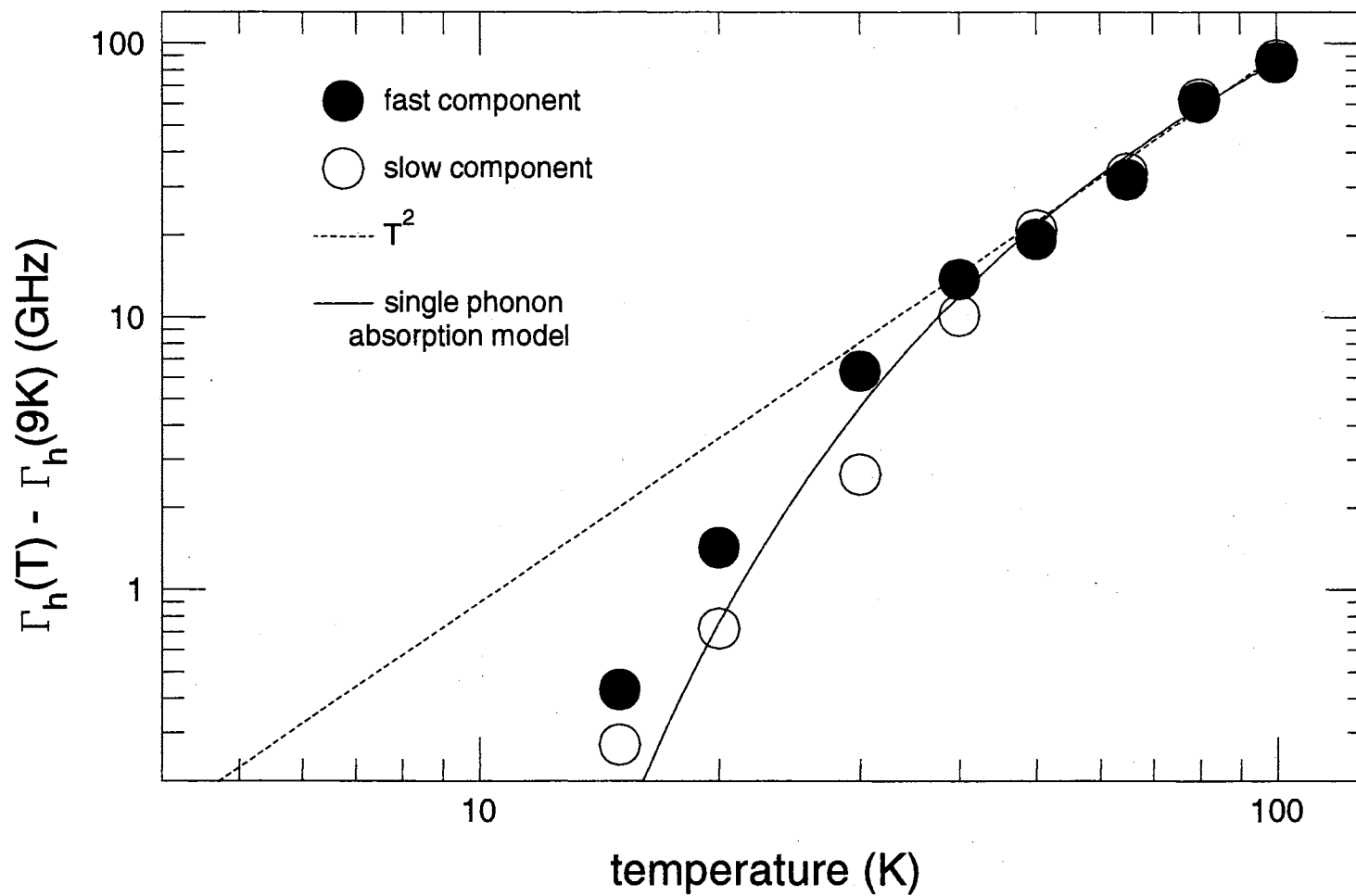


Figure 18. Temperature dependence of the total dephasing rates of the I center (579.0 nm) in $\text{CaF}_2 - \text{YF}_3(12\text{wt.}\%) : \text{NdF}_3(4\text{wt.}\%)$. The circles represent the echo decay components.

to inhomogeneous broadening of the transition ($\Gamma_{inh} = 13.5 \text{ cm}^{-1}$) results in only a small shift of the line fitted to the data in Fig. 18.

Above a temperature of 30K the experimental data of $\Gamma_h(T)$ can also be fit to a T^2 law (dashed line in Fig. 18). As mentioned earlier in this chapter, Raman scattering of acoustic phonons by Nd ions could give a quadratic temperature dependence for temperatures as low as 60K. However, in our case it is possible to explain the homogeneous line broadening throughout the 9-100K temperature range using only the model of direct single phonon relaxation between real electronic states without the use of a second order process like Raman scattering.

Analysis of the temperature dependence for the II center was more complicated and was not modeled. As the temperature was raised, upper Stark levels of the $^4I_{9/2}$ ground state of the I center became populated and led to absorption superimposed on to the 580 nm line of the II center. As shown in Fig. 19, this was particularly apparent at temperatures above 77K as the integrated absorption intensity of the 580 nm line increased much more than that of the 579 nm line.

Some discussion is warranted on the many causes of non single-exponential decay and our attempts to minimize these. Some of these causes have been discussed in Chapter 3. One additional source of nonexponential APE signals is that due to the optical density effect. It has been shown [29] that in materials that are optically dense and which possess inhomogeneous linewidths narrower than the laser bandwidth, the laser field correlation function changes as it traverses the medium. This results in the laser pulse shape changing as it goes through the material. Optical impurities located at different sample depths experience different excitation pulse shapes, and consequently the ensemble emits a nonexponential APE signal.

Our sample was purposefully chosen to have a low optical density to minimize distortions due to the optical density effect. We note that the APE decay was non-single exponential for the II center excitation ($\lambda_p=581.2\text{nm}$) which has a significantly lower optical density than the I center. (Figure 14). When we changed the Nd^{3+} concentration from 4% to 0.1%, there was no appreciable change in T_2 .

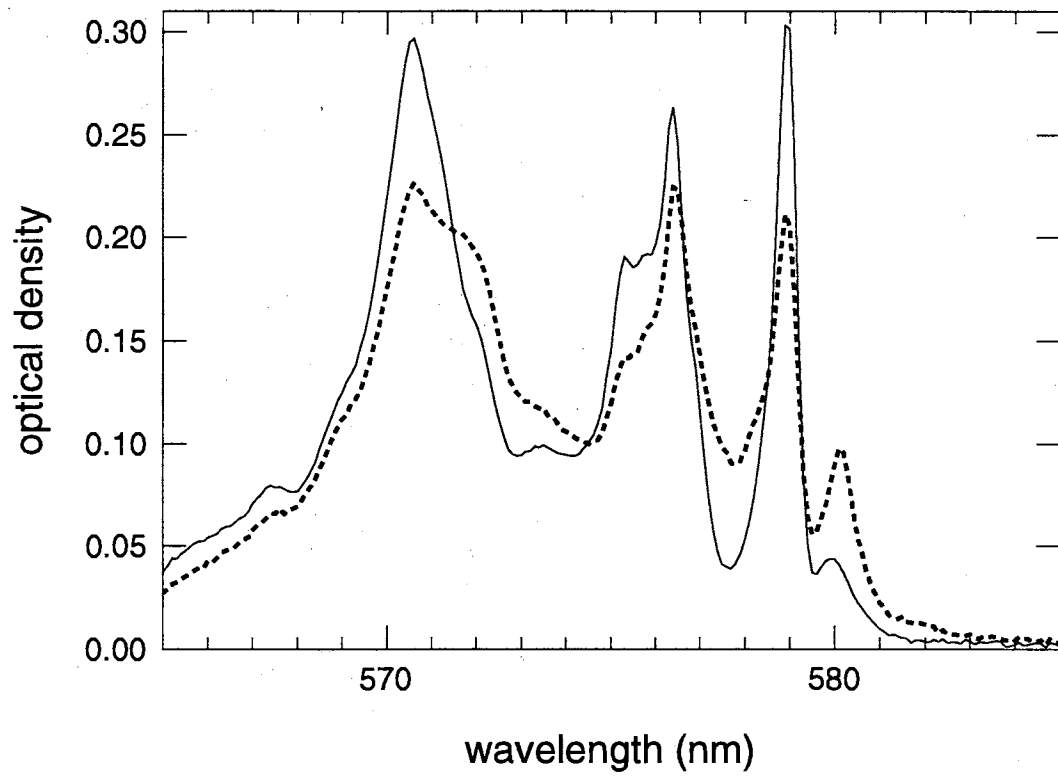


Figure 19. Absorption spectra of CaF₂ - YF₃(12wt.%) : NdF₃(4wt.%) at 9K (solid line) and 77K (dashed line).

This would imply that Nd^{3+} - Nd^{3+} interaction does not contribute to the dephasing process in this frequency and time scale range. This would also imply that spectral diffusion does not significantly affect the ground state frequency grating, as mentioned in Chapter 3.

With broadband excitation ($\Delta\lambda_p(FWHM) \approx 1.5\text{nm}$) at $\lambda_p = 578.7\text{nm}$ the long wavelength wing of the laser excitation spectrum has some overlap with the II center ($\lambda = 580\text{nm}$) and the short wavelength wing overlaps the second Stark level of the I center ($\lambda_m = 576.4\text{nm}$). Since each of the I and II centers corresponds to a spectral packet of homogeneous lines, there are site to site variations in $1/\pi T_2$ due to the inhomogeneously broadened manifold that could increase APE signal distortion. However, when we decreased $\Delta\lambda_p(FWHM)$ from 1.5 to 0.3nm and therefore significantly improved our selectivity of excited centers, neither the APE decay time nor the nonexponential character of the decay changed.

Results for ordered crystal

Figure 20 shows the absorption spectrum of a 0.3% Nd^{3+} : CaF_2 crystal. The N and M label lines belonging to Nd^{3+} ions located in a crystalline field of rhombic (C_s) symmetry. The M site is modeled as a pair of Nd^{3+} ions associated with two interstitial F^- ions.[30][31] The N site is modeled as a cluster consisting of four Nd^{3+} ions and four interstitial F^- ions.[32] The splitting of the N and M sites is caused by Nd^{3+} pair splitting in the ${}^4G_{5/2}$ excited state. These splittings were barely resolved in the absorption spectrum, which was measured with a halogen lamp light source and a 2-meter spectrometer with a resolution of about 2cm^{-1} .

The optical linewidths were much narrower in the CaF_2 crystal than in the disordered crystal, requiring greater frequency selectivity of the laser source. An etalon from a Spectra Physics 375 dye laser was glued to a Newport mirror mount and the assembly placed within the model 3500 dye laser cavity. The etalon combined with the single plate birefringent tuner already in the cavity resulted in a decrease of laser bandwidth from 1.5nm to about 0.1nm, with a corresponding increase of pulse duration to 14ps FWHM. The etalon had a free spectral range

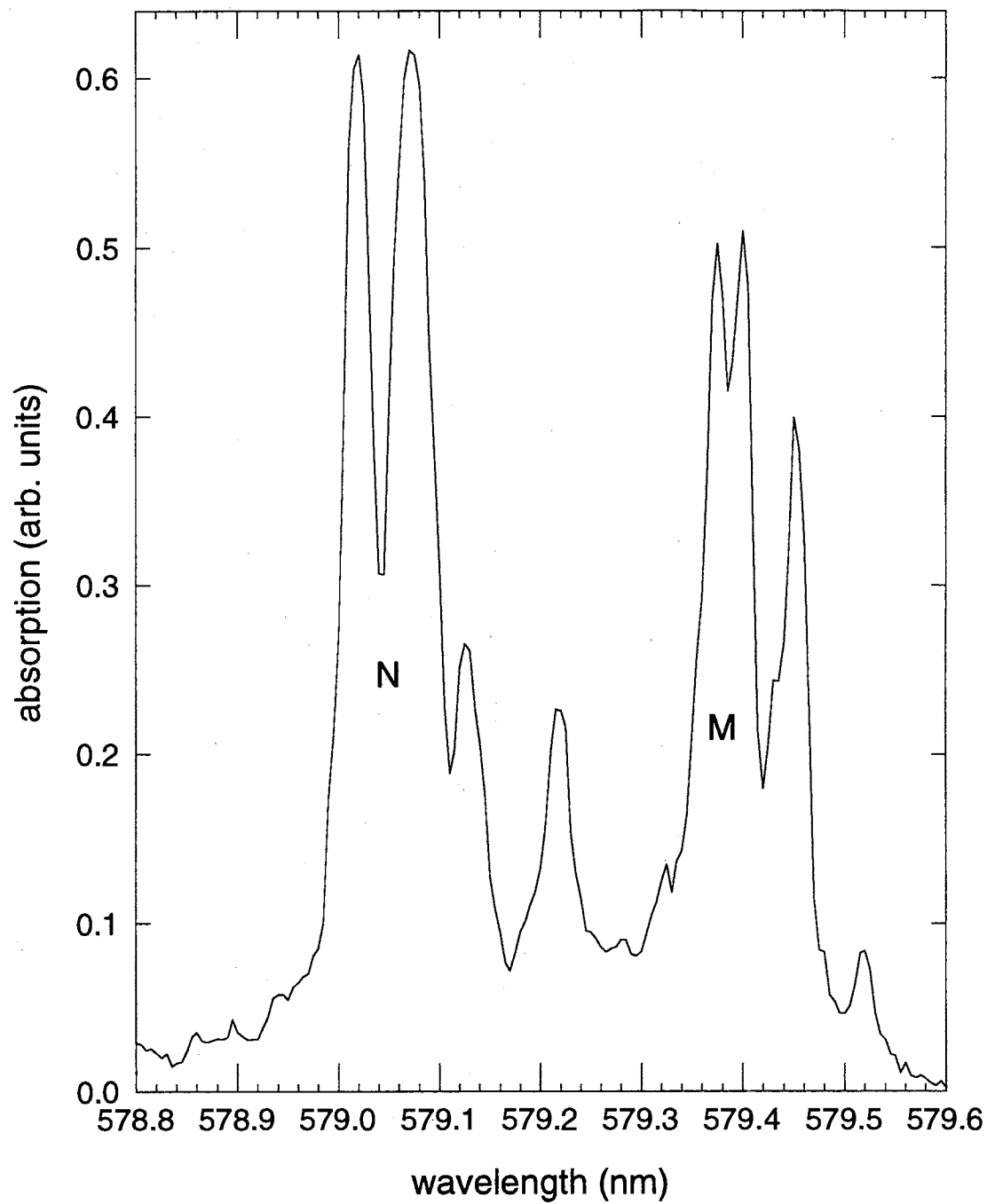


Figure 20. Absorption spectrum of 0.3wt.% Nd₂O₃:CaF₂ at 9K. M and N label two different crystal field sites.

(FSR) of ~ 900 GHz corresponding to an effective fine tuning range of about 1nm. The wavelength was determined by using a Burleigh wavemeter and a 0.25 meter Spex monochrometer. Given the finesse of the tuning apparatus and uncertainty in the wavelength measuring devices, the uncertainty in the true wavelength is estimated to be ± 0.4 nm. This experimental error combined with a relatively broad laser spectral bandwidth compared to the narrow linewidth of the M and N centers prevented careful measurement of the wavelength dependence of $1/\pi T_2$.

The APE signals were oscillatory in nature, as shown in Fig. 21 and were nonexponential at low temperatures.

The APE signal had two exponential decay components of 230ps and 2000ps for the N center, and a single component of approximately 1800 ps for the M center. To make measurements over such a large time base, the optical delay line was reconfigured for a double-pass geometry allowing a maximum scan range of -340ps to +3400ps. However, a long APE signal decay combined with long period oscillations made multiexponential APE signal deconvolution impractical in all but a few cases. The reported values of $T_2 = 0.46$ ns- 4 ns for the N center and $T_2 = 3.6$ ns for the M center were arrived at by tuning the laser frequency across each peak and averaging the measured value of T_2 .

The relatively broad frequency spectrum of the dye laser seems to preclude measurement of sub cm^{-1} spectral details. This is not necessarily true. In pure crystals, such as CaF_2 , the optical transitions have sufficiently narrow linewidth to insure that the laser source interacts coherently with the entire ensemble of ions. Under this near-resonance condition, two (or more) ensembles possessing optical transitions that differ only slightly in energy may be driven coherently. The APE emitted from each ensemble interferes with that produced by the other, resulting in an oscillatory APE signal measured at the detector. The frequency components of the detected APE signal correspond to the difference in transition frequency of the two (or more) ensembles of dopant ions.

Figure 22 and Table XV shows the result of Fourier transform analysis of 0.3% Nd: CaF_2 APE signals.

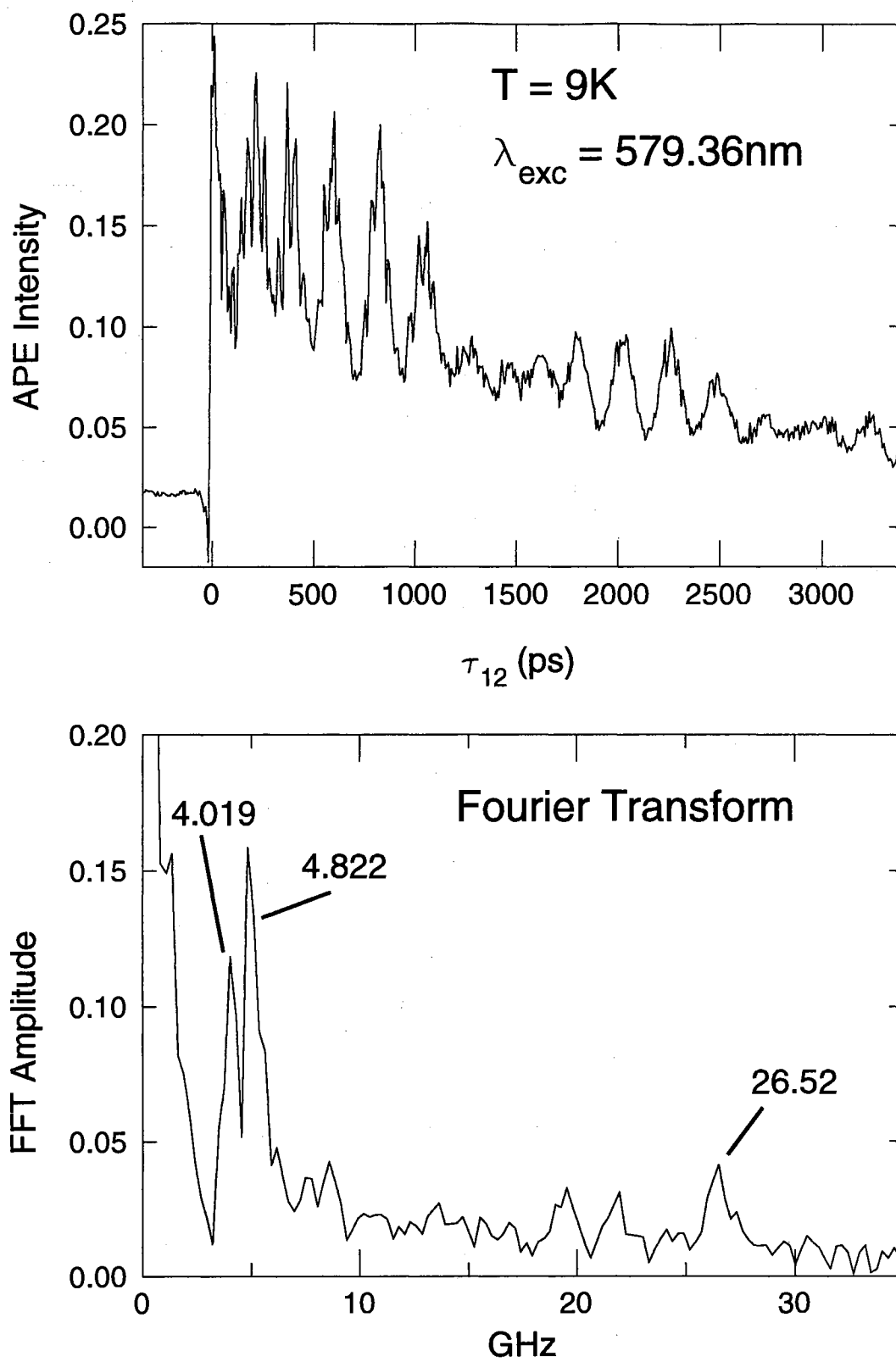


Figure 21. (a) APE signal of 0.3% $\text{Nd}^{3+}:\text{CaF}_2$ at 9K, $\lambda_{\text{exc}} = 579.36\text{ nm}$. (b) Fourier transform of the APE signal. Principle peaks are labeled by frequency.

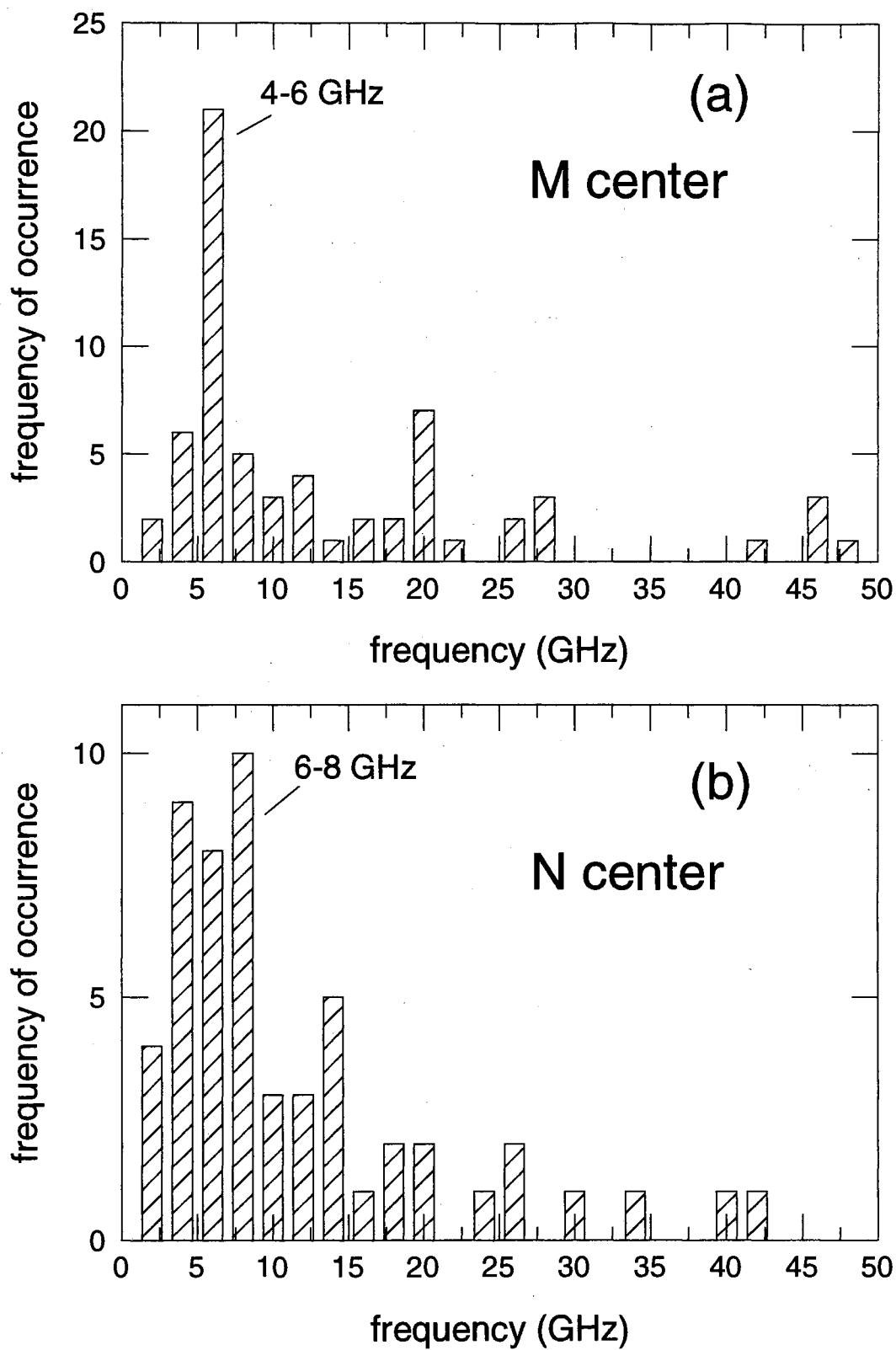


Figure 22. Fourier analysis of 23 APE signals in 0.3% Nd³⁺ : CaF₂ at 9K measured at wavelengths corresponding to both M and N centers. Each "bin" of the histogram represents an interval of 2 GHz.

The fast Fourier transform (FFT) of twenty-three APE signals recorded across the M and N centers were computed, an example of which is shown in Fig. 21(b). These were analyzed in terms of how many APE signals had frequency components within a specific interval. The APE signals were separated into two groups depending on whether their excitation wavelength corresponded to the N or M center. Each FFT frequency spectrum had many distinct peaks, but those peaks varied considerably in intensity depending on the signal to noise ratio of the APE signal and the excitation frequency.

Figure 22(a) shows that the M center had two primary frequency components at 4-6GHz ($0.13\text{cm}^{-1} - 0.20\text{cm}^{-1}$) and another at 20 GHz ($\sim 0.67\text{cm}^{-1}$). The N center had components at 6-8GHz ($0.20\text{cm}^{-1} - 0.27\text{cm}^{-1}$) and another at 14GHz (0.50cm^{-1}). The 20GHz splitting of the M center is assigned to Nd^{3+} pair splitting of the ${}^4G_{5/2}$ state, by comparison with the barely resolvable 0.7cm^{-1} splitting of the M center shown in Fig. 20. The FFT analysis also indicates a frequency component corresponding to an energy separation of $0.20\text{cm}^{-1} - 0.27\text{cm}^{-1}$, but it is unclear whether this splitting is in the excited state or ground state multiplet. Recent measurements of ${}^4I_{9/2}$ and ${}^4G_{5/2}, {}^2G_{7/2}$ Stark level splitting in CaF_2 [33] had a resolution of $\pm 1\text{cm}^{-1}$, which is greater than the level splittings reported by our experiments.

The cluster nature of the N center is reflected in Fig 22(b) by the lack of any single dominant frequency component, unlike the M center. Again, there is a distribution centered at 7GHz, but its width is greater than for the M center, reflecting the greater distribution of splittings due to the Nd^{3+} cluster. Neither the 7GHz nor the 14GHz frequency component corresponds to any structure of the N center shown in Fig 20. It is possible that the 14 GHz splitting may be the first harmonic of the strong 7 GHz component. However, the data do suggest a principle splitting of about 0.25cm^{-1} either in the excited state or ground state of the ${}^4I_{9/2} \rightarrow {}^4G_{5/2}$ transitions for both the N and the M center.

Temperature dependence measurements were made at two wavelengths 579.09 nm and 579.45 nm corresponding to the N and M centers, respectively. At temperatures above 22K, the APE signal was single exponential and did not exhibit the oscillations seen at T=9K. At temperatures above 40K, the signal decay time had decreased to times comparable to the laser pulsewidth. These data are shown in Table XIII, Table XIV, and in Fig. 23.

The long decay components were used in the plots of Fig. 23. The data were fit to a single phonon absorption model, Eqn. 19, with one adjustable parameter. Reference [33] measured the level splitting between the two lowest Stark levels in the ground and excited state of CaF₂ to be 35 and 61 cm⁻¹ (M center) and 41 and 57 cm⁻¹ (N center). Consequently, we have taken the average of these two values for each center as the energy splitting used in the fitting process: 48 cm⁻¹ (M center) and 49 cm⁻¹ (N center). The low temperature intercepts from the fits were 0.07 GHz (N center) and 0.008 GHz (M center). It can be seen From Fig. 23 that the data are consistent with a direct exponentially activated nonradiative process with inter Stark level single phonon absorption in the ground and excited ⁴G_{5/2}, ²G_{7/2} multiplets of Nd³⁺ ions.

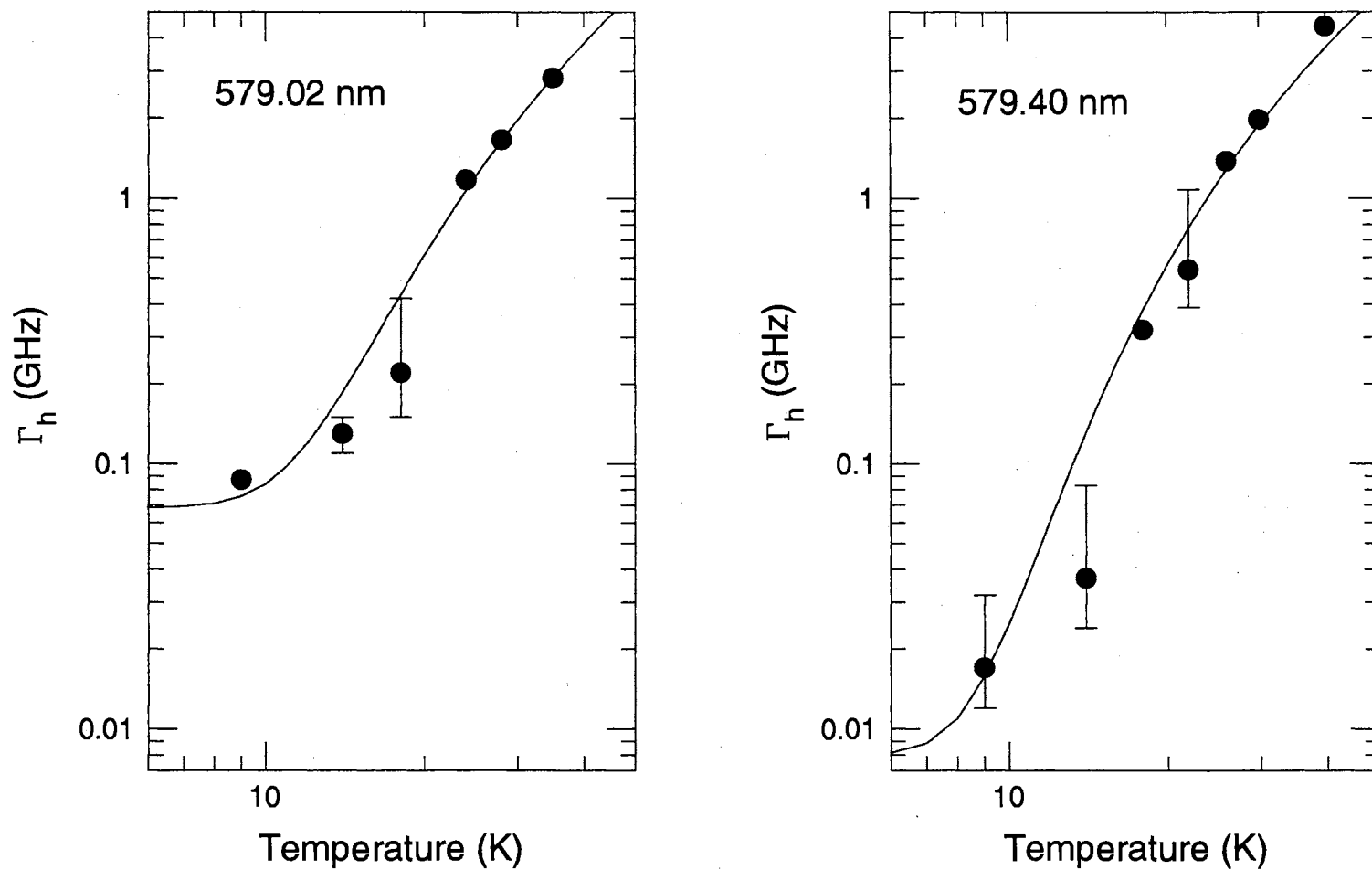


Figure 23. Temperature dependence of the dephasing rate for 0.3% $\text{Nd}^{3+} : \text{CaF}_2$ N center (left) and M center (right). The fit is to a direct, single phonon absorption process.

CHAPTER V

CONCLUSION

The information reported in this thesis regarding the use of accumulated photon echoes to directly measure optical dephasing times of the ${}^4I_{9/2} \rightarrow {}^4G_{5/2}, {}^2G_{7/2}$ transition of neodymium doped materials has led to a better understanding of dephasing dynamics in glasses, disordered crystals, and ordered crystals. Samples studied were: ED2 silicate glass, lithium germanate glass, lithium phosphate glass, calcium fluoride disordered crystal, and calcium fluoride crystal. The temperature dependence of the dephasing rate was measured in these materials, enabling specific dephasing mechanisms to be identified. In the calcium fluoride crystal, neodymium pair interactions caused narrow splittings in the energy level structure, which were resolved by Fourier analysis of oscillatory APE signals. In the glasses and disordered crystal, measurement of the dephasing rate as a function of excitation energy resulted in the identification of a low temperature dephasing mechanism for these materials.

Summary of Results

Results of dephasing time measurements using the APE were presented in Chapter 3. Three oxide glasses, all containing lithium modifier cations, and network formers of silicon, germanium, and phosphorus were the first samples studied. The temperature dependence of the dephasing time for the lowest ${}^4G_{5/2}, {}^2G_{7/2}$ Stark level was approximately quadratic. Values for specific glasses were: $T^{2.4 \pm 0.2}$ (silicate), $T^{2.4 \pm 0.1}$ (germanate), $T^{1.8 \pm 0.1}$ (phosphate). These results are consistent with the prediction of models based on Raman scattering of phonons with a Debye density of states modified to account for dilational symmetry of glasses (fracton

model) or a modified Debye temperature reflecting a different energy coefficient for acoustic versus optical phonons. Low temperature (9K) excitation energy ($\hbar\omega$) dependence of the dephasing rate showed that the dephasing rate increased as $(\hbar\omega)^3$ in the germanate and phosphate glasses, which is consistent with excited state relaxation via direct single phonon emission. The dephasing rate in the silicate glass varied approximately linearly with energy, which may be a consequence of increased inhomogeneous broadening in the silicate glass compared to that in the phosphate and germanate glasses. The lifetime limited T_2 dephasing times in the three glasses was 11 ps (25ps long component), 27.8ps, and 14.7ps for the silicate, germanate, and phosphate glass, respectively. The value of T_2 decreased to ~ 1.5 ps as the excitation wavelength was reduced to approximately the same value of the third Stark component.

The same measurements were made on a yttrium fluoride disordered crystal which had an inhomogeneous linewidth approximately 5% that of the glasses, suggesting a less disordered host matrix. The dephasing rate temperature dependence for the lowest Stark level of the I center was consistent with a direct single phonon absorption process with a phonon energy of 75cm^{-1} and became quadratic with T at temperatures above 50K. Like the glass, the dephasing rate increased as the cube of the excitation energy, which is consistent with direct single phonon emission at low temperature. The lifetime limited dephasing time at 9K was 212ps (800ps long component) which quickly decreased to 1.5 ps at wavelengths that represented higher Stark levels within the multiplet. These values of T_2 were ten times those measured in the glasses.

The inhomogeneous linewidth of the calcium fluoride crystal was approximately 5% that of the disordered crystal, and dephasing measurements were made on the lowest Stark components of two optical centers denoted M and N. Dephasing times in the crystal were ten to twenty times longer than those measured for the disordered crystal. Data from temperature dependence measurements of the dephasing rate for the M and N centers were consistent with a single phonon absorption mechanism in the ground and excited states. Complex oscillations in

the APE signal indicated quantum beating between Nd^{3+} pair and cluster levels. Fourier analysis of the oscillations revealed two primary frequencies of 4-6 GHz and 20 GHz for the M center, corresponding to level splittings of about 0.18 cm^{-1} and 0.67 cm^{-1} . The N center had a broader distribution of frequencies, characteristic of the complicated energy level structure associated with a cluster. The N center frequency distribution peaks indicated principle level splittings of about 0.25 cm^{-1} and 0.50 cm^{-1} .

Progression from the calcium fluoride crystal to the oxide glasses represented a corresponding decrease in long range order of the host lattice. Introduction of YF_3 into the CaF_2 host resulted in the appearance of new types of rhombic NdY and F centers. The large (12%) concentration of YF_3 has been shown to lead to a disordering of the crystalline structure, appearance of two groups of optical centers, and large inhomogeneous broadening.[34] The glass hosts possess only short range order, and the broad overlapping Stark levels suggest a near continuum of inhomogeneously broadened optical centers.

Suggestions for Future Work

Additional work should be done on the applicability of the APE method to excited state Stark multiplets. One assumption used in the derivation of Eqn. 117 is that there be no population relaxation during the inter-pulse interval (t_{12}). This simplification was necessary to apply a two-level model to the system during t_{12} . It is known, however, that inter-Stark population relaxation can occur on time scales of a few picoseconds, which violates this assumption. To accurately consider excited state population relaxation, one would have to use a density matrix formalism for a three-level system interacting with a pulsed laser field, and solve the equations numerically.

Useful information would be gained by applying the APE method to measure dephasing times of transition metal ions that are strongly coupled to the crystal field. Transition metal ions such as chromium or titanium, which have unshielded 3d electrons, couple strongly to the lattice and therefore may be a better probe

of how changes in the host modify lattice dynamics. APE's have been successfully applied to measurement of the 4A_2 zero field splitting of Cr^{3+} in ruby and alexandrite. [35][36][37] Use of the APE to measure dephasing in the 4T_2 level of Cr^{3+} would first require that the question regarding population relaxation during excitation be answered.

Lastly, to check the hypothesis that the nonexponential nature of the APE signal is primarily due to overlapping Stark levels, and not necessarily caused by a continuum of optical centers, it would be useful to measure the APE of the ${}^7F_0 \rightarrow {}^5D_0$ transition in Eu^{3+} doped glass, and compare the results with those obtained by FLN.[21][20] Exciting this singlet transition would provide a check about how continuous variation in optical centers affects the shape of the APE signal by eliminating the effect of overlapping Stark levels.

BIBLIOGRAPHY

1. A. Kiel in *Paramagnetic Resonance*, edited by W. Low (Academic, New York, 1963) p. 525.
2. M.J. Weber, "Multiphonon relaxation of rare-earth ions in Yttrium Orthoaluminate", *Phys. Rev. B* 8, 54-64 (1973).
3. "Multiphonon relaxation of rare-earth ions in oxide glasses", C.B. Layne, W.H. Lowdermilk, M.J. Weber, *Phys.Rev. B* 16, 10 (1977).
4. "Geometrical representation of the Schrodinger equation for solving maser problems", R.P. Feynman, F.L. Vernon, R.W. Hellwarth, *J. Appl. Phys.* 28, 49-52 (1957).
5. E.L. Hahn, *Phys. Rev.* 80, 580 (1950).
6. W.H. Hesselink, D.A. Wiersma, " Photon echoes stimulated from an accumulated grating: theory of generation and detection", *Phys. Rev. Lett.* 43, 1991 (1979).
7. I.D. Abella, N.A. Kurnit, S.R. Hartmann, "Photon Echoes," *Phys. Rev.* 141, 391-141 (1966).
8. L. Allen, J.H. Eberly, *Optical Resonance and Two-Level Atoms*, (Dover, New York, 1987).
9. Marc D. Levenson, Satoru S. Kano, *Introduction to Nonlinear Laser Spectroscopy*, (Academic Press, San Diego, 1988).
10. Anthony E. Siegman, *Lasers*, (University Science Books, Mill Valley, CA 1986).
11. Harmen de Vries, Douwe A. Wiersma, "Numerical simulations of accumulated stimulated photon echoes," *J. Chem. Phys.* 80, 657-666 (1984).
12. Harmen de Vries, "The application of accumulated stimulated photon echoes as studied by numerical simulations," Dept. of Physical Chemistry, State University, Nijenborgh 16, 9747 AG Groningen, The Netherlands, 1982/'83.
13. Baldassare DiBartolo, *Optical Interactions in Solids*, (John Wiley & Sons, New York, 6th edition, 1986).

14. R.M. Macfarlane, R.M. Shelby, "Homogeneous line broadening of optical transitions of ions and molecules in glasses", *J. Lumin.* **36**, 179 (1987).
15. O.L. Anderson, "The Debye temperature of vitreous silica", *J. Phys. Chem. Sol.* **12**, 41-52 (1959).
16. S.K. Lyo, "Anomalous optical homogeneous linewidths in glasses", *Phys. Rev. Lett.* **48**, 688-691 (1982).
17. M.M. Broer, B. Golding, W.H. Haemmerle, J.R. Simpson, D.L. Huber, "Low temperature optical dephasing of rare-earth ions in inorganic glasses", *Phys. Rev. B* **33**, 4160-4165 (1986).
18. I.S. Osad'ko, S.A. Zhdanov, "Effect of low-frequency modes on temperature broadening of optical lines of impurity centres in glasses", *Opt. Commun.* **42**, 185-188 (1982).
19. S. Alexander, R. Orbach, *J. Phys. (Paris)* **43**, L625 (1982).
20. F. Durville, G.S. Dixon, R.C. Powell, "Comparison of the spectral and temperature dependences of the homogeneous linewidths in Eu^{3+} - doped fluoride and oxide glasses", *J. Lumin.* **36**, 221-229 (1987).
21. G.S. Dixon, R.C. Powell, X. Gang, "Fracton contribution to the temperature dependence of the homogeneous linewidth of the ${}^5D_0 - {}^7F_0$ transition in Eu^{3+} - doped glasses", *Phys. Rev. B* **33**, 2713-2718 (1986).
22. D.L. Huber, "Reassessment of the Raman mechanism for homogeneous linewidths in glasses", *J. Non Cryst. Sol.* **51**, 241 (1982).
23. D.L. Huber, "Raman contribution to the homogeneous optical linewidth of impurity ions in vitreous silica", *J. Lumin.* **36**, 327-329 (1987).
24. D. Heiman, R.W. Hellwarth, D.S. Hamilton, "Raman scattering and non-linear refractive index measurements of optical glasses", *J. Non. Cryst. Sol.* **34**, 63-79 (1979).
25. R.M. Shelby, "Measurement of optical homogeneous linewidths in a glass with picosecond accumulated photon echoes", *Opt. Lett.* **8**, 88 (1983).
26. O.K. Alimov, T.T. Basiev, Y.K. Voron'ko, Y.V. Gribkov, A.Y. Karasik, V.V. Osiko, A.M. Prokhorov, I.A. Scherbakov, "Selective laser excitation study of the structure of inhomogeneously broadened spectra of Nd^{3+} ions in glass.", *Sov. Phys. JETP* **47**, 29 (1978).
27. H.W.H. Lee, "Intra-stark relaxation of Nd^{3+} in silicate glass: subpicosecond accumulated photon echo experiments," *J. Lumin.* **45**, 99-101 (1990).

28. T.T. Basiev, Y.K. Voron'ko, A.Y. Karasik, V.V. Osiko, I.A. Scherbakov, "Spectral migration of electronic excitation between Nd^{3+} ions in $\text{CaF}_2\text{-YF}_3$ crystals under selective laser excitation conditions", *Sov. Phys. JETP* 48, 32-36 (1978).
29. S. Saikan, H. Miyamoto, Y. Tosaki, A. Fujiwara, "Optical-density effect in heterodyne-detected accumulated photon echo", *Phys. Rev. B* 36, 5074-5077 (1987).
30. V.V. Osiko, *Sov. Phys. Sol. State.* 7, 1047 (1965).
31. Yu.K.Voronko, A.A.Kaminski, V.V.Osiko, "Analysis of the optical spectrum of $\text{CaF}_2\text{:Nd}^{3+}$ (type 1) crystals", *Sov.Phys. JETP* v.22, 295-300 (1966).
32. V.V. Osiko, I.A. Shcherbakov, *Sov. Phys. Sol. State* 13, 820 (1971).
33. T.P.J. Han, G.D. Jones, R.W.G. Syme, "Site-selective spectroscopy of Nd^{3+} centers in $\text{CaF}_2\text{:Nd}^{3+}$ and $\text{SrF}_2\text{:Nd}^{3+}$ ", *Phys. Rev. B*, (1993).
34. Kh.S.Bagdasarov, Yu.K.Voronko, A.A.Kaminski, L.V.Krotova, V.V.Osiko, *Phys. Stat. Sol.*, v.12 (1965) 905.
35. M.H.F. Overwijk, C.R. de Kok, J.I. Dijkhuis, H.W. de Wijn, "Accumulated photon echo in Cr^{3+} -doped crystals", *J. Lumin.* 45, 440-441 (1990).
36. M.H.F. Overwijk, J.I. Dijkhuis, H.W. de Wijn, R. Vreeker, R. Sprik, A. Lagendijk, "Accumulated photon echo in ruby under hydrostatic pressure: ground-state splitting and spontaneous decay of $2\bar{A}(^2E)$ ", *Phys. Rev. B* 43, 12744-12750 (1991).
37. M.H.F. Overwijk, P.J. Rump, J.I. Dijkhuis, H.W. de Wijn, "Accumulated photon echo in ruby and alexandrite", *Phys. Rev. B* 44, 4157-4164 (1991).

APPENDIX

APPENDIX A

THE TUNED PREAMPLIFIER

The tuned preamplifier used in this experiment is of a very basic design, as shown in Fig. 25. It consists of two cascaded RC filters separated by wideband operational amplifiers that function as 20 dB gain blocks. The total amplitude gain of the preamp is 34 dB with a Q of about 50 at a center frequency of 4 MHz, as shown in Fig. 24. It is tuned by applying a 4 MHz signal to the input, and observing the output on a spectrum analyzer. The iron core of the inductor is adjusted with a wooden screwdriver until the resonance of each RC filter overlap each other, and large signal gain is seen at 4 MHz. $0.1 \mu F$ blocking capacitors reduce stray RF feedback into the gain blocks. A metal box encloses the entire circuit, which is powered by a ± 13.6 volt battery power supply.

In the APE experiment, a metal box also houses the PIN photodiode detector. The preamp BNC input is attached directly to the BNC output of the photodiode housing. A ground strap from the photodiode housing to a grounding terminal on the lock-in amplifier further reduces background noise. It was also necessary to insert a 10x attenuator on the trigger output of the signal generator to reduce unwanted 4MHz RF emission from the approximately 3-meter coax cable connected to the reference input of the lock-in.

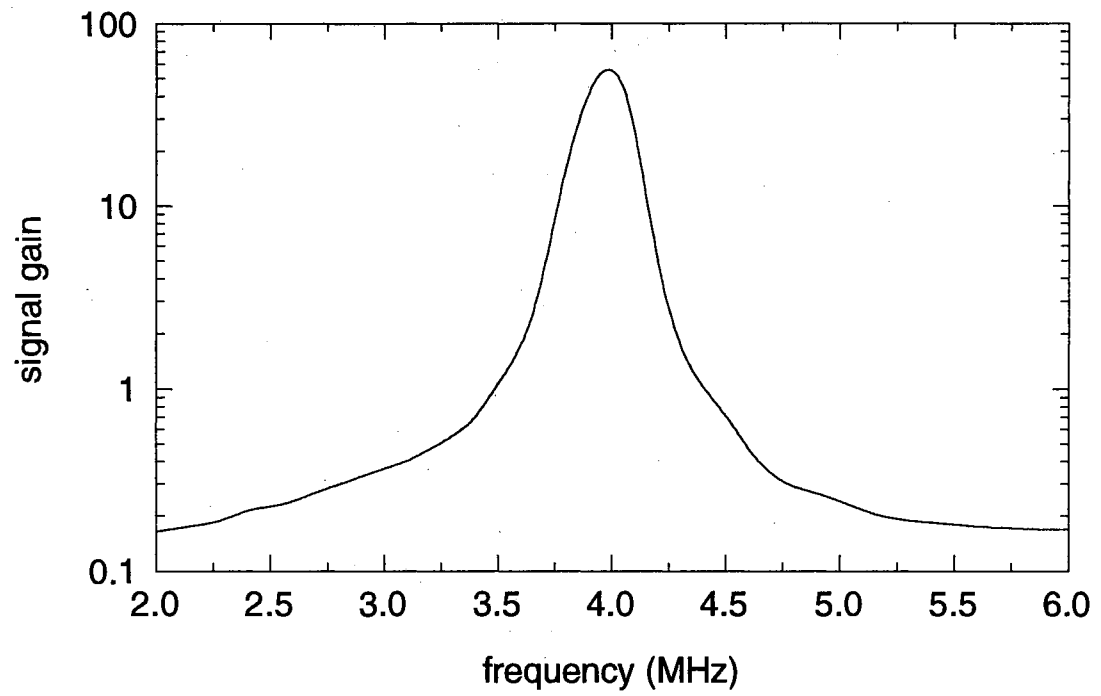
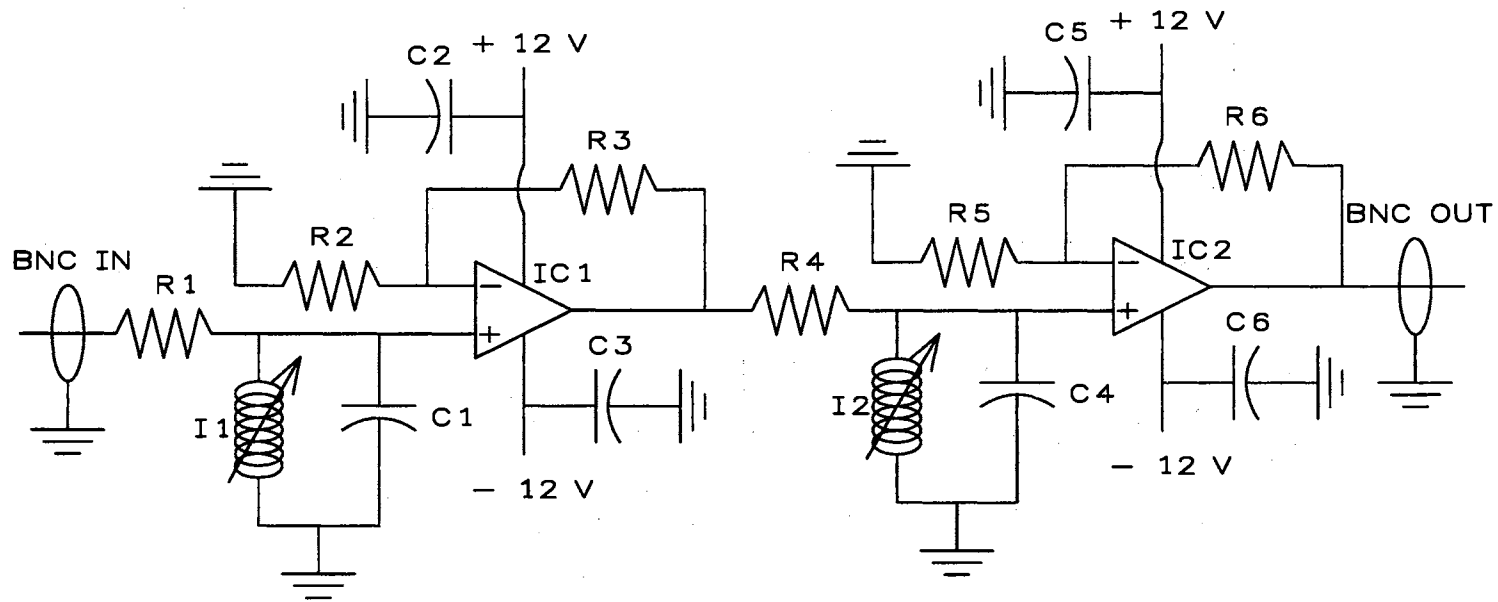


Figure 24. Frequency response of the tuned preamplifier



R 1,R 3,R 4,R 6	10,000 ohm, 1/4 watt resistor
R 2,R 5	1,000 ohm, 1/4 watt resistor
C 1,C 4	200 pF capacitor
C 2,C 3,C 5,C 6	0.1 uF capacitor
I 1,I 2	100 uH variable inductor
IC 1,IC 2	TI 2037C wideband op-amp

Figure 25. Tuned preamplifier schematic

APPENDIX B

APE SIGNAL THEORY

The excitation matrix

In this appendix, the Maxwell-Bloch equations will be solved for the two-pulse sequence shown in Fig. 26. In this figure, τ_p , t_{12} , and T represent the pulse width, inter-pulse pair separation time, and the pulse pair repetition period, respectively.

The Rabi frequency is defined to be

$$\mathbf{X}^* = \frac{-\vec{\mu}_{21} \odot \mathbf{E}}{\hbar} * e^{i(\omega t - \alpha_i)} \quad (36)$$

where

$$\alpha_i = \mathbf{k} \odot \mathbf{r} + \phi_i$$

$$\vec{\mu}_{21} = \text{dipole moment of the relevant transition}$$

$$\mathbf{E} = \text{driving field .}$$

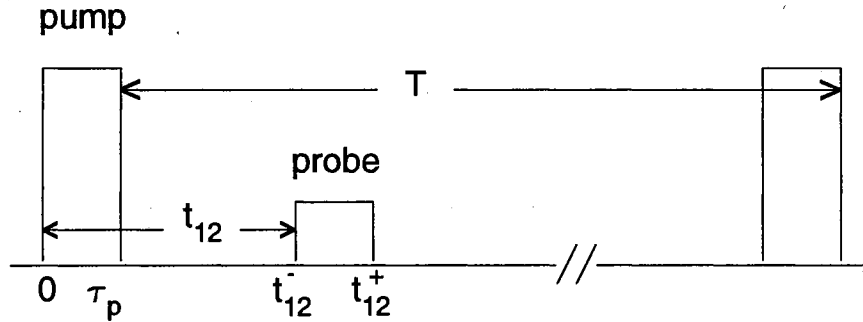


Figure 26. Pump-probe timing diagram for APE signal generation.

The pseudofield vector and the Bloch vectors in the stationary frame are, respectively:

$$\beta = \text{Re}X^*(t)\hat{\mathbf{1}} + \text{Im}X^*(t)\hat{\mathbf{2}} + \omega_o\hat{\mathbf{3}} \quad (37)$$

$$\mathbf{R} = u\hat{\mathbf{1}} + v\hat{\mathbf{2}} + w\hat{\mathbf{3}} \quad (38)$$

with the Bloch vector components given in Chapter 3 by Eqns. 5.

In a frame of reference rotating at ωt about the $\mathbf{3}$ axis, the pseudofield and Bloch vectors become:

$$\beta' = -X \cos(\alpha)\hat{\mathbf{1}}' + X \sin(\alpha)\hat{\mathbf{2}}' + \omega_o\hat{\mathbf{3}}' \quad (39)$$

$$\mathbf{R}' = u\hat{\mathbf{1}}' + v\hat{\mathbf{2}}' + w\hat{\mathbf{3}}'$$

where we have used the rotation matrix

$$\begin{bmatrix} \hat{\mathbf{1}} \\ \hat{\mathbf{2}} \\ \hat{\mathbf{3}} \end{bmatrix} = \begin{pmatrix} \cos(\omega t) & -\sin(\omega t) & 0 \\ \sin(\omega t) & \cos(\omega t) & 0 \\ 0 & 0 & 1 \end{pmatrix} \begin{bmatrix} \hat{\mathbf{1}}' \\ \hat{\mathbf{2}}' \\ \hat{\mathbf{3}}' \end{bmatrix}. \quad (40)$$

The equation of motion of the Bloch vector in the rotating frame is

$$\begin{aligned} \frac{d\mathbf{R}'}{dt} &= (\beta' - \omega') \otimes \mathbf{R}' \\ &= \boldsymbol{\Omega}' \otimes \mathbf{R}' \end{aligned} \quad (41)$$

where $\omega' = \omega\hat{\mathbf{3}}'$ and the new pseudofield vector is

$$\boldsymbol{\Omega}' = -X \cos(\alpha)\hat{\mathbf{1}}' + X \sin(\alpha)\hat{\mathbf{2}}' + \Delta\hat{\mathbf{3}}' \quad (42)$$

and the detuning frequency is

$$\Delta = \omega_o - \omega. \quad (43)$$

The task which we have before us is to solve the equations of motion for the elements of the Bloch vector (Eq. 41). This can be achieved through an explicit solution of the coupled differential equations, or through sequential coordinate rotations[8]. The latter method is chosen since it is easier to follow and more illustrative. Figure 27 shows graphically our starting point.

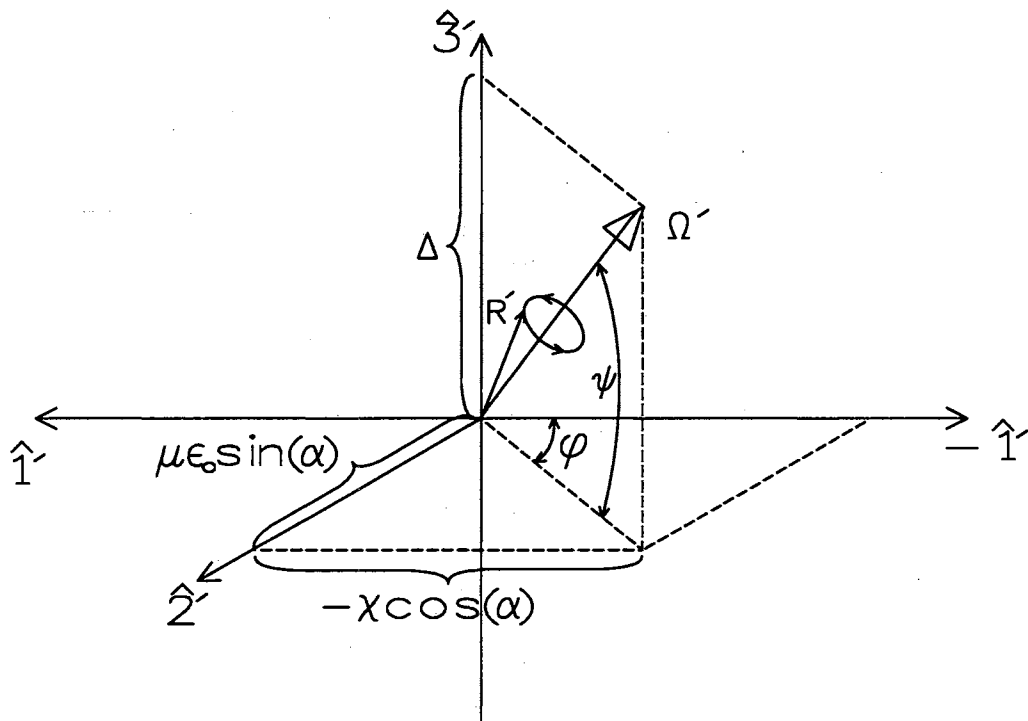


Figure 27. Coordinate representation of the Bloch vector (\mathbf{R}') precessing about the pseudofield vector (Ω').

The pseudofield vector $\boldsymbol{\Omega}'$ precesses about the $\hat{\mathbf{z}}'$ axis while the Bloch vector spins about $\boldsymbol{\Omega}'$. The strategy in solving this problem is to rotate the coordinate system until \mathbf{R}' is stationary.

First, rotate about the $\hat{\mathbf{z}}'$ axis through the angle ϕ , where it can be seen from Fig. 27 that

$$\tan(\phi) = \tan(\alpha) \quad (44)$$

and the rotation matrix is

$$\begin{bmatrix} \hat{\mathbf{1}}'' \\ \hat{\mathbf{2}}'' \\ \hat{\mathbf{3}}'' \end{bmatrix} = \begin{bmatrix} \cos(\phi) & -\sin(\phi) & 0 \\ \sin(\phi) & \cos(\phi) & 0 \\ 0 & 0 & 1 \end{bmatrix} \begin{bmatrix} \hat{\mathbf{1}}' \\ \hat{\mathbf{2}}' \\ \hat{\mathbf{3}}' \end{bmatrix}. \quad (45)$$

Next rotate by angle ψ about the $\hat{\mathbf{2}}'$ axis where

$$\tan(\psi) = \frac{\Delta}{\chi} \quad (46)$$

and the rotation matrix is

$$\begin{bmatrix} \hat{\mathbf{1}}''' \\ \hat{\mathbf{2}}''' \\ \hat{\mathbf{3}}''' \end{bmatrix} = \begin{bmatrix} \cos(\psi) & 0 & -\sin(\psi) \\ 0 & 1 & 0 \\ \sin(\psi) & 0 & \cos(\psi) \end{bmatrix} \begin{bmatrix} \hat{\mathbf{1}}'' \\ \hat{\mathbf{2}}'' \\ \hat{\mathbf{3}}'' \end{bmatrix}. \quad (47)$$

The total rotation matrix is found by multiplying Eqns. 45 and 47. Inverting the resulting matrix gives

$$\begin{bmatrix} \mathbf{u}' \\ \mathbf{v}' \\ \mathbf{w}' \end{bmatrix} = \begin{bmatrix} \cos(\psi) \cos(\phi) & \sin(\phi) & \sin(\psi) \cos(\phi) \\ -\cos(\psi) \sin(\phi) & \cos(\phi) & -\sin(\psi) \sin(\phi) \\ -\sin(\psi) & 0 & \cos(\psi) \end{bmatrix} \begin{bmatrix} \mathbf{u}''' \\ \mathbf{v}''' \\ \mathbf{w}''' \end{bmatrix}. \quad (48)$$

The Bloch vector is not precessing around the $-\hat{\mathbf{1}}'$ axis of Fig. 27 with frequency

$$\boldsymbol{\Omega}'(\Delta) = \sqrt{\Delta^2 + \chi^2} \quad (49)$$

The coordinate system is rotated through an angle of $-\Omega(\Delta)t$ about the $-\hat{\mathbf{1}}'$ axis in order to stop the precession of \mathbf{R}' about the pseudofield vector. The

rotation matrix is

$$\begin{bmatrix} \hat{\mathbf{1}}^{iv} \\ \hat{\mathbf{2}}^{iv} \\ \hat{\mathbf{3}}^{iv} \end{bmatrix} = \begin{bmatrix} 1 & 0 & 0 \\ 0 & \cos(\Omega t) & -\sin(\Omega t) \\ 0 & \sin(\Omega t) & \cos(\Omega t) \end{bmatrix} \begin{bmatrix} \hat{\mathbf{1}}''' \\ \hat{\mathbf{2}}''' \\ \hat{\mathbf{3}}''' \end{bmatrix}. \quad (50)$$

Inverting 50 gives the Bloch vector

$$\begin{bmatrix} \mathbf{u}^{iii} \\ \mathbf{v}^{iii} \\ \mathbf{w}^{iii} \end{bmatrix} = \begin{bmatrix} 1 & 0 & 0 \\ 0 & \cos(\Omega' t) & \sin(\Omega' t) \\ 0 & -\sin(\Omega' t) & \cos(\Omega' t) \end{bmatrix} \begin{bmatrix} \mathbf{u}^{iv} \\ \mathbf{v}^{iv} \\ \mathbf{w}^{iv} \end{bmatrix} \quad (51)$$

The relationship between the rotating and stationary Bloch vectors is then found by multiplying matrices 48 and 51. If we define u_o, v_o, w_o as the elements of the Bloch vector at time $t = 0$, then the product of matrices 48 and 51 gives

$$\begin{bmatrix} \mathbf{u}_o \\ \mathbf{v}_o \\ \mathbf{w}_o \end{bmatrix} = \begin{bmatrix} \cos(\psi) \cos(\phi) & \sin(\phi) & \sin(\psi) \cos(\phi) \\ -\cos(\psi) \sin(\phi) & \cos(\phi) & -\sin(\psi) \sin(\phi) \\ -\sin(\psi) & 0 & \cos(\psi) \end{bmatrix} \begin{bmatrix} \mathbf{u}^{iv} \\ \mathbf{v}^{iv} \\ \mathbf{w}^{iv} \end{bmatrix}. \quad (52)$$

Inverting Eq. 52 and multiplying it by the product of matrices 48 and 51 determines the Bloch vector at any time t and in any direction α :

$$\begin{bmatrix} \mathbf{u}' \\ \mathbf{v}' \\ \mathbf{w}' \end{bmatrix} = \begin{bmatrix} \cos(\psi) \cos(\phi) & \sin(\phi) & \sin(\psi) \cos(\phi) \\ -\cos(\psi) \sin(\phi) & \cos(\phi) & -\sin(\psi) \sin(\phi) \\ -\sin(\psi) & 0 & \cos(\psi) \end{bmatrix} \times \begin{bmatrix} 1 & 0 & 0 \\ 0 & \cos(\Omega' t) & \sin(\Omega' t) \\ 0 & -\sin(\Omega' t) & \cos(\Omega' t) \end{bmatrix} \times \begin{bmatrix} \cos(\psi) \cos(\phi) & -\cos(\psi) \sin(\phi) & -\sin(\psi) \\ \sin(\phi) & \cos(\phi) & 0 \\ \sin(\psi) \cos(\phi) & -\sin(\psi) \sin(\phi) & \cos(\psi) \end{bmatrix} \begin{bmatrix} \mathbf{u}_o \\ \mathbf{v}_o \\ \mathbf{w}_o \end{bmatrix} \quad (53)$$

Equation 53 can be simplified using Eqs. 46 and 49

$$\begin{aligned} \sin(\psi) &= \frac{\Delta}{\Omega'} \\ \cos(\psi) &= \frac{\chi}{\Omega'} \end{aligned} \quad (54)$$

where from Eq. 44

$$\phi = \alpha. \quad (55)$$

If the time t corresponds to the pulse duration (τ_p) and the excitation pulse is assumed to be a “top hat” function, then the pulse area is given by

$$\theta = \chi\tau_p \quad (56)$$

When multiplying out Eq. 53 the following assumptions are also made.

1. The pulse area is small enough ($\theta \ll 1$) such that

$$\begin{aligned} \cos(\theta) &\approx 1 - \frac{\theta^2}{2} \\ \sin(\theta) &\approx \theta \end{aligned}$$

2. Excitation is near resonance so that Δ is small, or

$$\Delta\tau_p \ll 1.$$

3. Terms of second order in θ or $\Delta\tau_p$ may be discarded, unless doing so would result in a trivial term ($=1$), or would result in dropping a term with wavevector (α) information.

By using the above assumptions, the Bloch vector during the excitation pulse is found from Eq. 53 to be

$$\begin{bmatrix} \mathbf{u}' \\ \mathbf{v}' \\ \mathbf{w}' \end{bmatrix} = \mathbf{A} \begin{bmatrix} \mathbf{u}_o \\ \mathbf{v}_o \\ \mathbf{w}_o \end{bmatrix}$$

where the excitation matrix \mathbf{A} is

$$\begin{bmatrix} 1 - \frac{(\Delta\tau_p)^2}{2} - \frac{\theta^2}{2} \sin^2(\alpha) & -\Delta\tau_p - \frac{\theta^2}{4} \sin(2\alpha) & \theta \sin(\alpha) \\ \Delta\tau_p - \frac{\theta^2}{4} \sin(2\alpha) & 1 - \frac{(\Delta\tau_p)^2}{2} - \frac{\theta^2}{2} \cos^2(\alpha) & \theta \cos(\alpha) \\ -\theta \sin(\alpha) & -\theta \cos(\alpha) & 1 - \frac{\theta^2}{2} \end{bmatrix} \quad (57)$$

The relaxation matrix

The next step is to find how the Bloch vector behaves when the excitation pulse is turned off. The kinetic equations of the diagonal terms shown below follow from Fig. ??.

$$\begin{aligned}\frac{d\rho_{22}}{dt} &= -(k_{21} + k_{23})\rho_{22} \\ \frac{d\rho_{33}}{dt} &= -k_{31}\rho_{33} + k_{23}\rho_{22} \\ \frac{d\rho_{11}}{dt} &= k_{21}\rho_{22} + k_{31}\rho_{33}\end{aligned}\tag{58}$$

The solution to the first of Eqs. 58 is

$$\rho_{22}(t) = \rho_{22}(0)e^{-t/T_1}\tag{59}$$

where $T_1 = 1/(k_{21} + k_{23})$ is the longitudinal relaxation time. Substituting Eq. 59 into the second of Eqs. 58 and using an integrating factor $e^{k_{31}t}$ gives the solution for $\rho_{33}(t)$

$$\rho_{33}(t) = [be^{-k_{31}t} - be^{-t/T_1}]\rho_{22}(0) + \rho_{33}(0)e^{-k_{31}t}\tag{60}$$

where $b = k_{23}/(k_{21} + k_{23} - k_{31})$. Lastly, by using conservation of energy:

$$\begin{aligned}1 &= \rho_{11}(t) + \rho_{22}(t) + \rho_{33}(t) \\ &= \rho_{11}(0) + \rho_{22}(0) + \rho_{33}(0)\end{aligned}\tag{61}$$

we can write

$$\rho_{11}(t) = \rho_{11}(0) + \rho_{22}(0) + \rho_{33}(0) - \rho_{22}(t) - \rho_{33}(t).\tag{62}$$

Substituting Eqs. 60 and 61 into Eq. 62 and collecting terms gives the solution for the third of Eqs. 58

$$\rho_{11}(t) = \rho_{11}(0) + [(b-1)e^{-t/T_1} + 1 - be^{-k_{31}t}]\rho_{22}(0) + [1 - e^{-k_{31}t}]\rho_{33}(0).\tag{63}$$

To determine the relaxation of the off diagonal terms ρ_{21} & ρ_{12} , we solve the equations of motion for the Bloch vector with zero applied field ($\chi = 0$). From Eq.

41

$$\frac{d\mathbf{R}}{dt} = \begin{vmatrix} 0 & 0 & \omega_o - \omega \\ u & v & w \end{vmatrix}$$

$$\dot{u} = -\Delta v - u/T_2 \quad (64)$$

$$\dot{v} = \Delta u - v/T_2 \quad (65)$$

$$\dot{w} = -\frac{w - w_e}{T_1} \quad (66)$$

In the above three equations, relaxation terms have been added phenomenologically. T_2 is the off-diagonal relaxation time, or dephasing time, and T_1 is the population relaxation time. w_e is the inversion parameter at equilibrium.

From Eq. 65 we have

$$u = \frac{1}{\Delta} \left[\dot{v} + \frac{v}{T_2} \right]. \quad (67)$$

Substituting Eq. 67 into Eq. 64 and solving for v gives

$$v = A_1 e^{(-1/T_2 + \Delta i)t} + A_2 e^{(-1/T_2 - \Delta i)t} \quad (68)$$

$$A_1 + A_2 = v_o. \quad (69)$$

Substituting Eq. 68 into Eq. 67 leads to a solution for u

$$u = i[A_1 e^{(-1/T_2 + \Delta i)t} - A_2 e^{(-1/T_2 - \Delta i)t}] \quad (70)$$

$$i[A_1 - A_2] = u_o. \quad (71)$$

A_1 and A_2 are found in terms of u_o and v_o by solving Eqs. 69 and 71. The definition of the Bloch vector components u and v is

$$u = \rho_{12} + \rho_{21} \quad (72)$$

$$v = i(\rho_{21} - \rho_{12}). \quad (73)$$

By using Eqs. 72, 73, 68, and 69 the solution of the off-diagonal matrix elements is found:

$$\rho_{21}(t) = e^{-t/T_2} e^{-i\Delta t} \rho_{21}(0) \quad (74)$$

and $\rho_{12}(t)$ follows from $\rho_{12} = \rho_{21}^*$.

From Eqs. 59, 60, 63, and 74 we can write down the matrix which governs the relaxation of the density matrix components under zero applied field:

$$\begin{bmatrix} \rho_{11}(t) \\ \rho_{12}(t) \\ \rho_{21}(t) \\ \rho_{22}(t) \\ \rho_{33}(t) \end{bmatrix} = \mathbf{C} \begin{bmatrix} \rho_{11}(0) \\ \rho_{12}(0) \\ \rho_{21}(0) \\ \rho_{22}(0) \\ \rho_{33}(0) \end{bmatrix}$$

$$\mathbf{C} = \begin{bmatrix} 1 & 0 & 0 & \{1 + (b-1)e^{-t/T_1} - be^{-k_{31}t}\} & \{1 - e^{-k_{31}t}\} \\ 0 & e^{-t/T_2}e^{i\Delta t} & 0 & 0 & 0 \\ 0 & 0 & e^{-t/T_2}e^{-i\Delta t} & 0 & 0 \\ 0 & 0 & 0 & e^{-t/T_1} & 0 \\ 0 & 0 & 0 & \{be^{-k_{31}t} - be^{-t/T_1}\} & e^{-k_{31}t} \end{bmatrix} \quad (75)$$

Calculation of the Bloch vector following a 2-pulse sequence.

The next step is to calculate the inversion parameter (w) and the coherence parameters (u, v) immediately following a 2-pulse sequence, as shown in Fig.26.

To begin, we use the excitation matrix Eq. 57 to calculate the inversion parameter immediately after the pump pulse ($w(\tau_p)$). In order to do this, we must make 2 important assumptions:

1. There is no relaxation during the pump pulse ($\tau_p \ll T_2$).
2. There is no coherence at $t = 0$ ($u(0) = v(0) = 0$)

We find that

$$w(\tau_p) = \left(1 - \frac{\theta_1^2}{2}\right)w(0) \quad (76)$$

where, as stated before, $w(0) = \rho_{22}(0) - \rho_{11}(0) = -1$.

The coherence parameters are similarly found from Eq. 57 to be

$$u(\tau_p) = \theta_1 \sin(\alpha)w(0) \quad (77)$$

$$v(\tau_p) = \theta_1 \cos(\alpha)w(0). \quad (78)$$

In the interval between the pump and probe pulses, we must apply the relaxation matrix (Eq. 75). In doing this, we assume that we can neglect population relaxation ($t_{12} \ll T_1$). This means that the inversion parameter (w) will not change during t_{12} ; only the coherence parameters (u, v) will change. From the relaxation matrix and the definition of u at the end of the interval t_{12}

$$u(t_{12}) = e^{-t_{12}/T_2} [e^{i\Delta t_{12}} \rho_{12}(0) + e^{-i\Delta t_{12}} \rho_{21}(0)] \quad (79)$$

where $\rho_{12}(0)$ and $\rho_{21}(0)$ are the off diagonal density matrix elements of the system after the 1st pulse. These can be found from Eqs. 77 and 78 using the definitions of u and v :

$$\rho_{12}(0) = \rho_{12}(\tau_p) = \frac{\theta_1}{2} w(0) [\sin(\alpha) + i \cos(\alpha)] \quad (80)$$

$$\rho_{21}(0) = \rho_{12}^*(0). \quad (81)$$

Substituting Eqs. 80,81 into Eq. 79 gives

$$\begin{aligned} u(t_{12}) &= e^{-t_{12}/T_2} \frac{\theta_1}{2} w(0) [e^{i\Delta t_{12}} (\sin(\alpha) + i \cos(\alpha)) + e^{-i\Delta t_{12}} (\sin(\alpha) - i \cos(\alpha))] \\ &= -w(0) \theta_1 e^{-t_{12}/T_2} \sin(\Delta t_{12} - \alpha). \end{aligned} \quad (82)$$

Similarly, we find for $v(t_{12})$

$$\begin{aligned} v(t_{12}) &= i e^{-t_{12}/T_2} [e^{-i\Delta t_{12}} \rho_{21}(0) - e^{i\Delta t_{12}} \rho_{12}(0)] \\ &= i e^{-t_{12}/T_2} \frac{\theta_1}{2} w(0) [e^{-i\Delta t_{12}} (\sin(\alpha) - i \cos(\alpha)) - e^{i\Delta t_{12}} (\sin(\alpha) + i \cos(\alpha))] \\ &= w(0) \theta_1 e^{-t_{12}/T_2} \cos(\Delta t_{12} - \alpha). \end{aligned} \quad (83)$$

To summarize our work so far:

1. Equation 76 gives the inversion parameter at time $t = \tau_p$.
2. During the delay between the two pulses ($t = t_{12}$), the inversion parameter remains Eq. 76. The coherences at time $t = \tau_{12}$ are given by Eqs. 82 and 83.

Finally, we use the excitation matrix (Eq. 57) to find the inversion parameter after the probe pulse ($t = t_{12}^+$):

$$w(t_{12}^+) = -\theta_2 \sin(\alpha)u(t_{12}) - \theta_2 \cos(\alpha)v(t_{12}) + (1 - \frac{\theta_2^2}{2})w(\tau_p). \quad (84)$$

By substituting Eqs. 76, 82, and 83 into Eq. 84, and doing the appropriate algebra, we find

$$w(t_{12}^+) = w(0)[(1 - \frac{\theta_1^2}{2})(1 - \frac{\theta_2^2}{2}) - \theta_1\theta_2 e^{-t_{12}/T_2} \cos(\alpha - \Delta t_{12})]. \quad (85)$$

For reasons that will be apparent later, this can be rewritten as

$$w(t_{12}^+) = (1 - p) - 1 \quad (86)$$

where p is called the excitation parameter, and is given by

$$(1 - \frac{\theta_1^2}{2})(1 - \frac{\theta_2^2}{2}) - \theta_1\theta_2 e^{-t_{12}/T_2} \cos(\alpha - \Delta t_{12}). \quad (87)$$

Calculation of the APE signal

Using the expressions for the coherences (Eqs. 82,83) and the population inversion parameter (Eq. 76) just before the arrival of the probe pulse, we can calculate the transmitted probe intensity, and thus the APE signal.

The electromagnetic wave equation for a homogeneous, isotropic dielectric is

$$\nabla^2 \mathbf{E} = \frac{n^2}{c^2} \frac{\partial^2 \mathbf{E}}{\partial t^2} + \frac{1}{c^2 \epsilon_o} \frac{\partial^2 \mathbf{P}}{\partial t^2} \quad (88)$$

where

- n = index of refraction
- ϵ_o = permittivity of free space
- c = speed of light .

If we look only in the probe beam (z) direction, Eq. 88 reduces to

$$\frac{\partial^2 E}{\partial z^2} = \frac{n^2}{c^2} \frac{\partial^2 E}{\partial t^2} + \frac{1}{c^2 \epsilon_o} \frac{\partial^2 P}{\partial t^2}. \quad (89)$$

The optical field is described by a plane polarized wave

$$E(z, t) = E_o(z, t) \cos(\omega t - kz + \phi) \quad (90)$$

where $E_o(z, t)$ is the pulse envelope which varies slowly compared to the optical period ($1/\omega$). The polarization in the medium at a given detuning frequency Δ is given by

$$P = N \text{Trace}(\mu\rho). \quad (91)$$

To find the weighted average of P , it is necessary to integrate Eq. 91 across the normalized inhomogeneous distribution which is given by $g(\Delta)$ or

$$P = N \int_{-\infty}^{+\infty} g(\Delta) \text{Tr}(\mu\rho) d\Delta \quad (92)$$

where N is the number density of absorbing ions and

$$\begin{aligned} \text{Tr}(\mu\rho) &= \mu_{12}(\rho_{21} + \rho_{12}) \\ &= \mu_{12}[u] \end{aligned} \quad (93)$$

Note that u is in the stationary frame, and is related to the rotated frame by Eq. 40:

$$u = u' \cos(\omega t - \alpha) - v' \sin(\omega t - \alpha). \quad (94)$$

If we include the phase factor $e^{-i\alpha}$ in the rotating frame transformation Eq. 40 becomes

$$\begin{bmatrix} 1 \\ 2 \\ 3 \end{bmatrix} = \begin{pmatrix} \cos(\omega t - \alpha) & -\sin(\omega t - \alpha) & 0 \\ \sin(\omega t - \alpha) & \cos(\omega t - \alpha) & 0 \\ 0 & 0 & 1 \end{pmatrix} \begin{bmatrix} 1' \\ 2' \\ 3' \end{bmatrix} \quad (95)$$

and the pseudofield vector (Eq. 42) becomes

$$\mathbf{\Omega}' = -\chi \hat{\mathbf{1}}' + \Delta \hat{\mathbf{3}}'. \quad (96)$$

The equations of motion (when including the phase factor in the rotation) are (Eq. 41)

$$\dot{u}' = -\Delta v' \quad (97)$$

$$\dot{v}' = \Delta u' + \chi w' \quad (98)$$

$$\dot{w}' = \dot{w} = -\chi v'. \quad (99)$$

Inserting Eq. 94 into Eq. 92 gives for the polarization

$$P = N \int_{-\infty}^{+\infty} g(\Delta) \mu_{12} [u' \cos(\omega t - kz + \phi) - v' \sin(\omega t - kz + \phi)] d\Delta. \quad (100)$$

We now insert the optical field expression (Eq. 90) into Maxwell's equation (Eq. 89). Note the following conventions:

1. Let $\eta = -\omega t + kz + \phi$
2. $\frac{n^2}{c^2} \omega^2 = k^2$
3. Using the slowly varying envelope approximation (SVEA) for $E_o(z, t)$ implies that as long as E_o varies more slowly in time than the optical frequency ω , and as long as during the time of 1 pulse width the pulse does not travel less than the reciprocal wavevector, we may neglect the second derivative terms E_{tt} and E_{zz} .

With the above simplifications, the wave equation takes the form

$$\frac{\partial E_o}{\partial z} \sin(\eta) = \frac{-n}{c} \frac{\partial E_o}{\partial t} \sin(\eta) - \frac{1}{2k} \frac{1}{\epsilon_o c^2} \frac{\partial^2 P}{\partial t^2}. \quad (101)$$

Taking the second time derivative of Eq. 100 gives the source term of the wave equation:

$$\begin{aligned} \frac{\partial^2 P}{\partial t^2} = & N \mu_{12} \int_{-\infty}^{+\infty} [(-u' \omega^2 + \ddot{u}' - 2\omega \dot{v}') \cos(\eta) \\ & + (2\omega \dot{u}' - v' \omega^2 + \ddot{v}') \sin(\eta)] g(\Delta) d\Delta. \end{aligned} \quad (102)$$

Inserting the above source term into the wave equation (Eq. 101), equating like ($\sin(\eta)$) terms, and using Eq. 97 allows us to further simplify the wave equation:

$$\frac{\partial E_o}{\partial z} = \frac{-n}{c} \frac{\partial E_o}{\partial t} - \frac{N \mu_{12}}{2\epsilon_o k c^2} \int_{-\infty}^{+\infty} [-2\omega \Delta v' - v' \omega^2 + \ddot{v}'] g(\Delta) d\Delta. \quad (103)$$

We need to rank the terms of the integrand in Eq. 103 so that small terms can be omitted. The following conditions are true in our case

$$\begin{aligned} \omega \Delta & \ll \omega^2 \quad (\text{near resonance condition}) \\ \ddot{v}' & \ll \omega^2 v' \quad (\text{SVEA}) \end{aligned}$$

which implies that

$$2\omega\Delta, \ddot{v}' \ll \omega^2 v' \quad (104)$$

and Eq. 103 can be reduced to

$$\frac{\partial E_o}{\partial z} = \frac{-n}{c} \frac{\partial E_o}{\partial t} - \frac{\omega N \mu_{12}}{2\epsilon_o n c} \int_{-\infty}^{+\infty} [v'(\Delta, r, t) g(\Delta) d\Delta]. \quad (105)$$

To find the total pulse intensity, it is necessary to integrate Eq. 105 over the pulse duration, t_p

$$\theta_2 = \frac{\mu_{12}}{\hbar} \int_0^{\tau_p} E_o dt \quad (106)$$

where for a symmetric function (such as our “top hat” function)

$$\int_0^{\tau_p} \frac{\partial E_o}{\partial t} dt = 0. \quad (107)$$

After this integration Eq. 105 becomes

$$\frac{\partial \theta_2}{\partial z} = \frac{\omega N \mu_{12}^2}{2\hbar \epsilon_o n c} \int_0^{\tau_p} \int_{-\infty}^{+\infty} v'(\Delta, r, t) g(\Delta) d\Delta dt. \quad (108)$$

The time integral can be simplified by using Eqs. 76, 85, and 99

$$\begin{aligned} \int_0^{\tau_p} v'(\Delta, r, t) dt &= \frac{-1}{\chi_2} \int_{\tau_p^+}^{\tau_p^-} \frac{dw}{dt} dt \\ &= \frac{1}{\chi_2} \left[\frac{\theta_2}{2} \left(1 - \frac{\theta_2^2}{2} \right) w(0) + w(0) \theta_1 \theta_2 e^{-t_{12}/T_2} \cos(\alpha - \Delta t_{12}) \right]. \end{aligned} \quad (109)$$

When we calculated the inversion parameter $w(t_{12}^+)$ for a single 2-pulse sequence in Eq. 85, we wrote it as $w(t_{12}^+) = (1 - p) - 1$ where $w(0) = -1$. For many pump-probe sequences, the inversion parameter can be written as

$$w(t_{12}^+) = (1 - p)\gamma - 1 = w(0) \quad (110)$$

where γ is called the “enhancement factor”. [6] As such, γ parameterizes the degree to which a frequency grating is accumulated in the ground state. A material with a very lossy bottleneck state would be characterized by a relatively small accumulation effect, and thus a small value for γ . The excitation parameter p is given by Eq. 87.

Inserting Eq. 109 and 110 into Eq. 108 and integrating over a gaussian inhomogeneous distribution

$$g(\Delta) = \frac{1}{\sqrt{\pi} \delta \omega_{inh}} e^{-\left(\frac{\Delta}{\delta \omega_{inh}}\right)^2} \quad (111)$$

gives

$$\begin{aligned}
\frac{\partial \theta_2}{\partial z} &= \frac{\omega N \mu_{12}^2}{2 \hbar \epsilon_0 n c} \frac{1}{\chi_2} \left[\frac{\theta_2^2}{2} \left(1 - \frac{\theta_1^2}{2} \right) \left(\left\{ 1 - \left(1 - \frac{\theta_1^2}{2} \right) \left(1 - \frac{\theta_2^2}{2} \right) \right\} \gamma - 1 \right) \right. \\
&\quad \left. + \frac{1}{2} \gamma \theta_1^2 \theta_2^2 e^{-2t_{12}/T_2} \right] \\
&= \frac{\alpha \tau_p}{2 \pi g(0)} \theta_2 \left[\frac{\gamma \theta_2^2}{4} \left(1 + \frac{\theta_2^2}{\theta_1^2} - \theta_2^2 - \theta_1^2 + \frac{\theta_1^2 \theta_2^2}{4} \right) \right. \\
&\quad \left. + \frac{\gamma \theta_1^2}{4} \left(2e^{-2t_{12}/T_2} - \frac{1}{2} \left(1 - \frac{\theta_1^2}{2} \right) \right) \right]
\end{aligned} \tag{112}$$

where we have used

$$\theta_2 = \chi_2 \tau_p. \tag{113}$$

In this experiment, it can be assumed that $\theta_2 \ll \theta_1$ so we may omit terms of second order in θ_2 and Eq. 112 can be integrated to give the intensity of the probe pulse exiting the sample

$$I(l) = I(0) \exp\left(-\alpha_{eff} \left[\frac{1}{2} \left(1 - \frac{\theta_1^2}{2} \right) - \left(1 - \theta_1^2 + 2e^{-2t_{12}/T_2} \right) \frac{\gamma \theta_1^2}{4} \right] l\right) \tag{114}$$

where we have replaced the pulse area θ_2 with the beam intensity since the two are proportional. We have also defined an effective absorption coefficient

$$\alpha_{eff} = \frac{\alpha \tau_p}{2 \pi g(0)} \tag{115}$$

where α is the regular absorption coefficient, τ_p is the pulse area, and $g(0) = \frac{1}{\sqrt{\pi} \delta \omega_{inh}}$ is the inverse inhomogeneous linewidth of the transition.

As described in Chapter 2 of this thesis, the pump beam is modulated and the APE signal is detected with a phase-sensitive detector. The detected signal is then given by

$$\begin{aligned}
S(t_{12}) &= \frac{I_{on} - I_{off}}{I_{off}} \\
&= \exp\left(\frac{\alpha_{eff} l}{2} \left[\frac{\theta_1^2}{2} (1 + \gamma) + \gamma \theta_1^2 e^{-2t_{12}/T_2} \right]\right) - 1
\end{aligned} \tag{116}$$

where we have assumed that $\theta_1 \ll 1$, which is usually the case with the type of quasi-cw laser used in this experiment. Since the signal is very small, Eq. 116 can be written as

$$S(t_{12}) = \frac{\alpha_{eff} l}{2} \left[\frac{\theta_1^2}{2} (1 + \gamma) + \gamma \theta_1^2 e^{-2t_{12}/T_2} \right] \tag{117}$$

which is the detected APE signal.

APPENDIX C

APE DATA TABLES

The data contained in the following tables were determined from exponential fits to APE signals. The raw data had its baseline subtracted, and was shifted along the time axis so that the APE maximum occurs at $t_{12} = 0$. Peakfit v. 3.18 was used to fit exponential functions to the APE signal function. The total dephasing time, T_2 , is calculated as twice the fitted decay time.

To provide an estimate of the fitted parameter error, the 95% confidence interval is given. This is to say that we can be 95% confident that the actual parameter value lies within this numeric range. "N.A." means that the data is not available.

TABLE I

$^4I_{9/2} \rightarrow ^4G_{5/2}, ^2G_{7/2}$ ABSORPTION SPECTRUM
GAUSSIAN DECONVOLUTION FOR Nd³⁺ DOPED GLASSES

glass	peak #	amplitude	center (nm)	width (nm)
silicate	1	0.05	570.18	5.63
	2	0.18	571.79	3.79
	3	0.24	575.70	5.84
	4	0.40	583.89	6.76
	5	0.04	589.41	2.34
	6	0.06	591.12	3.53
germanate	1	0.39	573.51	6.82
	2	0.03	577.19	4.01
	3	0.53	582.89	7.88
	4	0.03	589.01	2.56
	5	0.04	590.76	3.75
phosphate	1	0.37	570.02	1.22
	2	0.17	570.64	2.47
	3	0.28	573.87	1.49
	4	0.26	578.43	2.72
	5	0.43	582.00	1.93
	6	0.06	585.82	0.84
	7	0.09	587.24	1.61

TABLE II
 TEMPERATURE DEPENDENCE OF T_2 AS MEASURED
 BY APE IN $\text{Nd}^{3+}:\text{ED2}$ SILICATE GLASS AT
 593.1 NM, $\Delta\lambda = 1.5\text{NM}$

T (K)	a1 (μV)	$T_2(\text{a})$ (ps)	95% C.I. (ps)	a2 (μV)	$T_2(\text{b})$ (ps)	95% C.I. (ps)
9.5	6	5.24	3.12 - 7.34	16	20.8	19.4 - 22.0
20.0	10	5.28	3.14 - 7.42	14	17.4	15.1 - 19.6
30.0	10	3.12	1.92 - 4.32	11	13.6	12.2 - 15.0
40.0	9	3.40	1.42 - 5.40	8	9.30	6.40 - 12.0
50.0	10	3.16	1.62 - 4.72	4	10.4	4.00 - 16.0
65.0	7	1.22	0.38 - 2.06	9	4.48	3.68 - 5.20
80.0	10	2.60	2.44 - 2.74	N.A.	N.A.	N.A.
100.0	10	1.78	1.66 - 1.90	N.A.	N.A.	N.A.

TABLE III
 WAVELENGTH DEPENDENCE OF T_2 AS MEASURED BY APE IN
 $\text{Nd}^{3+}:\text{ED2}$ SILICATE GLASS AT 9.5K

λ (nm)	a1 (μV)	$T_2(\text{a})$ (ps)	95% C.I. (ps)	a2 (μV)	$T_2(\text{b})$ (ps)	95% C.I. (ps)
577.9	71	1.16	0.92 - 1.40	13	3.28	2.06 - 4.40
579.8	36	1.26	0.52 - 2.00	54	2.84	2.08 - 3.60
582.1	74	1.66	1.24 - 2.06	47	3.68	2.70 - 4.66
583.7	76	1.58	1.26 - 1.88	69	4.24	3.72 - 4.74
585.8	104	2.26	1.98 - 2.56	51	7.34	6.16 - 8.52
587.9	68	2.72	2.48 - 2.98	76	11.3	10.8 - 11.8
588.3	22	3.94	0.44 - 7.44	35	14.8	12.6 - 17.1
589.9	34	4.68	3.94 - 5.42	73	14.6	13.9 - 15.2
592.0	27	6.48	5.30 - 7.68	42	20.6	19.3 - 22.0
593.1	10	10.6	3.56 - 17.6	11	24.2	14.0 - 34.0
594.1	17	11.0	9.14 - 12.9	17	25.0	25.0 - 42.2

TABLE IV
 TEMPERATURE DEPENDENCE OF T_2 AS MEASURED
 BY APE IN Nd^{3+} :GERMANATE GLASS AT
 594.0 NM, $\Delta\lambda = 1.5\text{NM}$

T (K)	a1 (μV)	T_2 (a) (ps)	95% C.I. (ps)	a2 (μV)	T_2 (b) (ps)	95% C.I. (ps)
9.5	52	27.8	26.8 - 28.8	N.A.	N.A.	N.A.
15.0	24	24.6	23.4 - 25.6	N.A.	N.A.	N.A.
20.0	40	22.1	21.6 - 22.6	N.A.	N.A.	N.A.
30.0	33	16.4	15.7 - 17.0	N.A.	N.A.	N.A.
40.0	26	11.4	10.9 - 12.0	N.A.	N.A.	N.A.
50.0	28	8.38	8.00 - 8.78	N.A.	N.A.	N.A.
65.0	21	5.78	5.46 - 6.10	N.A.	N.A.	N.A.
80.0	23	2.72	2.12 - 3.30	N.A.	N.A.	N.A.
100.0	14	2.12	1.80 - 2.42	N.A.	N.A.	N.A.

TABLE V

WAVELENGTH DEPENDENCE OF T_2 AS MEASURED BY APE IN
 Nd^{3+} :GERMANATE GLASS AT 9.5K

λ (nm)	a1 (μV)	T_2 (a) (ps)	95% C.I. (ps)	a2 (μV)	T_2 (b) (ps)	95% C.I. (ps)
570.0	439	2.00	1.78 - 2.24	N.A.	N.A.	N.A.
572.0	619	1.64	1.50 - 1.78	N.A.	N.A.	N.A.
576.0	408	2.00	1.70 - 2.30	N.A.	N.A.	N.A.
578.0	342	2.24	2.04 - 2.42	N.A.	N.A.	N.A.
579.9	99	2.88	2.70 - 3.04	N.A.	N.A.	N.A.
581.8	105	1.94	1.08 - 2.78	40	7.86	0.38 - 15.4
584.0	305	1.76	1.54 - 2.00	166	8.56	7.46 - 9.64
585.9	146	2.54	2.34 - 2.72	95	13.0	12.3 - 13.8
588.0	160	2.74	2.24 - 3.22	325	20.1	19.4 - 20.8
590.0	62	14.7	5.98 - 23.4	90	33.8	22.4 - 44.0
591.9	88	24.4	16.2 - 32.8	20	84.4	0.00 - 219
594.0	52	27.8	26.8 - 28.8	N.A.	N.A.	N.A.

TABLE VI

TEMPERATURE DEPENDENCE OF T_2 AS MEASURED
 BY APE IN Nd^{3+} :PHOSPHATE GLASS AT
 589.9 NM, $\Delta\lambda = 1.5\text{NM}$

T (K)	a1 (μV)	T_2 (a) (ps)	95% C.I. (ps)	a2 (μV)	T_2 (b) (ps)	95% C.I. (ps)
9.5	79	14.7	14.1 - 15.3	N.A.	N.A.	N.A.
15.0	79	12.1	11.7 - 12.5	N.A.	N.A.	N.A.
20.0	65	11.4	11.0 - 11.7	N.A.	N.A.	N.A.
30.0	65	8.64	8.36 - 8.94	N.A.	N.A.	N.A.
40.0	53	6.28	6.02 - 6.54	N.A.	N.A.	N.A.
50.0	62	4.12	4.00 - 4.26	N.A.	N.A.	N.A.
65.0	44	3.46	3.28 - 3.62	N.A.	N.A.	N.A.
80.0	41	2.28	2.16 - 2.42	N.A.	N.A.	N.A.
100.0	36	1.76	1.68 - 1.86	N.A.	N.A.	N.A.

TABLE VII

WAVELENGTH DEPENDENCE OF T_2 AS MEASURED BY APE IN
 Nd^{3+} :PHOSPHATE GLASS AT 9.5K

λ (nm)	a1 (μV)	T_2 (a) (ps)	95% C.I. (ps)	a2 (μV)	T_2 (b) (ps)	95% C.I. (ps)
568.0	52	2.28	2.06 - 2.50	N.A.	N.A.	N.A.
570.0	166	1.94	1.90 - 2.00	N.A.	N.A.	N.A.
572.1	206	1.60	1.58 - 1.64	N.A.	N.A.	N.A.
573.9	125	1.88	1.84 - 1.92	N.A.	N.A.	N.A.
576.0	97	1.84	1.76 - 1.94	N.A.	N.A.	N.A.
578.0	126	2.18	2.12 - 2.24	N.A.	N.A.	N.A.
580.0	105	1.84	1.24 - 2.44	N.A.	N.A.	N.A.
581.9	86	2.12	1.58 - 2.66	25	6.94	1.64 - 12.2
584.2	50	2.24	1.36 - 3.12	87	7.68	6.48 - 8.88
584.8	10	2.62	1.76 - 3.46	18	10.8	9.44 - 12.2
586.0	28	4.54	0.68 - 8.38	87	14.0	11.8 - 16.3
588.0	74	10.8	9.26 - 12.4	17	49.6	25.6 - 73.8
589.9	79	14.7	14.1 - 15.3	N.A.	N.A.	N.A.

TABLE VIII
 TEMPERATURE DEPENDENCE OF T_2 AS MEASURED
 BY APE IN $\text{Nd}^{3+}:\text{CaF}_2\text{YF}_3$ AT
 579.0 NM, $\Delta\lambda = 1.5\text{NM}$

T (K)	a1 (μV)	$T_2(\text{a})$ (ps)	95% C.I. (ps)	a2 (μV)	$T_2(\text{b})$ (ps)	95% C.I. (ps)
9.0	498	153	143 - 163	745	673	657 - 688
15.0	648	100	86.0 - 115	815	342	322 - 362
20.0	1095	118	93.6 - 142	70	310	0.00 - 877
30.0	612	37.8	28.6 - 47.2	338	102	77.6 - 126
40.0	497	28.4	27.6 - 29.4	N.A.	N.A.	N.A.
50.0	386	12.2	7.08 - 17.2	101	23.2	0.00 - 49.0
65.0	522	7.96	7.12 - 8.80	28	88.0	0.00 - 218
80.0	483	5.04	4.76 - 5.32	N.A.	N.A.	N.A.
100.0	384	3.64	3.00 - 4.28	N.A.	N.A.	N.A.

TABLE IX

TEMPERATURE DEPENDENCE OF T_2 AS MEASURED
 BY APE IN $\text{Nd}^{3+}:\text{CaF}_2\text{YF}_3$ AT
 580.2 NM, $\Delta\lambda = 1.5\text{NM}$

T (K)	a1 (μV)	$T_2(\text{a})$ (ps)	95% C.I. (ps)	a2 (μV)	$T_2(\text{b})$ (ps)	95% C.I. (ps)
8.9	246	106	86.4 - 125	247	601	556 - 646
15.0	72	71.4	4.44 - 138	106	284	187 - 380
20.0	21	34.6	0.92 - 68.2	22	184	36.2 - 331
30.0	23	5.78	0.00 - 11.8	14	65.8	47.8 - 84.0
40.0	70	10.9	3.28 - 18.6	115	32.0	22.4 - 41.4
50.0	119	14.1	13.3 - 14.9	N.A.	N.A.	N.A.
65.0	97	12.6	11.2 - 14.0	N.A.	N.A.	N.A.

TABLE X

TEMPERATURE DEPENDENCE OF T_2 AS MEASURED
 BY APE IN $\text{Nd}^{3+}:\text{CaF}_2\text{YF}_3$ AT
 579.04 NM, $\Delta\lambda = 0.1\text{NM}$

T	a1	$T_2(\text{a})$	95% C.I.	a2	$T_2(\text{b})$	95% C.I.
(K)	(μV)	(ps)	(ps)	(μV)	(ps)	(ps)
9.0	175	209	N.A.	152	609	N.A.
15.0	192	122	N.A.	118	372	N.A.
20.0	212	121	N.A.	25	333	N.A.
25.0	153	68.8	N.A.	52	148	N.A.
30.0	153	62.4	N.A.	N.A.	N.A.	N.A.
35.0	118	47.0	N.A.	N.A.	N.A.	N.A.
40.0	92	35.2	N.A.	N.A.	N.A.	N.A.

TABLE XI
 TEMPERATURE DEPENDENCE OF T_2 AS MEASURED
 BY APE IN $\text{Nd}^{3+}:\text{CaF}_2\text{YF}_3$ AT
 580.04 NM, $\Delta\lambda = 0.1\text{NM}$

T (K)	a1 (μV)	T_2 (a) (ps)	95% C.I. (ps)	a2 (μV)	T_2 (b) (ps)	95% C.I. (ps)
9.6	118	161	N.A.	86	415	N.A.
15.0	126	102	N.A.	63	325	N.A.
20.0	N.A.	71.8	N.A.	N.A.	197	N.A.
25.0	122	84.6	N.A.	N.A.	N.A.	N.A.
30.0	78	42.8	N.A.	29	108	N.A.
35.0	74	51.4	N.A.	N.A.	N.A.	N.A.
40.0	60	37.6	N.A.	N.A.	N.A.	N.A.

TABLE XII

WAVELENGTH DEPENDENCE OF T_2 AS MEASURED BY APE IN
Nd³⁺:CaF₂YF₃ AT 9.5K

λ (nm)	$\Delta\lambda$ (nm)	a1 (μ V)	T_2 (a) (ps)	95% C.I. (ps)	a2 (μ V)	T_2 (b) (ps)	95% C.I. (ps)
572.9	1.5	2.11	1.28	1.12 - 1.44	N.A.	N.A.	N.A.
574.3	1.5	0.62	2.88	2.34 - 3.42	0.02	31.80	0.00 - 146
575.0	1.5	0.50	2.36	1.60 - 3.14	0.32	7.92	6.50 - 9.34
575.5	1.5	0.43	4.36	2.54 - 6.20	0.36	11.2	7.80 - 14.5
575.8	1.5	0.21	5.98	5.24 - 6.72	0.21	19.2	17.0 - 21.4
576.7	1.5	N.A.	0.78	0.06 - 0.91	N.A.	6.94	5.98 - 7.88
576.5	0.1	0.40	19.4	15.0 - 23.8	0.04	84.8	0.00 - 178
577.0	0.1	0.76	8.70	5.68 - 11.7	0.24	54.8	45.4 - 64.0
577.5	0.1	0.86	8.48	7.64 - 9.32	0.19	105	89.6 - 118
578.0	0.1	0.99	157	116 - 198	0.02	1058	380 - 172
578.7	1.5	0.05	147	132 - 161	0.12	504	488 - 520
579.0	1.5	0.20	153	143 - 163	0.30	672	658 - 688
580.2	1.5	0.21	99.6	76.4 - 123	0.26	474	430 - 516
581.2	1.5	0.24	14.0	7.70 - 20.4	0.19	270	254 - 286

TABLE XIII

TEMPERATURE DEPENDENCE OF T_2 AS MEASURED
 BY APE IN 0.3% $\text{ND}^{3+}:\text{CaF}_2$ AT
 579.09NM, $\Delta\lambda = 0.1\text{NM}$

T (K)	a1 (μV)	$T_2(\text{a})$ (ps)	95% C.I. (ps)	a2 (μV)	$T_2(\text{b})$ (ps)	95% C.I. (ps)
9.0	210	430	368 - 492	230	3668	3464 - 3874
14.0	250	580	474 - 684	150	2456	2070 - 2842
18.0	240	458	332 - 584	120	1450	808 - 2090
24.0	N.A.	N.A.	N.A.	190	270	262 - 276
28.0	N.A.	N.A.	N.A.	240	192	179 - 204
35.0	N.A.	N.A.	N.A.	160	112	103 - 121

TABLE XIV

TEMPERATURE DEPENDENCE OF T_2 AS MEASURED
 BY APE IN 0.3% $\text{ND}^{3+}:\text{CaF}_2$ AT
 579.45NM, $\Delta\lambda = 0.1\text{NM}$

T	a1	$T_2(\text{a})$	95% C.I.	a2	$T_2(\text{b})$	95% C.I.
(K)	(μV)	(ps)	(ps)	(μV)	(ps)	(ps)
9.0	875	932	808 - 1058	123	18536	9612 - 27462
14.0	575	1106	998 - 1212	63	8654	3826 - 13482
18.0	500	158	140 - 176	650	988	954 - 1020
22.0	700	284	228 - 340	250	588	354 - 820
26.0	N.A.	N.A.	N.A.	775	230	224 - 234
30.0	N.A.	N.A.	N.A.	650	161	159 - 163
40.0	N.A.	N.A.	N.A.	400	71.6	67.2 - 76.2

TABLE XV

FFT FREQUENCY COMPONENT DISTRIBUTION FROM APE SIGNALS
OF M AND N CENTERS IN $\text{Nd}^{3+}:\text{CaF}_2$ at 9K, $\Delta\lambda = 0.1\text{nm}$

	center	interval	occurrence	center	interval	occurrence	center	interval	occurrence
		GHz			GHz			GHz	
M		0-2	2		17-18	2		33-34	0
		3-4	6		19-20	7		35-36	0
		5-6	21		21-22	1		37-38	0
		7-8	5		23-24	0		39-40	0
		9-10	3		25-26	2		41-42	1
		11-12	4		27-28	3		43-44	0
		13-14	1		29-30	0		45-46	3
		15-16	2		31-32	0		47-48	1
N		0-2	4		17-18	2		33-34	1
		3-4	9		19-20	2		35-36	0
		5-6	8		21-22	0		37-38	0
		7-8	10		23-24	1		39-40	1
		9-10	3		25-26	2		41-42	1
		11-12	3		27-28	0		43-44	0
		13-14	5		29-30	1		45-46	0
		15-16	1		31-32	0		47-48	0

VITA

KEITH W. VER STEEG

Candidate for the Degree of

Doctor of Philosophy

Report: ACCUMULATED PHOTON ECHOES AS A PROBE OF DEPHAS-
ING DYNAMICS IN $\text{Nd}^{3+}:\text{CaF}_2$, CaF_2YF_3 , AND GLASSES

Major field: Physics

Biographical:

Personal Data: Born in Rock Rapids, Iowa, son of Kenneth and Delores Ver Steeg. Married to Lori Annette Layton on June 4, 1988.

Education: Graduated from Central Lyon High School, Rock Rapids, Iowa, in May, 1982; Received Bachelor of Science Degree from Iowa State University in December, 1986, with a Major in Physics, Minor in Mathematics; received the Master of Science Degree from Oklahoma State University, Stillwater, Oklahoma in December, 1990; completed the requirements for the Doctor of Philosophy degree at Oklahoma State University in July, 1994.